National Technical University of Athens

Naval structure & Marine Engineering

Spatial Localization of Air Inclusions in Carbon Fiber T-beam, by Use of Wavelet Entropy Time Series from Hammer Tap Test.

By Spyridon Brouzas

Supervisor Ioannis T. Georgiou, Professor of Naval Architecture and Marine Engineering, NTUA & Adjunct Professor of Mechanical Engineering, Purdue University

May 21, 2021

Acknowledgements

This thesis would not have been possible without the guidance of my estimable professor and mentor Ioannis T. Georgiou. His immense contribution, not only by providing the database used from his research program IM PB Diagnostic but mainly by teaching me and inspiring me, reincarnated this project. I greatly appreciate his patience and will od power. I also feel fortunate to have been a part of this prestigious institution, the National Technical University of Athens which has in a way shaped me and prepared me for my future as a naval engineer. Last but not least, I would like to sincerely extend my gratitude to my friends and family who stood by my side and supported me in this endeavor.

This page is intentionally left blanc.

Abstract

Many critical safety structures such as aircrafts are constructed using extensively composite materials; therefore, non-destructive testing (NDT) of composite structures is imperative. The following thesis investigates a new method of NDT for carbon fiber structures based on the analysis of a vibration signal after exciting the composite specimen with a pulse. The analysis proposed in this report consists of transforming the signal using the Haar Wavelet Transform, segmenting the Transform in the time domain and calculating its Informational Entropy, as defined by Shannon, for every frame (Wavelet Entropy Time Series). The use of Wavelet Transform in combination with Shannons Informational Entropy (Wavelet Entropy) has been proven to identify irregularities in signals, mostly when comparing them to healthy signals using the KullbackLeibler Divergence (Relative Wavelet Entropy). Wavelet Entropy Time Series requires no additional signals for comparison. In this thesis, notions such as Wavelet Entropy and Wavelet Entropy Time Series are introduced and defined. The presupposition that Wavelet Entropy Time Series can single out and localize damaged areas of a structure is backed up both theoretically and experimentally.

To prove this experimentally, a carbon-fiber T-beam containing air inclusions was subject to hammer tap tests across its length. Accelerometers were mounted along its long axis. For every excitation, these accelerometers measured the vibration signals, which were then analyzed using Wavelet Entropy Time Series, and viewing its trend.

The experiment identified 2 locations where the Wavelet Entropy Time Series follows an increasing path. The signal from exciting the adjacent area to these locations also exhibits similar behavior those locations but with less intensity. Repetition of the experiment provides similar results proving that the outcomes were not random. It is therefore clear that the properties of the beam locally differ from the rest of the beam. This in combination with the knowledge that the beam contains air inclusions gives us a strong indication for their existence. However, extensive research is required to establish the accuracy and applicability of this NDT method.

Non-destructive testing (NDT) of composite specimens can be a tedious task, as such, any

new NDT method can be a new tool in the arsenal of an NDT inspector. The applicability of wavelet entropy time series for NDT could also probably extend outside of composite materials, for example in metal structures. The method, should it be developed commercially, could be a low-cost, reliable testing technique that requires just a computer, an accelerometer with relatively small sampling frequency of 5000Hz as well as little to no specialization on behalf of the tester.

Contents

1 Introduction

Due to the wide application of composite materials, the necessity to ensure sufficient reliability is imperative. Airplanes, high performance cars, spacecrafts and countless other sensitive engineering applications use extensively composites, such as carbon fiber. These structures require non-destructive testing (NDT) in order to identify potential defects that could compromise their mechanical properties . Testing composites can be challenging since not many methods of testing are commercially available and all of them can have significant drawbacks. Therefore, the study of new ways to reliably test composite structures is important since it can provide the tester with new tools to this strenuous task.

Radiography and Ultrasound testing have the most vast applicability of all NDT for composite materials. Conventional X-radiography provides very clear results. A major limitation of the method is its inability to detect delaminations. Furthermore, the use of ionizing radiation and hazardous chemicals creates health concerns for the tester. This combined with the increased cost of the equipment, makes radiography a less sustainable solution for smaller businesses. Ultrasonic testing, on the other hand, is widely used commercially for composite inspection. It is a budget method that requires no extensively specified tester that offers good quality resolution. However, its inability to identify small flaws, makes the method unsuitable for high sensitivity applications.

It is clear that exists a market gap for a budget, reliable method, capable of distinguishing small defects. This thesis investigates a new NDT method for testing carbon fiber structures called Wavelet Entropy Time Series which capitalizes on this market gap. The method relies on vibration signals acquired by exciting the inspected specimen with a pulse (e.g. hammer tap test), sampling with an accelerometer its response and analyzing the signal. Wavelet Entropy for signal testing although being a young idea, it finds multiple applications, including in shaft misalignment detection [Lin et al., 2010], transmission lines fault locating [Ekici et al., 2008], even biomedicine [Wang et al., 2014], and neuroscience [Rosso et al., 2001]. The concept behind Wavelet Entropy is to quantify the disorder of the information contained in a signal and its trend. One benefit of this method is the lack of requirement of signal from an undamaged

structure for comparison. The method developed although based on the paper *"Wavelet entropy: a new tool for analysis of short duration brain electrical signals"* [Rosso et al., 2001], has been slightly modified to allow for more clear and reliable results when examining the structural integrity of a carbon fiber structure.

2 Composite materials

The term composite material essentially means any structure that is comprised of two or more materials with different physical and chemical properties. Generally speaking, modern composite materials are comprised of a fiber dispersed in a continuous matrix phase. As a result, the composite structure exhibits improved properties than all the original materials. Due to their unique way of development, it is possible to create complicated geometries that exhibit the maximum efficiency from their reinforcement. They are lightweight with a remarkable weight to strength ration, they are exceptionally resilient to corrosion and can be used in a wide variety of applications.

2.1 Brief History

Humanity quickly realized that the properties of their constructions could be improved by combining different materials. Civilizations throughout the world have included straw in the creation of bricks, since they understood that they had increased durability than bricks constructed from plain clay. This can be explained due to the increased resistance in sheer stress because of the introduction of friction between the hay and clay.

The earliest recollection of a composite material was in 3400 B.C in Mesopotamia which is located in modern Iraq. The Mesopotamians used to glue wood strips on top of each other at some angles, essentially creating plywood. Later on, in around 2200 B.C. the Egyptians used to create death masks by soaking linen and papyrus in plaster. Another breakthrough was the combination of wood, bamboo, bone, cattle tendons, horn, and silk bonded with pine resin by Mongols, in order to manufacture composite bows that were extremely effective at the time. Following the industrial revolution, synthetic resins started to take a solid form by using polymerisation. In the 1900s this new-found knowledge about chemicals led to the creation of various plastics such as polyester, phenolic and vinyl. Synthetics then started to be developed, Bakelite was created by the chemist Leo Baekeland. The fact that it did not conduct electricity

and was heat resistant meant it could be widely used across many industries.

The 1930s was an incredibly important time for the advancement of composites. Glass fiber was introduced by Owens Corning who also started the first fiber reinforced polymer (FRP) industry. The resins engineered during this era are still used to this day and, in 1936, unsaturated polyester resins were patented. Two years later, higher performance resin systems became accessible and in 1960 Boron high stiffness fibers allowed for a greater stiffness to weight ration, making Boron fibers widely applicable in the aviation industry. In 1964 carbon fibers were introduced in the market which even now find great use in all different kind of industries that require great strength to weight ratio, such as aerospace engineering. Aramid fibers (Kevlar) were then discovered in 1971. These have specific stiffness and really good strength to weight ratio, making them ideal for use in the naval, aviation, aerospace, and many more industries.

2.2 Carbon Fiber Composites

Carbon fibers are fibers comprised mostly by carbon atoms that have a diameter between 5 to 10 micrometers. Carbon fibers exhibit high stiffness, high tensile strength, high chemical resistance, and resistance to heat while being very lightweight. For the reasons above, the carbon fibers are applied widely in multiple industries, such as aviation, aerospace, civil engineering, automotive industry, military, spots and many other. They are produced by bonding together crystals with a crystal alignment parallel to the long axis of the fiber. This lattice symmetry allows for great directional high strength to weight ratio. Carbon fibers by themselves are brittle; for that reason, they are combined with other materials to form a composite structure. They are generally manufactured from polymeric precursor materials such as polyacrylonitrile (PAN), cellulose, pitch and polyvinylcloride. PAN based carbon fibers are the most popular due to their good strength and modulus properties, however pitch-based carbon fibers can be used for a better modulus to weight ratio.

Although, the widespread of carbon fibers is relatively new, the idea of fibers made of carbon molecule chains exists for about 150 years [Friedel and Israel, 2010]. Thomas Alva Edison

patent the use of carbon fibers as filament material for his electric lamp. After about unsuccessfully trying more than 1500 different materials and substances (including the hair of a Scotsman's Beard), Edison decided to test a carbonized loop of ordinary cotton which managed to glow for more than half a day. This was later replaced by *Bristol Cardboard* which was capable of glowing for 170 hours.

Edison took out a UK patent on November 10^{th} 1875 [Park, 1999]. A year later, a UK provisional patent was taken out by J.W. Swann for lamp filaments made of carbon [Swann,]. These were the first recollections of patents concerning carbon fibers.

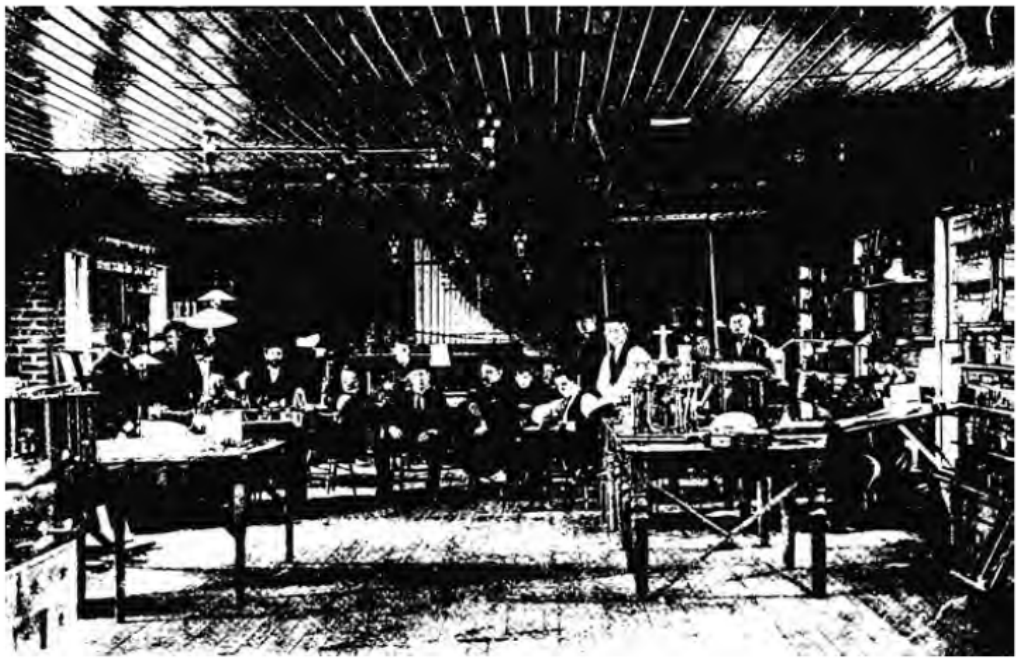

Figure 1: Edison with his team of scientific men at the Menlo Park R&D facility in New Jersey taken in 1876. Edison is seated, wearing cap, and sixth from the left. Note the pipe organ at the back, the focal point for after-hours singing and beer drinking [Source: The Edison Birthplace Museum, Milan, Ohio].

The first example of an oxidized polyacrylonitrile (PAN) carbon fiber was developed was developed by R.C.Houtz [Houtz, 1950] in the 1950s. They were made from *Orlon* when heated at 200^{o}C for 16-20 hours. Polyancrylonitrile polymers have a continuous carbon backbone and the nitrile groups are ideally placed that when crystallized, they produce a ladder polymer. Acrylonitrile (CH_2=CHCN) is the backbone of PAN carbon fibers; it is a colorless volatile liquid with a pungent, onion-like odor with a carbon content of 67.9%. Acrylic fibers, in order to be appropriate for the use of carbon fibers, must have a content of acrylonitrile monomer

exceeding 85%.

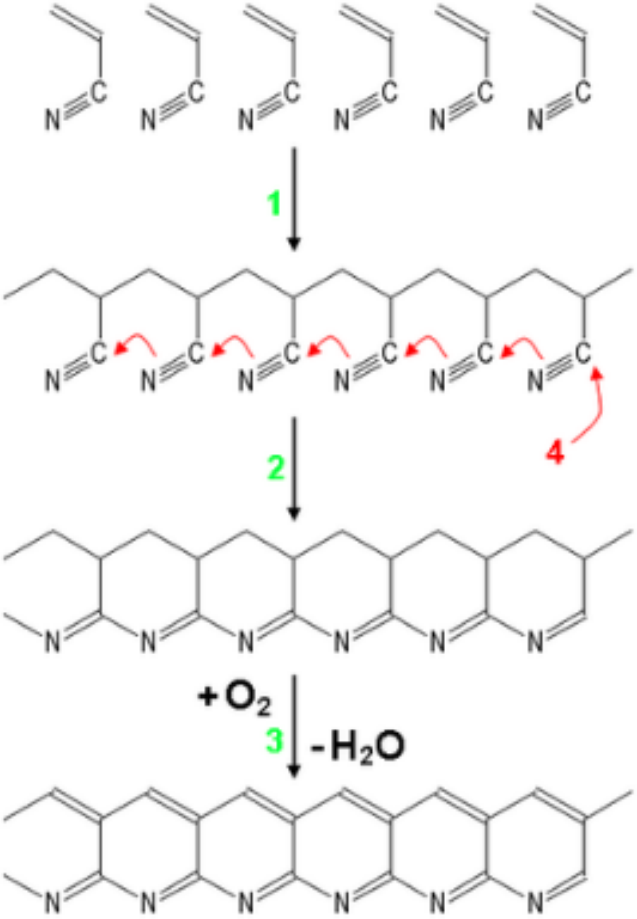

Figure 2: Synthesis od carbon fiber from polyacrylonitride (PAN):

1. Polymerization of acrylonitrile to PAN.
2. Cyclization during the low-temperature process.
3. High-temperature oxidative treatment of carbonization (hydrogen is removed). After this process of graphitization starts where nitrogen is removed and chains are joined into graphite planes.

For synthetic polymers such as PAN, the precursor is spun into filament yarns by mechanical and chemical means thus, allowing the alignment of the polymer molecules in such a way as to enhance the final properties of the carbon fiber. After drawing or spinning, the polymer filament yarns are headed to remove non carbon items in a process called carbonization effectively, producing the final carbon fiber.

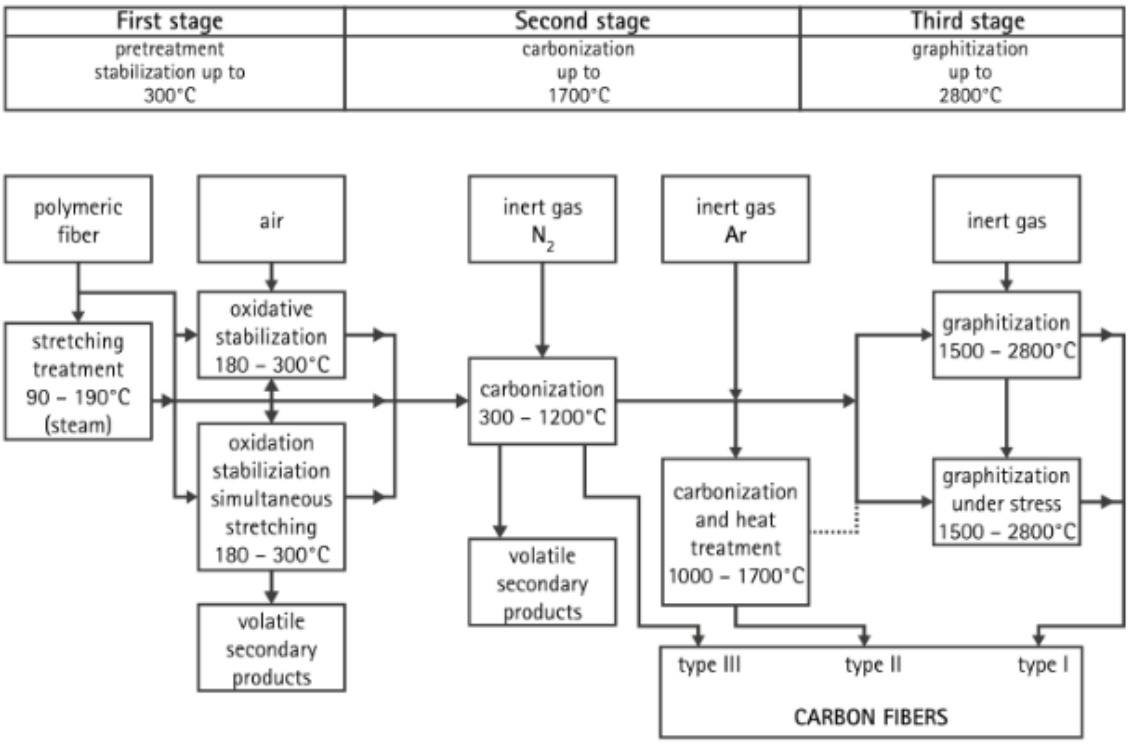

Figure 3: Process of creating carbon fibers

To be more precise, after the construction of PAN polymeric fibers, they are heated at a temperature between 180^{o}C and 300^{o}C in order to break the hydrogen bonds and oxidize the material. The then oxidized fibers are reheated at about 2000^{o}C in a furnace surrounded by an inert atmosphere (for example Argon) which results to graphitization of the material. When reheated, the chains bond together, forming sheets of graphene (ladder polymers) which eventually merge to a single columnar filament with a carbon content exceeding 93%. Lower grade carbon fibers can be constructed from pitch or rayon polymers, instead of polyacrylonitride. Further improvement of the properties of the fibers can occur from treatment processes such as carbonization which allows the fibers to exhibit directional tensile strength exceeding 5,650 Mpa.

Carbon fiber is stronger than steel but lighter than aluminum. Carbon fiber is roughly five times stronger than steel and two times stiffer (some types are even 8 times stronger), and due to this, it is often used as a replacement for metal alloys in places where metal just is not strong enough .The biggest requirement of any high-performance racing car, motorbike or powerboat construction is that it should be strong and lightweight. Carbon fiber has been approved as the

best material for the job. In a drive shaft application, it can be as much as 4 times as strong as steel and it manages to be 40% lighter than aluminum. Cars like the McLaren MP4-12c, being able to accelerate from 0-62Mph in just 3.3 seconds and having a top speed of 205Mph, would not have been able to be made if it were not for its fully Carbon fiber composite chassis that lies underneath.

Many rival companies constantly compete to produce high-performance equipment and it utilizes the physical property of carbon fiber. For example, in golf, the traditional materials such as steel used for the shaft of a golf club are being replaced in favor of carbon fiber as it produces a lightweight club, with the benefit of low torque. Tennis is another sport where the same knowledge is being used to create light, strong rackets. Carbon fiber and other composite materials are being used in the development of musical instruments. Carbon fiber has also an advantage in science, one of the main use is carbon fiber electrode.

Carbon fiber is used in the aerospace industry, where it is used to make lighter and stronger plane parts that can achieve much more than their metal alloy counterparts ever could. However Carbon fiber is not only used in the aerospace industry, In fact, Carbon fiber is used as a substitute for metals in many things that are more down to earth, such as boats, bulletproof suits,computers, R/C helicopters, and many other products.

They are also increasingly used in wind turbines, aerospace (commercial and military aircraft, space launch vehicles), and pressure vessel industries for improved strength to weight and stiffness. Their demand in the aviation and automotive industries is growing fast, especially in Asia.

The latest development in carbon fiber expertise is tiny carbon tubes called nanotubes. These hollow tubes, some as minor as 0.00004 in (0.001 mm) in diameter, have exceptional mechanical and electrical properties that may be useful in making new high-strength fibers, submicroscopic test tubes, or conceivably new semiconductor materials for integrated circuits. The potential of carbon fiber is almost limitless.

Carbon fiber is a very nice material to work with and has several advantages but like any other product also has some disadvantages. The great disadvantage is that carbon fiber is actually

very brittle. This means that though it is durable when it breaks it often breaks devastatingly. The disadvantage of using carbon fiber is that you need a mold if you want to make a decent product, making a mold is not always easy and you often need the help of some specialist. Another drawback is the amount of carbon fiber, it is very expensive. The material is very light in weight and strong but you have to pay a big amount of cash to be able to use it in your goods. Its environmentally unfavorable, firstly it smudges it while manufacturing and again while degrading. It has only one color and because of its expensiveness, nobody wants to hide it in any other color. Carbon fiber is not easy biodegradable yet like you can salvage steel and other materials. It is a little bit harmful to the human body as it causes some form of cancer to the lungs

2.3 Typical defects of composite structures

Flaws found in composite materials can be categorized with regard to which component of the structure was damaged, or the time frame of the damage occurrence in its lifecycle. Composite flaws can occur:

- in fibers or fiber distribution,
- in the matrix or fiber-matrix bond,
- during production,
- during service.

Fibers reinforce the composite and great care must be taken to ensure the correct type and grade of fiber is used for each application in order to achieve the desired properties. Proper alignment and correct fiber distribution is also important in order to achieve the desired directional properties. Furthermore, fibers are generally brittle and are prone to breaking, resulting in an overall reduced strength of the final structure and possibly stress concentrations.

Most common problems found in matrices are caused by incorrect storage of the resins and polymers. Foreign contamination, humidity, and incorrect storage conditions can undermine the matrix or increase porosity. Voids can also occur from trapped air during the manufacturing process. Whatever the cause of pores and voids may be, they can cause internal stress concentrations and compromise the mechanical properties of the structure. This can result to even more severe issues such as delaminations and eventually total failure.

3 Damage detection methods

The simplest and most accurate way of testing materials and components is generally to test them to destruction. Destructive testing (DT) is used to determine the physical properties of materials and components. It can reveal useful information about characteristics of materials, including ductility, tensile strength, fracture toughness but also determine the existence or not of flaws in a structure. Obviously, destructive testing is not always possible or desirable when testing parts and materials destined for, or already in use.

Instead, non-destructive methods are implemented to determine the state of the structure. The first and possibly the most powerful practice when determining the state of a structure is visual inspection. Cracks, corrosion and misalignment will often be an indication of a problem. Acoustic emission testing, is an other method. This is the application of an abrupt force to the test object, a tap-test and the analysis of the results. This analysis could be as simple as listening to the sound or using multiple sensors to record the resulting stress waves and small deformations that occur. Other techniques are liquid penetrant testing, radiography, leak, ultrasonic, Eddy-current, thermal testing, and many others.

These methods although more practical, do not always provide accurate conclusions. As a result, extensive research is constantly being done to improve the reliability of non-destructive testing (NDT) and to invent new methods.

For this thesis, the concept of tap testing is being researched to expand on the idea that anomalies, such as cracks or air inclusions, cause increased scattering of elastic waves traveling through the medium. This in term results, overtime, in an increase of the wave complication. The tool proposed to quantify that complication is Shannon's informational entropy [Shannon, 1948].

3.1 Visual Inspection

When examining a structure, the initial examination is visual. Geometrical defects, pores in welding, large cracks, groves, misalignment, as well as the overall condition of the structure can give an indication for its health. A visual inspection can be conducted with or without the use of optical aids. For example, when examining a welded joint, a small magnifying lens (2-4x) can be used. A *"borescope"* is an other optical system, shown in *figure 4* with its own light source that allows the inspector to see a magnified view of otherwise inaccessible surfaces.

Figure 4: BR100: Video Borescope Inspection Camera

3.2 Radiography

X-Rays and gamma-rays are electromagnetic radiation, which although are of the same physical nature as visible light, infrared, ultraviolet and radio waves, have a much shorter wavelength which allows them to penetrate more surfaces and structures. By placing a photographic plate on the other side of the specimen the investigator can detect discrepancies in the structure. This is because more radiation will pass through a region of the specimen where there is cavity

than if it was a solid structure, allowing for brighter areas in the photographic film.

Generally, a simple radiograph will not provide adequate information concerning the location of cavities (although stereoradiography can), only inform about the existence of them. Radiography can also detect inclusions, considering they have a different absorption rate than the material of the specimen. *Figure 5* for example shows a radiography inspection of a weld, identifying multiple problems.

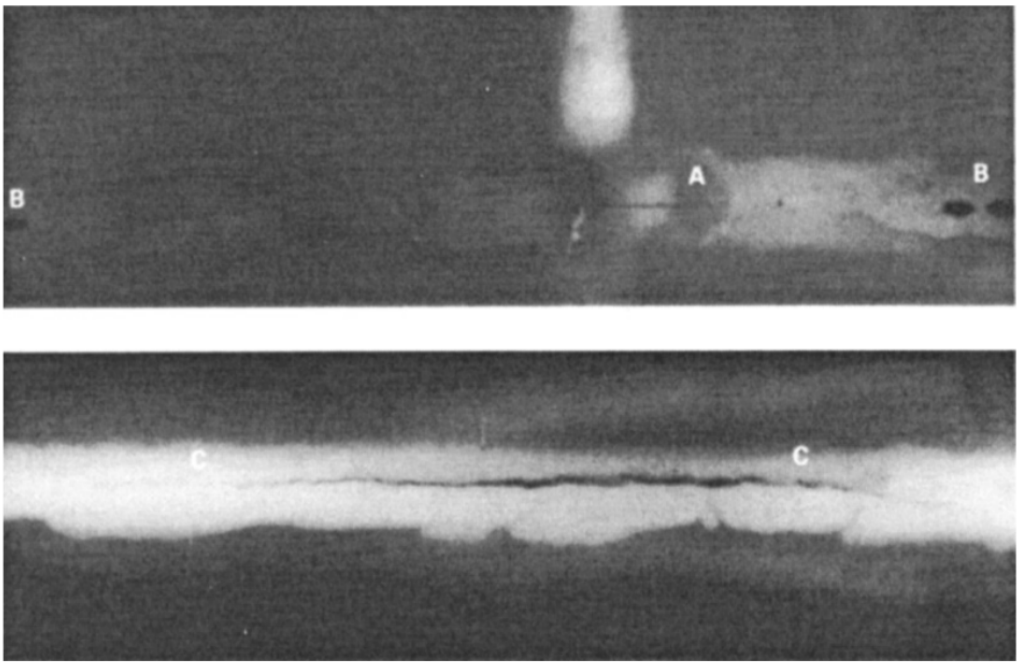

Figure 5: Radiography of a weld, identifying 4 problems [Halmshaw, 1996]:

A lack of root penetration;
B deep gas cavities;
C longitudinal crack.

Radiography on film produces a permanent record, with an image which is normally easy to interpret. Techniques are well developed for straight forward applications, are well documented, and do not require great skill to apply them. Radiography can be applied to all sorts of different structures, welds in any material - copper, austenitic steels, plastics - up to the thickness limits of the particular equipment, and up to a maximum of about 500mm of steel. Radiography is furthermore, one of the most popular inspection methods for composite materials, including carbon fiber structures.

However great radiography can be, it has several drawbacks which limit its use. The most

important drawback is cost; for example, the radiography of thick ferrous materials (>150mm) requires very expensive equipment, and subsequently, the laboratories needed to house such equipment are also expensive. Another limitation comes in the form of its inability to detect, with certainty, tight cracks, small cracks and other planar defects lying at an angle to the radiation beam, because their detection depends on the crack opening width (the separation of the crack faces) and the crack-to-radiation beam angle, as well as on the crack height and crack length. Concerns also arise about the safety of the inspectors from radiation, who need to follow strict protocols to ensure their wellbeing.

3.3 Ultrasonic Inspection

Most ultrasonic testing (UT) is done by moving a small probe (transducer) over the inspected surface of the specimen. The transducer then sends mechanical vibrations which resembles sound waves (generally with a frequency ranging between 500kHz and 20MHz) which pass through the object and get reflected back from any flaw. The transmitting probe also acts as a receiver which detects backscattering from the flaws and displays them in an oscilloscope screen for the inspector.

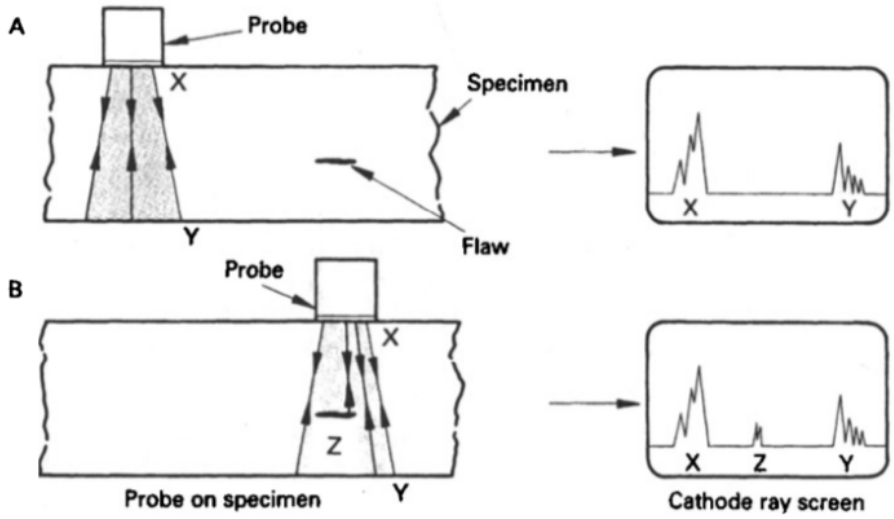

Figure 6: The principle of ultrasonic flaw detection, using a single wave probe and A-scan on oscilloscope display screen [Halmshaw, 1996].

Ultrasonic testing is also widely used for testing composite structures because it enables highly accurate results for locating and sizing flaws, cracks, voids and other defects.

Ultrasonic testing allows for

- high-speed scans,
- high resolution,
- high accuracy,
- the ability to detect a variety of flaws, including cracks, voids, disbonds and inclusions,
- the capability of sizing defects,
- repeatability,
- reliability,
- versatility,
- the ability to be used for items of all different sizes,
- the ability to be automated,
- suitability for an assembly line where the same part design needs to be tested repeatedly,
- accessibility,
- and finally it has no risk associated with the method.

3.4 Magnetic Particles

Magnetic particle testing is an other method for detecting surface cracks in ferromagnetic materials with wide applications in welding inspection. It can also detect sub-surface cracks, but only under very specific conditions. This method is based on the principle that a magnetized

specimen produces magnetic lines. Should those lines get interrupted by a geometric discontinuity, for example a crack or a cavity, then secondary magnetic poles are created at the faces of it. Magnetic particles, by form of a powder or a liquid suspension, are then applied in the surface of the examined object following the magnetic lines, thus revealing any surface cracks. Magnetic particle testing cannot be used in composite materials, since they exhibit no magnetic properties.

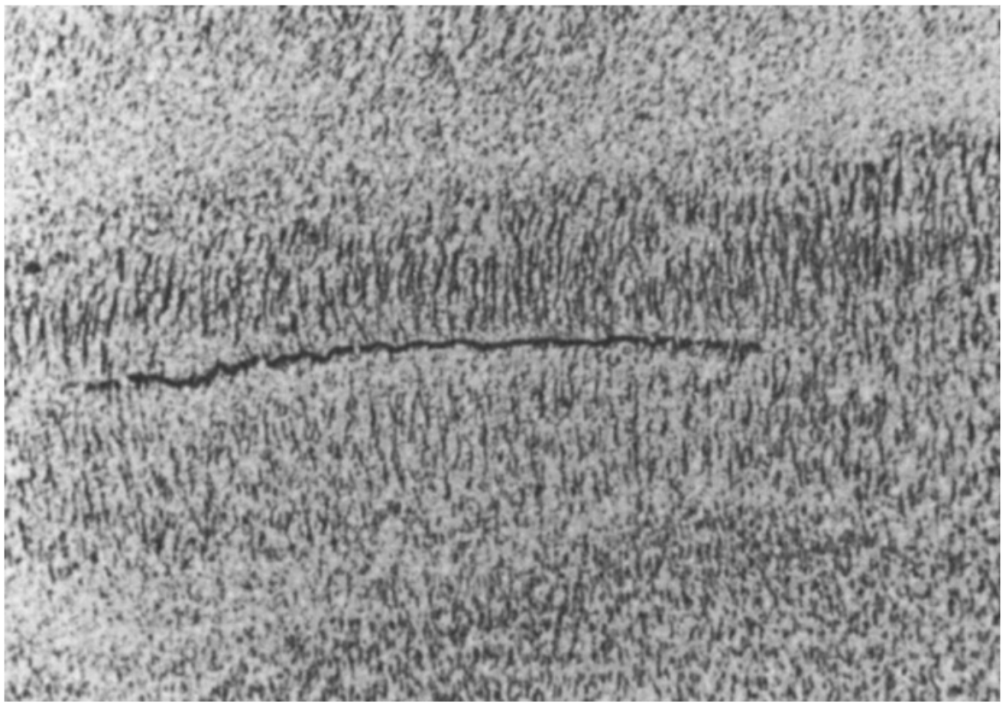

Figure 7: Magnetic particle test indicating longitudinal crack in weld [Halmshaw, 1996].

3.5 Penetrant Liquids

The idea of penetrant liquid testing is that liquids get applied on the examined surface. These liquids because of their low viscosity soak into surface-breaking cracks and cavities. The surplus liquids are then wiped, thus removing them from the surface, making the cracks and cavities visible since they are filled with the liquid. These liquids are generally either fluorescent materials which are visible using a UV light, or dye penetrants, which give a coloured indication of the cracks.

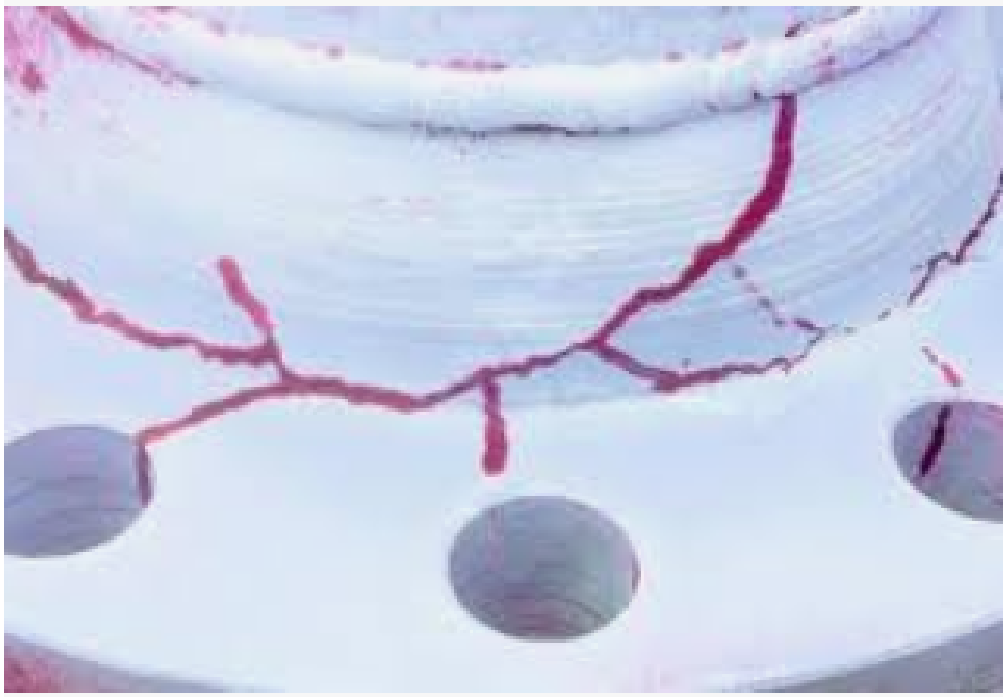

Figure 8: Dye/Liquid Penetrant Inspection [Halmshaw, 1996].

Penetrant liquids are widely used in metals and welding and have a more limited use in composite structures.

3.6 Electrical methods

Some electrical testing methods are the eddy current and potential drop methods of testing for crack depth measurement. Such testing methods can only be applied to structures that conduct electricity.

3.6.1 Eddy Current Method

Eddy current testing is based on Faraday's law of induction. They essentially are closed loops of electrical current induced within electrical conductors when a change in the magnetic field occurs. Eddy current testing can be carried out on any material which conducts electricity by placing a coil which carries an alternating current near the examined object. According

to Faraday's law of induction, eddy currents occur inside the specimen which in turn produce a current in a secondary coil or affect the current in the primary coil. Any flaws inside the structure disrupt the flow of eddy currents and in turn the electrical flow of the receiving coils, thus indicating the existence of a geometric discontinuity.The primary and search coils may be on opposite sides of a thin sheet specimen, may be wound coaxially, or may be separate side-by-side coils. The coils may be annular (encircling) through which tubular specimens are passed, wound on internal bobbins to pass through tubing, or in the form of a single transmitter-receiver coil.

The method is highly reliable on the metallurgical condition of the specimen and especially on its permeability and conductivity, as well as its dimensions. The inspector should bare the above in mind when adjusting the voltage parameter of the testing. Should eddy current testing be done correctly, where the geometry and the metallurgical state are accurately controlled, eddy current testing can be a very sensitive method of finding flaws.

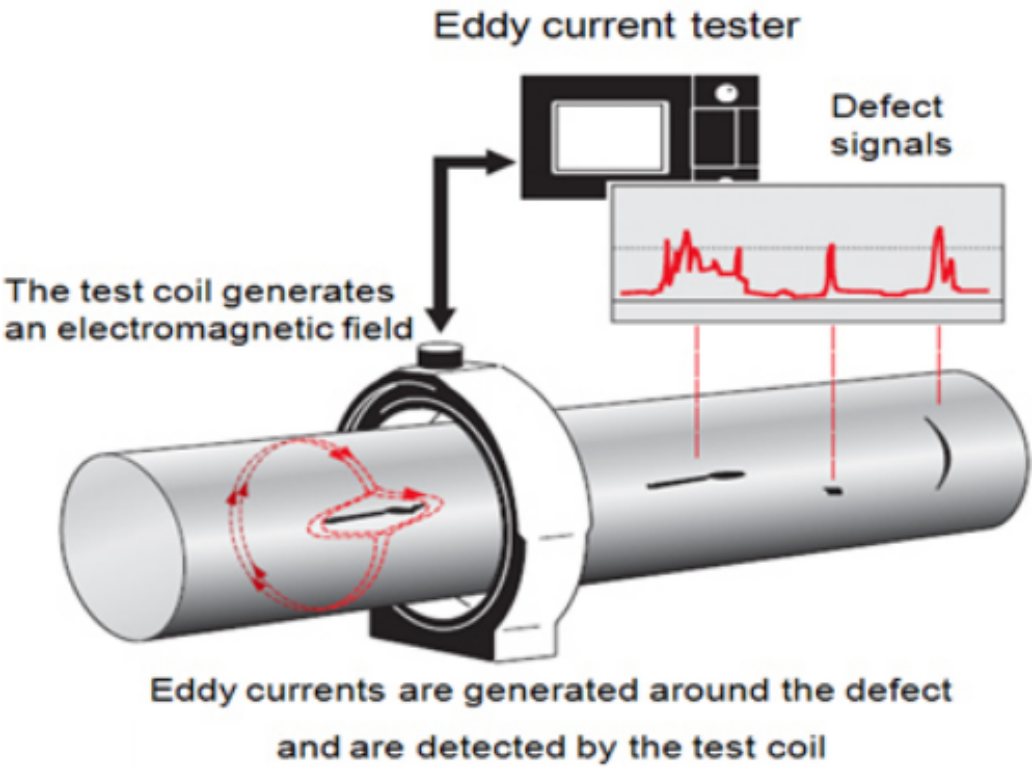

Figure 9: Eddy current Testing example of a shaft [Halmshaw, 1996].

3.6.2 Voltage Drop Methods

The voltage drop method essentially takes advantage of the fact that a crack or cavity has a higher electrical resistance than the metal. When applying a voltage difference across the metal specimen, an electric current will flow. When encountering a cavity or crack, because of the increase in resistance, the voltage difference will drop. A voltometer then reads that drop in voltage difference, indicating a problem with the structure, as shown in (*figure 10*). In practice, the metal is such a good conductor that the changes are very small and almost impossible to measure, but, if a second pair of contacts with a small (fixed) spacing is placed first across the crack and then across sound metal, the two voltage readings on this search probe will be different, and this difference will depend on the height of the crack. As a result, a special circuitry is needed to assess the readings of the voltometer and conclude about the existence or nonexistence of cracks and cavities.

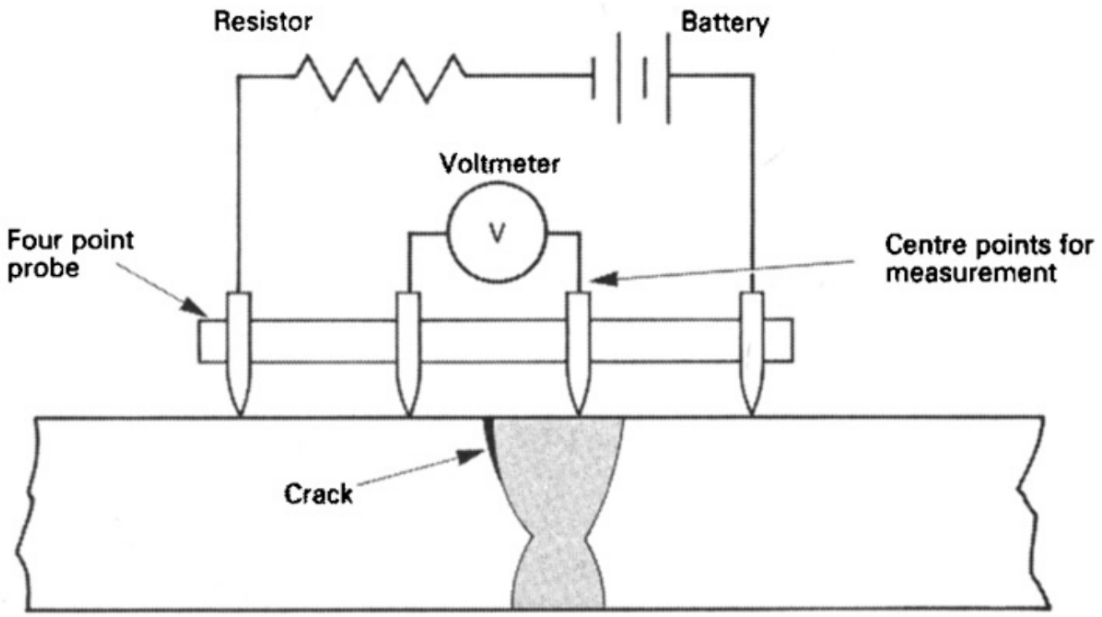

Figure 10: Four-probe contact potential-drop method. The outer probes produce a current flow; the inner pair measure the voltage. [Halmshaw, 1996].

3.7 Acoustic Emission Testing

While most Non destructive testing methods are active, meaning the inspector has to excite the specimen in some way to get an indication of damage, acoustic emission is passive, meaning there is no direct excitement from the inspector. Instead, he just listens for sounds made from the object while under stress. This stress does not need to be internal but instead, can be external.

Whenever an object subject to stress gets plastically deformed, or it get fractured, energy gets released [Prasad and Simha, 2002]. Some of this energy is converted to elastic waves which can then be interpreted as sound pulses of acoustic energy traveling through and can be detected by sensitive transducers positioned on the surface of the examined structure. The phenomenon of sound propagation in materials under stress is called acoustic emission (AE). The intensity and frequency of the acoustic emissions increases rapidly as the structure approaches its fracture limit. Although, the phenomenon of acoustic emission is not yet fully understood, it provides a clear indication of an object approaching fracture. An important note about acoustic emission testing is that the receiving transducer need not be particularly near the source of the emissions, so that the test is not localized. Also, the acoustic emission can be detected in real time, the second it occurs. The emissions will be attenuated in intensity and dispersed between the source of the acoustic emission and the detector.

Acoustic emission can not be applied to all materials. The amount of sound that gets produced can vary enormously between different mediums. As such, in many cases, acoustic emission prove to be futile which along with the interference from background noise causes some controversy over the effectiveness of the method. Nevertheless it remains a potentially powerful method of monitoring large stressed structures (including welded fabrications) during their service life or, for example, during hydrostatic proof testing.

Another important physical phenomenon which must be taken into consideration, when performing an acoustic emission testing, is known as the Kaiser effect. If a polycrystalline material such as a metal is stressed and then relaxed, no new acoustic emissions occurs when the speci-

men is restressed until the stress exceeds the previous maximum stress level.

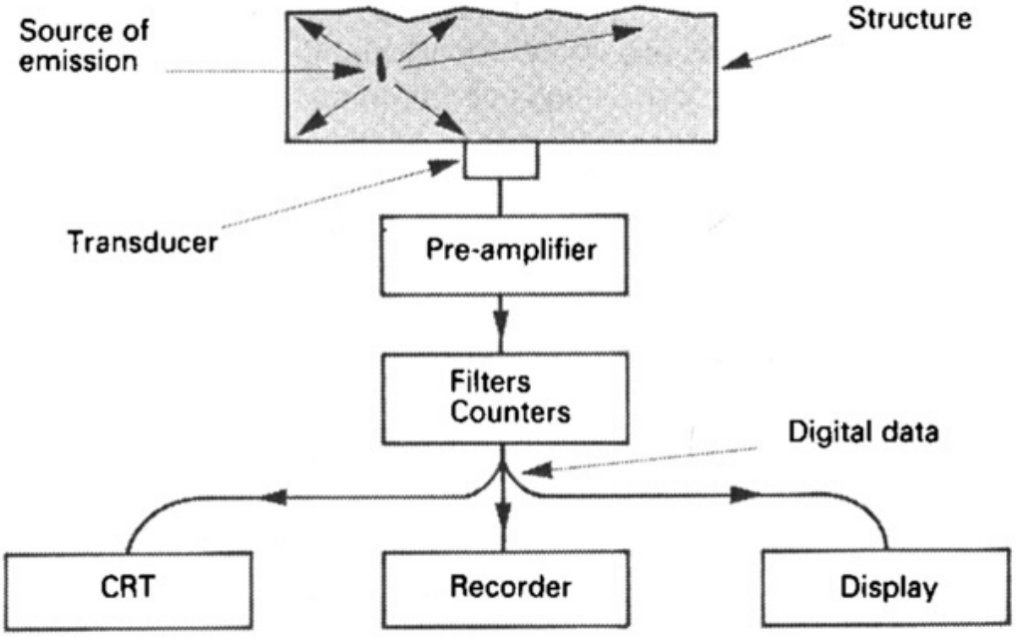

Figure 11: Block diagram of acoustic emission (AE) equipment. [Halmshaw, 1996].

Generally speaking, there are three major groups of applications of AE: the location of defects; the detection of crack propagation; and the monitoring of processes in real time. Acoustic emission testing also, finds applications when inspecting composite structures [Soares et al., 2002]. It is also possible for acoustic emission testing to be combined with wavelet transform to provide more reliable results [Ni and Iwamoto, 2002].

3.8 Optical holography

Optical holography testing can be used to identify microscopic deformation across a surface which could be under stress. It can reveal internal defects in the subsurface of the object by analyzing the light reflected off the surface of the specimen. In order for interference to be minimum, the light needs to be monochromatic, meaning a laser is the only viable option. The most common source is a helium-neon laser, emitting a radiation with a wavelength of 632.8nm. A series of lenses and mirrors is used to create a holographic reconstruction of the object for examination.

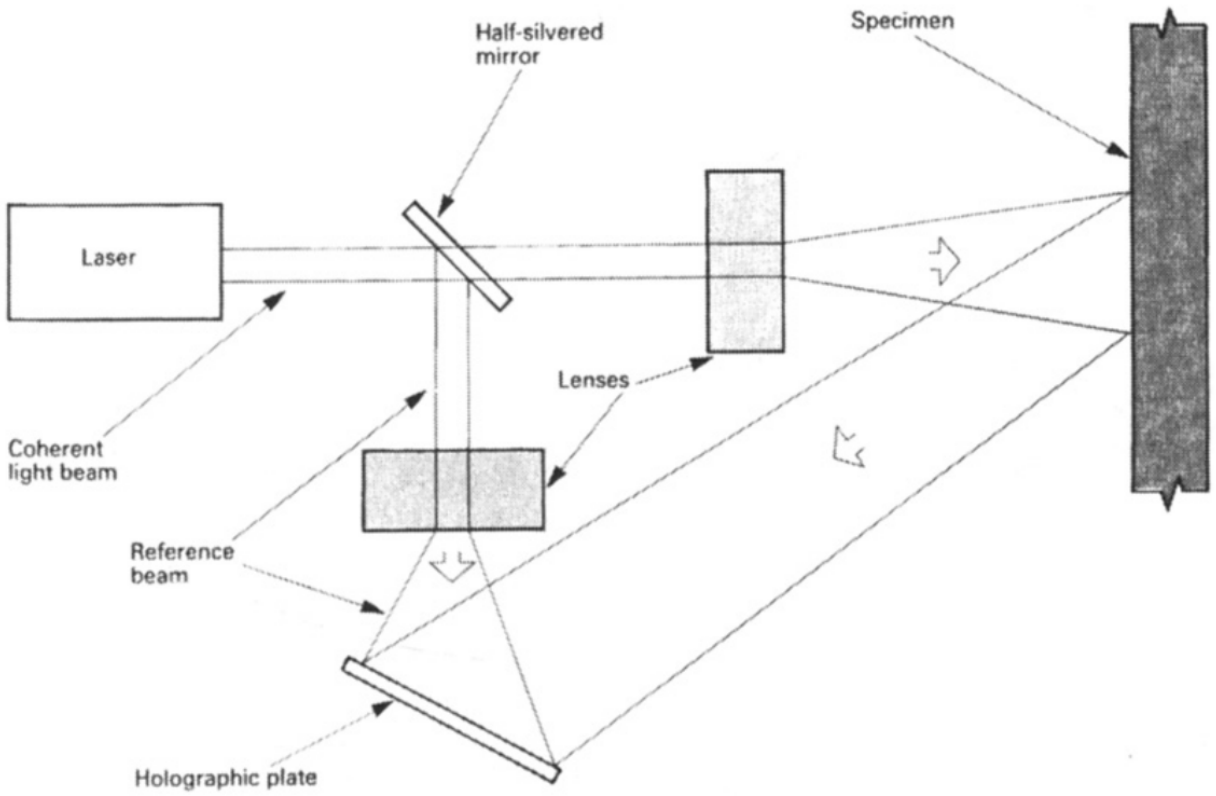

Figure 12: Optical holography for surface deformations.. [Halmshaw, 1996].

3.9 Leak Testing

Many structures need to be designed to withstand pressure, or to be water-tight. In such cases, leak testing is necessary to identify any leakage that could compromise the structure.

4 Theoretical Background

4.1 Bending waves

In experiment of section 6, the specimen is impacted transversely. Therefore, bending waves are generated. Bending waves are a result of a transverse concentrated force spread. For pure bending waves to propagate in a beam the following conditions need to be met:

- The beam should posses longitudinal symmetry,

- The material of the beam should be elastic and have a constant density ρ,

Generally speaking, the equation of motion for flexural (bending) waves in a beam is:

$$\frac{\theta^2 y}{\theta t^2} + c_L^2 K^2 \theta^4 y \theta x^4 = 0 \tag{4.1}$$

Where: $c_L = \sqrt{\frac{E}{\rho}}$ is the speed of a quasi-longitudinal wave (E is Young's modulus).

4.2 Elastic wave diffraction

The meaning of the word diffraction is the deviation of waves from rectilinear paths when not caused by reflection or refraction. The earliest recollection of the word was used in 1665 in the book "Physico-Mathesis du Lumine, Coloribus et Iride" [Grimaldi and Bernia, 1966] by Pr. Francesco Maria Grimaldi when she observed a light beam being slightly bent while passing through the edge of an aperture. The same phenomenon was later observed by Robert Hook and Christen Huygens, although they were initially unable to explain, since if the light propagated

like sound waves, there would be no darkness in shadow regions as light would spread equally. In 1801, Thomas Young discovered the law of interference of light waves, which then led Jean Fresnel to discover the true cause of diffraction. An interference can be explained as two waves that when mixing together destroy (or reinforce) each other, either wholly or partially. In a memoir of his in 1818 on the subject of "Diffraction" he explained that the diffraction is the mutual interference of secondary waves emitting from an aperture. He then introduced the Huygens-Fresnel principle stating that if the incident waves are conceived to be broken up upon arriving at the aperture of a screen, each element can be considered as the center of a secondary disturbance. However, the phase of the motion of each secondary wave is delayed by a quantity corresponding to the distance from its center to the point of observation, the arriving secondary waves interfere with each other, resulting in diffraction.

By the end of the 18th century the equations of sound waves in air had already been developed, although the motion of an elastic aether possessing resistance to both volumetric change and distortion was yet to be understood. That was until Claud Louis-Marie-Hentri Navier presented a molecular theory of elastic body, giving an equation of motion for the displacement of a particle in elastic solids. Later, inspired by his work, Augustine-Louis Cauchy developed the "Mathematical Theory of Elasticity", introducing the notions of strain, stress and their relationship. Following the development of the electromagnetic and quantum theories of light, the elastic solid theory was discarded, until in 1888 Lord Rayleigh in the article "Wave theory of light" [Rayleigh, 1888] stated: "The elastic solid theory , valuable as a piece of purely dynamical reasoning, and probably not without mathematical analogy to the truth, can in optics be regarded only as an illustration.". This was essentially the beginning of the elastic wave theory as it is known now, which applies to all waves in nature, including sound, electromagnetic and elastic waves.

Eventually the George Gabriel Stokes began to investigate the diffraction phenomenon, eventually introducing the general solution for propagation of a disturbance in a medium. Assuming the disturbance was produced by a given disturbance confined to a finite portion of the medium, he eventually derived to the conclusion that when light gets diffracted by the aperture, each element of the aperture acts like a source which generates secondary spherical waves. Rayleigh

inspired by the work of Stokes examined the diffraction of light by small particles, thus introduced the notion of Rayleigh Scattering which states that "When light is scattered by particles which are very small compared with any of the wave lengths, the ration of the amplitude of the vibrations of the scattered and incident light varies inversely as the square of the wave length, and the intensity of the light themselves as the inverse fourth power"; thus providing the answer to the question to why the sky is blue during the day and red during the sunrise and sunset. Perhaps the first definition of scattering can be attributed to Lord Rayleigh who described the scattering wave as "the difference od the total wave filed observed in the presence of an obstacle and the incident wave, then a scatter wave is comprised of the part reflected by the obstacle into the illuminated zone and the part refracted and diffracted by the object into the shadow zone". As a result, scattering and diffraction represent different wave phenomenons, although when not describing molecular physics, they represent the same thing. For sound waves traveling through a medium with sharp edges, the term diffraction prevails, while when a wave encounters a smooth obstacle like a sphere, the term scatter is preferred.

4.3 Wavelet Energy

For a wavelet family $w_{\alpha,b}$ which constitutes an orthogonal basis for $L^2(\mathbb{R})$ the concept of energy can be defined as the sum of squares of the Wavelet Transform coefficients $w(\alpha, b; W, f)$ which are going to called $c_{\alpha,b}$ from here on after (not to be confused with C_w as defined by equation A.18). Therefore, for every scale, the energy is given by:

$$E_\alpha = \sum_b |c_{\alpha,b}|^2 \tag{4.2}$$

However, since the higher the scale, the more wavelet coefficients exist on that scale, energy is normalized by being divided by the number of wavelet coefficients on the examined scale.

$$E_\alpha = \frac{1}{N_j} \sum_b |c_{\alpha,b}|^2 \tag{4.3}$$

Where N_j is the number of wavelet coefficients at scale j, or if examining a segment of the original signal, N_j is the number of wavelet coefficients at scale j that are present in that segment.

Therefore, the total energy of the signal can be obtained as:

$$E_{tot} = \sum E_{\alpha} \tag{4.4}$$

For the j^{th} scale, the wavelet energy ratio is considered as the normalized value:

$$p_j = \frac{E_j}{E_{tot}} \tag{4.5}$$

The ensemble of all wavelet energy ratios p_j for every scale j gives the distribution of energy between all different energy levels (scales).

4.4 Shannon's Entropy

In probability and statistics, the probability *P(A)* of an event A occurring during the performance of an experiment ℓ, can be interpreted as a measure of uncertainty about the occurrence or nonoccurrence of the event A. Expanding on that idea, the quantification of the uncertainty of occurrence or nonoccurrence of any event A_i of a partition P of ℓ is called entropy of the partitioning P. The term entropy derives from thermodynamics as firstly expressed by Rudolf Clausius, [Cropper, 1986] describing entropy as the *transformation-content* meaning the dissipation of energy of a thermodynamic system during its change of state.

Its probabilistic interpretation is attributed to Boltzmann [Sharp and Matschinsky, 2015] as in 1877 he succeeded in measuring the entropy of an ensemble of ideal gas particles in a probabilistic way. However, the explicit relationship between entropy and probability was given by Plank [Planck, 1914]. Shannon then expanded on the idea of entropy to give an economical

description of the properties of long sequences of symbols, and applied the results to a number of basic problems in coding theory and data to introduce the concept of informational entropy transmission [Shannon, 1948].

A heuristic interpretation of Shannon's informational entropy (H) is that it measures how uncertain the outcome of an experiment l, that has n possible outcomes A_i, each with probability p_i, i=1,2,...,n is. H should then have the following characteristics:

- H should be a continuous function of p_i.
- If all p_i are equal, then H should monotonically increase as a function of n.
- If an outcome can be divided into two outcomes, the original outcome should be the weighted sum of each individual values of H.

A function that satisfies those conditions is:

$$H = -K \sum_{i=1}^{n} p_i log p_i \tag{4.6}$$

Where K$\in \mathbb{R}$ is a constant.

For the purpose of damage identification, the impact of K is meaningless, therefore, K=1, or:

$$H = -\sum_{i=1}^{n} p_i log p_i \tag{4.7}$$

As aforementioned, in a heuristic interpretation of entropy, the number H is a measure of the uncertainty of the outcome of an experiment l prior to the execution of the experiment in question. After the execution of the experiment and when its outcomes become known, the uncertainty is removed and the entropy of the partition is equal to the information provided by the experiment about the events A_i.

A more practical description of the notion entropy can be given when considering a distribution $P(A_i),\ p_i = P(\mathbf{x} = x_i),\ \sum_i p_i = 1$. Should for $i = k$, $p_k = 1$, which in term means $p_i = 0,\ i \neq k$,

then there is no uncertainty and as a result, the entropy of the partition is zero (0). On the other hand, if a different distribution $P(A_i)$ statistical dispersion (meaning the distribution is stretched or squeezed), the uncertainty changes. Stretching of the distribution results in an increase of the uncertainty of the distribution with a subsequent increase in its entropy and vise versa for a squeezing of the distribution.

4.5 Wavelet Entropy

Expanding on the notion of informational entropy, Shannon's entropy in the time domain can indicate the uncertainty of a signal; while spectrum entropy (Shannon's entropy in the frequency domain) can measure the complexity of the signal [Zheng-You et al., 2006]. Since wavelet analysis allows multi-resolution in both time and scale, Wavelet Entropy manifests the complexity both in time and scale.

The definition of Wavelet Entropy can be given as follows:

Given $E = E_1, E_2, ..., E_N$ the wavelet spectra of the signal as defined by *equation (4.2)*, where each component p_i of the partition is expressed by *equation(4.5)*, the Wavelet Entropy of the signal is defined accordingly to Shannon's informational entropy as:

$$WE = -\sum_i p_i log p_i \tag{4.8}$$

4.5.1 Wavelet Entropy Time Series

For sliding windows, the Wavelet Entropy Time Series is the time series of the Wavelet Entropies defined by *equation (4.8)* for all the coefficients that participate in every time window.

Consider a signal of length $N = 2^k$ transformed using the *Haar* Wavelet Transform and a sliding window of length M with a sliding factor δ. Firstly the coefficients participating in that segment need to be identified. Every wavelet coefficient contributing is considered to be

participating in the window.

As mentioned in section A.2.4, scale j has 2^j coefficients, each expanding for $N/2^j$ samples. Therefore, every coefficient b_j, k corresponds to all points with an index between $kN/2^j$ and $(k+1)N/2^j$.

For a window starting at point l and finishing at point $l+N$, every coefficient b_j, k, where the $[kN/2^j,(k+1)N/2^j]$ intersects with $[l,l+N]$ is considered to be participating in the calculation of the Wavelet Entropy of the window. The conditions for the above are:

- $l \leqslant kN/2^j \leqslant l+N$ or,
- $l \leqslant (k+1)N/2^j \leqslant l+N$ or,
- $kN/2^j \leqslant l \leqslant (k+1)N/2^j$ or,
- $kN/2^j \leqslant l+N \leqslant (k+1)N/2^j$

Therefore, for a window between l and $l+N$, every coefficient b_j, k where either of these conditions are met is considered to participate in the window.

For every window then, the Wavelet Entropy of the window is calculated using *equation (4.8)*. The time series of those Wavelet Entropies, is the Wavelet Entropy Time Series.

Appendix A, B present two numerical simulations of signals analyzed using Wavelet Entropy Time Series.

5 Numerical simulations of examples to better understand the concept of wavelet entropy

For our better understanding of the concept of wavelet entropy, 3 numerical simulations were modeled.

5.1 Numerical simulation of Wavelet Entropy identifying a shift in the dynamics of a triple harmonic signal

The concept of wavelet entropy can better be explained by a numerical simulation. The method discussed in this thesis is applied at a signal $f(t)$ that has an abrupt but subtle change in its dynamics.

The function *f(t)* was created and sampled with a sampling frequency of $512Hz$ for $16s$ for a total of $N = 8192 = 2^{13}$ samples. f is comprised fully out of pure sin waves with an instantaneous frequency shift at t=5s, as shown by *equation 5.1.*

$$f(t) = \begin{cases} sin(2\pi t) + sin(4\pi t) + sin(10\pi t), & (0 \leqslant t \leqslant 5) \\ sin(1.998\pi t) + sin(4\pi t) + sin(10\pi t), & (5 < t \leqslant 16) \end{cases} \tag{5.1}$$

This harmonic function essentially contains three frequencies at $1Hz$, $2Hz$ and $5Hz$. At the time stamp of $5s$, the first frequency gets decreased by 0.1% while the remainder of the frequencies remain unchanged. As expected, a visual indication of the acquired signal (figure **??**) proves to be effortless. It is near impossible to spot that the shift in the signal's dynamics by pure examination of the output signal, let alone identify the instance of the change.

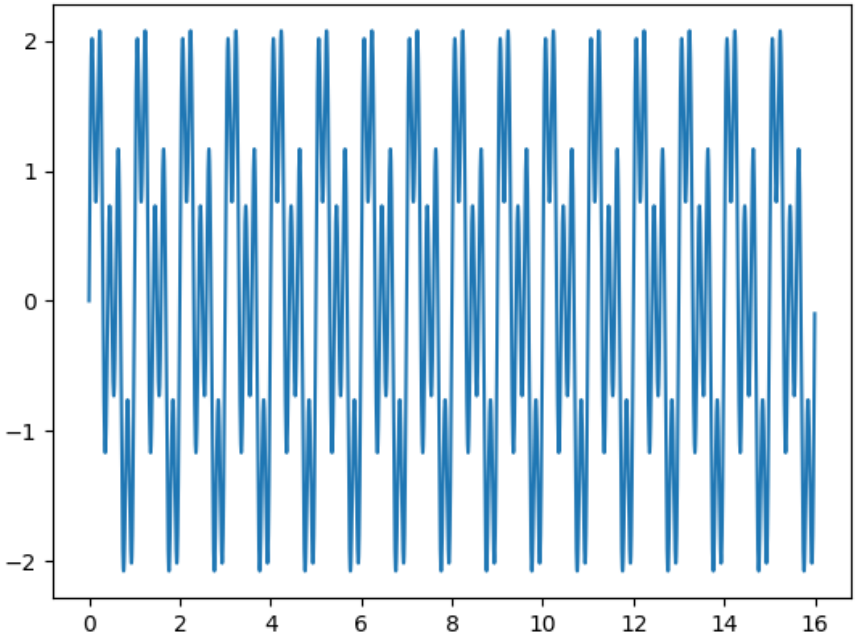

Figure 13: Triple harmonic function f(t), described by equation 5.1.

The power spectrum of the signal $f(t)$ in *figure 14* also reveals little useful information about the shift in the dynamics.

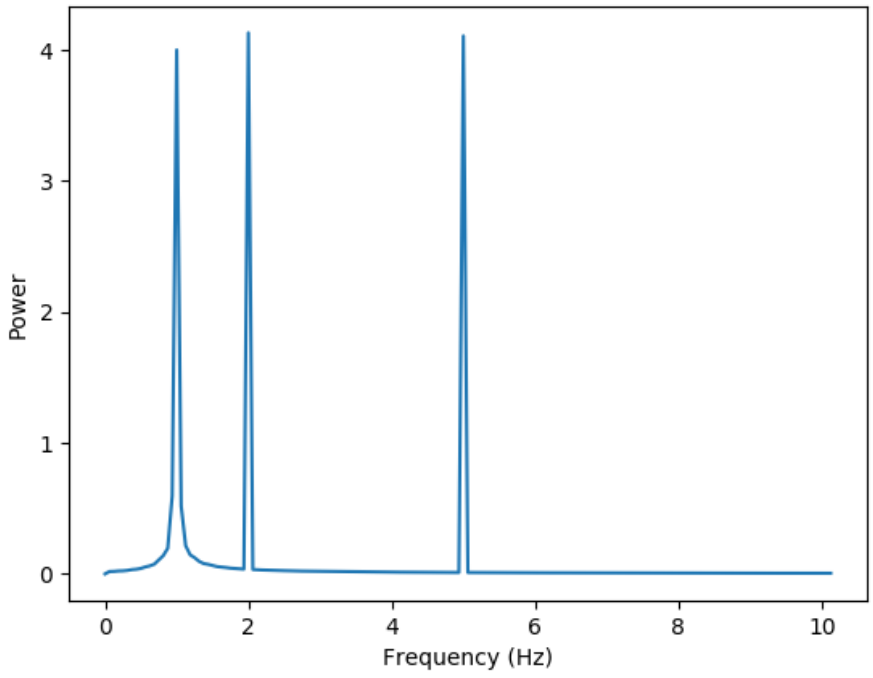

Figure 14: Power spectrum of triple harmonic function f(t).

Although some dispersion around the main frequency $f = 1Hz$ can be seen, we need to remember that this simulation is expressed as a sum of pure sine waves, without any noise or variation which will hardly ever be the case in a normal real world signal. Furthermore, the power spectrum reveals no information concerning the instance of the shift in the dynamics.

The signal has a length of $N = 2^{13}$ samples and a nyquist frequency $f_n = 256Hz$. Therefore, the *Haar* discrete wavelet transform of $f(t)$, as shown by *figure 17*, has 14 scales (-1 to 12) (the signals have been normalized, therefore there is no reason to plot scale -1 which essentially is the mean of the signal).

As discussed in section A.2.4, scale 0 has 1 coefficient, scale 1 has 2, etc, scale n has 2^n coefficients. The higher the scale, the better the resolution in the time domain, while the frequency resolution deteriorates and vice versa (Heisenberg uncertainty principle). Each scale acts as a combination of lowpass (moving average) and highpass (moving difference) filters. As such, the highest scale (12^{th} scale) contains frequencies ranging between $f_n = 256Hz$ and $f_n/2 = 128Hz$ and centered around $f_n/2 + f_n/4 = 192Hz$ with each subsequent scale lowering the frequency band by half. This can be seen in *table 1*.

Scale	No. of Coefficients	Frequency Range (Hz)	Center Frequency (Hz)
12	4096	256 - 128	192
11	2048	128 - 64	96
10	1024	64 - 32	48
9	512	32 - 16	24
8	256	16 - 8	12
7	128	8 - 4	6
6	64	4 - 2	3
5	32	2 - 1	1.5
4	16	1 - 0.5	0.75
3	8	0.5 - 0.25	0.375
2	4	0.25 - 0.125	0.1875
1	2	0.125 - 0.0625	0.09375
0	1	0.0625 - 0	0.03125

Table 1: Frequency-scale correspondence

From the amplitude of *figure 15* we can observe that scales 4-7 have the most contribution to the signal $f(t)$ which is sensible, considering the sine waves comprising the signal.

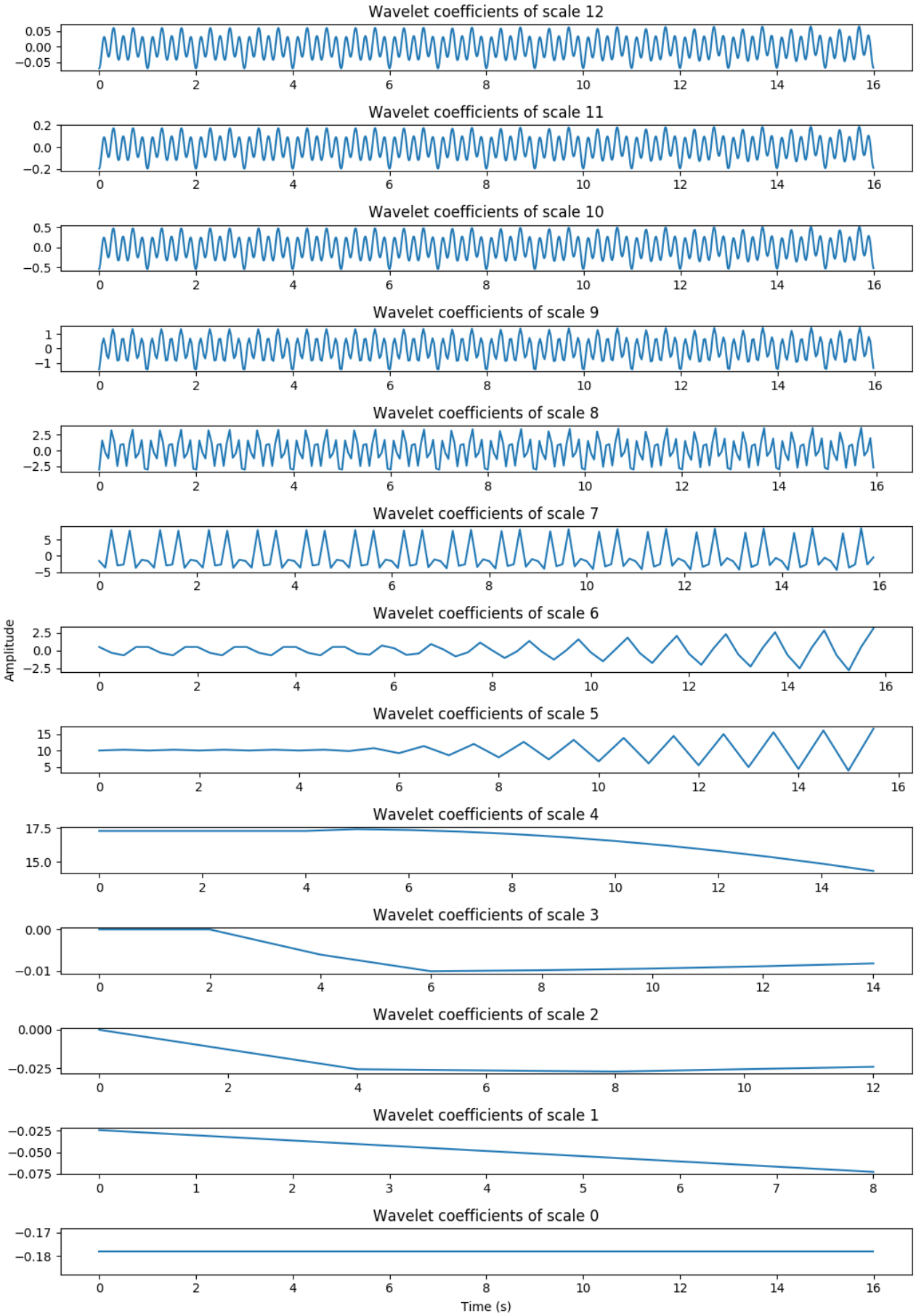

Figure 15: *Haar* Discrete wavelet decomposition of triple harmonic function $f(t)$.

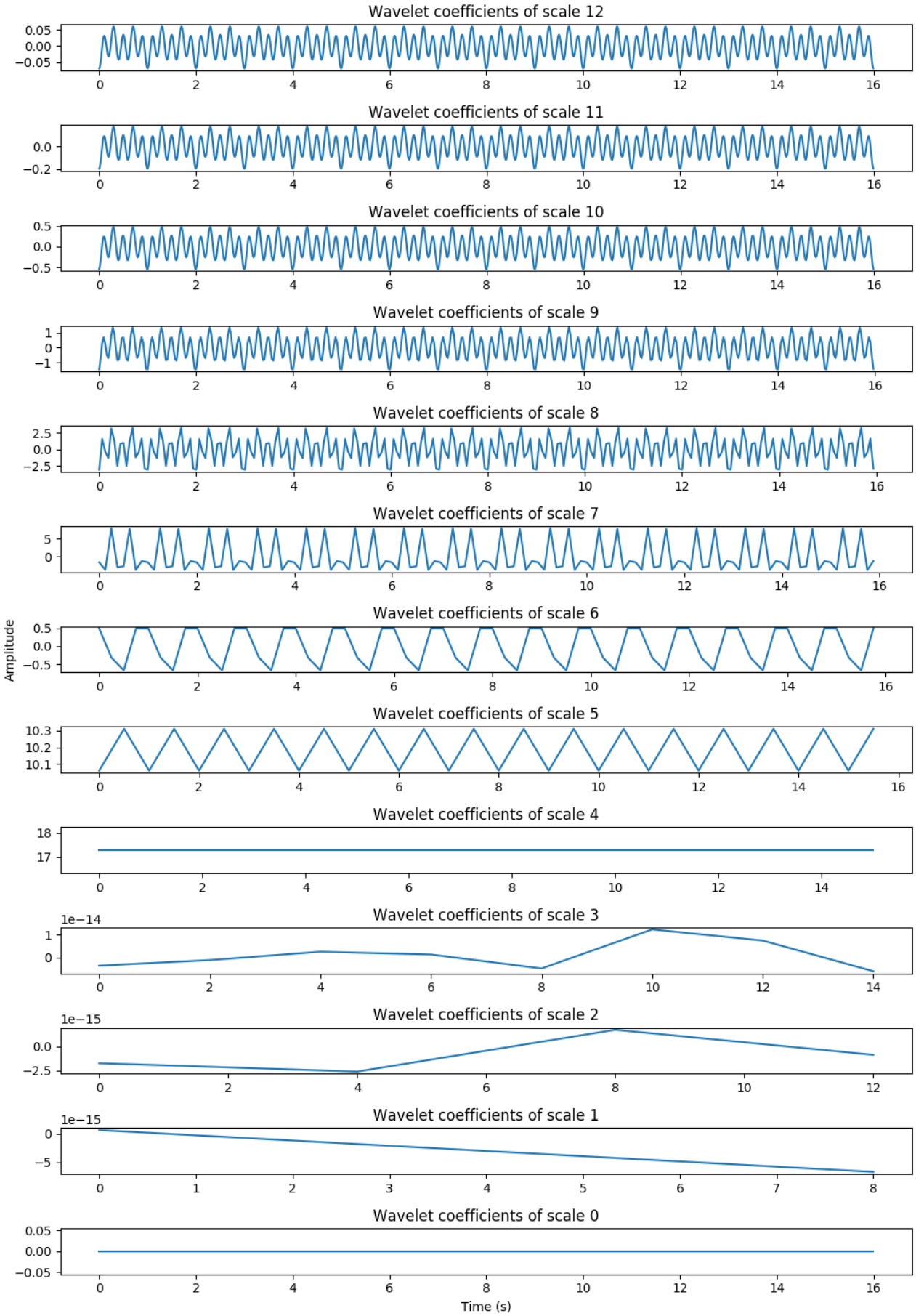

Figure 16: *Haar* Discrete wavelet decomposition of triple harmonic function $g(t)$.

Furthermore, *figure 16* displays the coefficients of a signal $g(t)$ similar to $f(t)$, but without the change in the dynamics it can be concluded that mainly scales 3, 4, 5, 6 detect the change in the dynamics at the 6 second time stamp.

$$g(t) = sin(2\pi t) + sin(4\pi t) + sin(10\pi t), \qquad (0 \leqslant t \leqslant 5) \tag{5.2}$$

By examining *figure 16*, we observe significant high frequency oscillations of the coefficients in the higher scales. Obviously, since $g(t)$ is composed entirely out of 3 sine waves with frequencies 1Hz, 2Hz, and 5Hz there are no high frequency components of the signal. Those oscillations occur due to the *Gibbs* phenomenon [Shim and Volkmer, 1996] [Strang and Nguyen, 1996].

The acceleration attributed to every scale for $f(t)$ can also be seen in figure *17*, the sum of which allows reconstruction of the original signal $f(t)$. The diagram was created by multiplying each coefficient with a *Haar* wavelet, which essentially is the series $\{1, -1\}$.

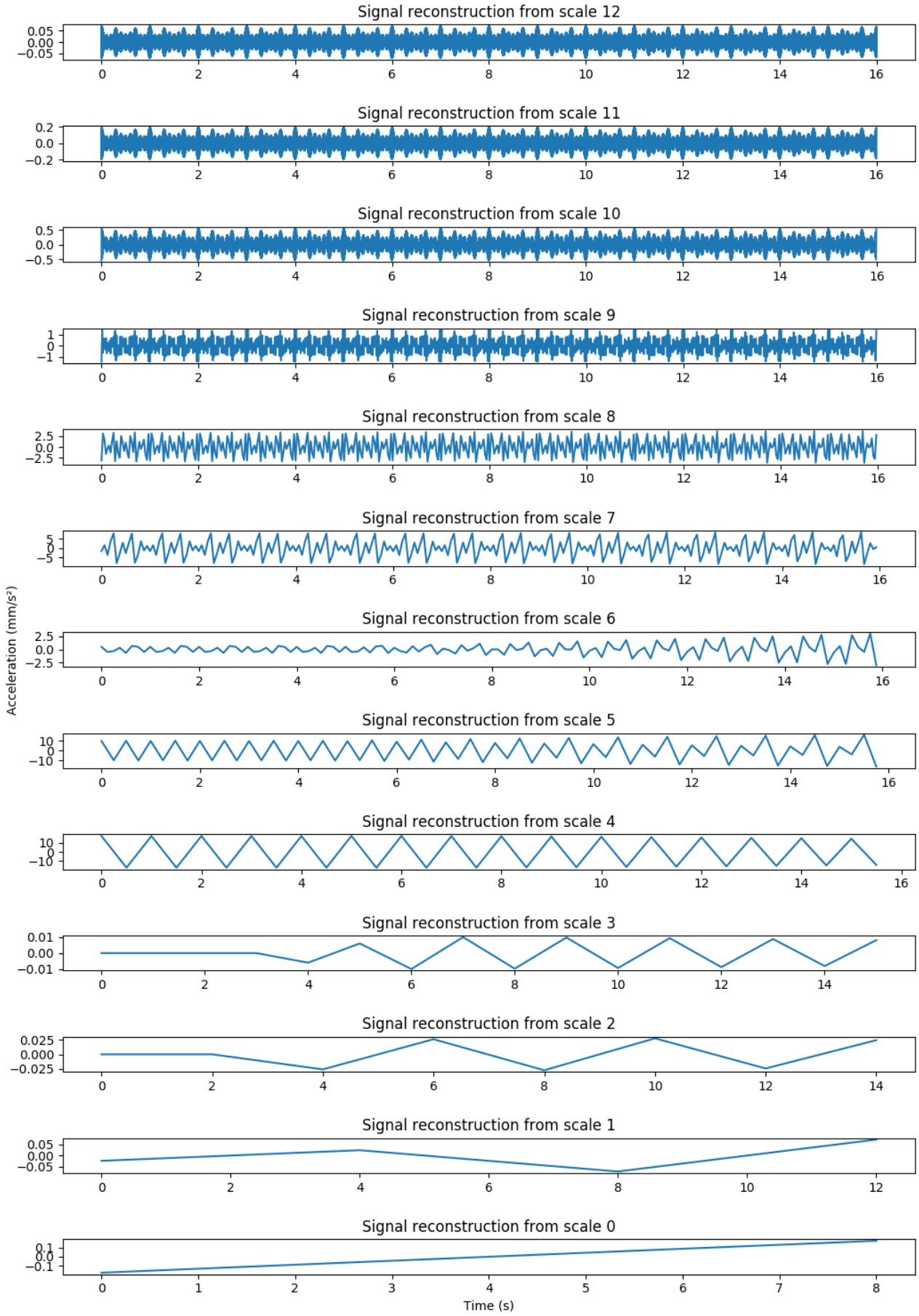

Figure 17: Acceleration attributed to every scale of triple harmonic function $f(t)$.

Although by careful examination of the wavelet coefficients in *figure 15* the shift in the dynamics can be identified, the wavelet entropy time series is much capable at identifying singularities effortlessly. *Figure 18* displays the wavelet entropy time series of the signal $f(t)$ for windows of length 512 samples and a step of 10 samples. It is clearly visible at the change of the dynamics increases the complicatedness of $f(t)$ with and entropy of the transform to experience a gradually increasing trend. The oscillations of the entropy can also be attributed to the *Gibbs* phenomenon.

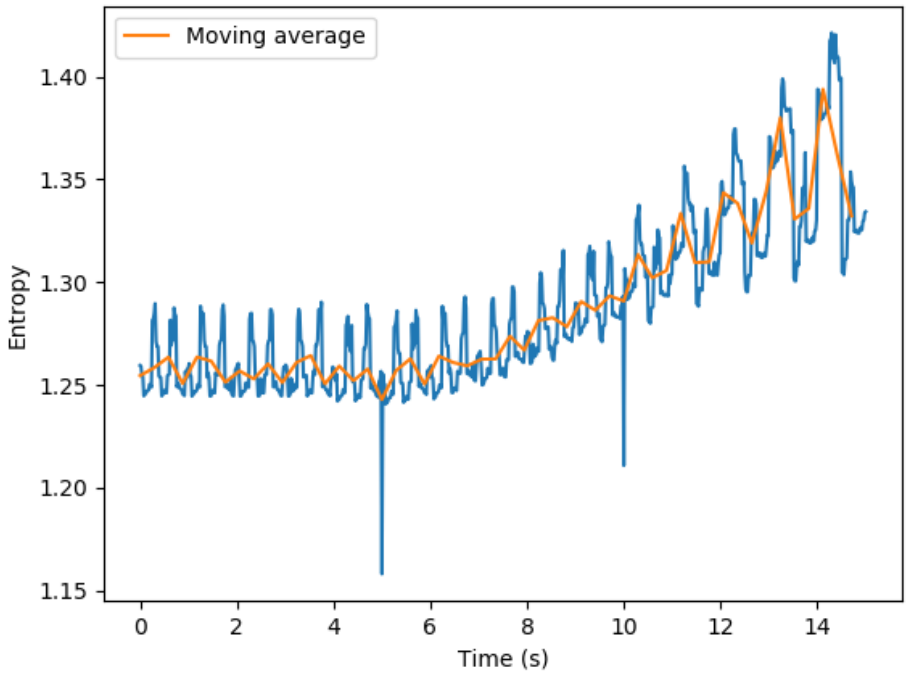

Figure 18: Wavelet time entropy of triple harmonic function f(t), described by equation 5.1.

5.2 Numerical simulation of applying wavelet entropy to system of linear coupled oscillators

In order to better comprehend the concept of wavelet entropy, two additional numerical simulations featuring systems of twenty, coupled, linear, dumped oscillators were numerically modeled. For each model the system is comprised of 20 equal masses (m_i) with spring and linear dumping between each successive mass. The springs have a spring constant k_i, while the linear dumping has a dumping coefficient c.

For a system of coupled, linear, dumped oscillators if the mass m_i gets displaced from its equilibrium position by an amount $\overrightarrow{x_i}$, then the spring at its left exerts a force equal to $-k_{i-1}(\vec{x_i}-\vec{x_{i-1}})$, while the spring to the right exerts a force $-k_i(\vec{x_i}-\vec{x_{i+1}})$. Each linear dumping exerts a force $-(c_{i-1}+c_i)\dot{\vec{x_i}}$. Therefore, the equation of motion for m_i is:

$$m\ddot{\vec{x_i}} = -k_{i-1}(\vec{x_i}-\vec{x_{i-1}}) - k_i(\vec{x_i}-\vec{x_{i+1}}) - 2c\dot{\vec{x_i}} \tag{5.3}$$

As a result, for a system of n masses, the equations of motion are:

$$\begin{cases} m\ddot{\vec{x_1}} + k_0(\vec{x_1}) + k_1(\vec{x_1}-\vec{x_2}) + 2c\dot{\vec{x_1}} = 0 \\ ... \\ m\ddot{\vec{x_i}} + k_{i-1}(\vec{x_i}-\vec{x_{i-1}}) + k_i(\vec{x_i}-\vec{x_{i+1}}) + 2c\dot{\vec{x_i}} = 0 \\ ... \\ m\ddot{\vec{x_n}} + k_{19}(\vec{x_n}-\vec{x_{n-1}}) + k_{20}(\vec{x_n}) + 2c\dot{\vec{x_i}} = 0 \end{cases} \tag{5.4}$$

This system of differential equations can be written in a matrix form as:

$$M\ddot{\vec{X}} + C\dot{\vec{X}} + K\vec{X} = 0 \tag{5.5}$$

Where:

$$M = \begin{bmatrix} m_1 \\ . \\ m_i \\ . \\ m_n \end{bmatrix} \quad , \quad C = \begin{bmatrix} c_0 + c_1 \\ . \\ c_{i-1} + c_i \\ . \\ c_1 9 + c_2 0 \end{bmatrix} \quad , \quad K = \begin{bmatrix} k_0 + k_1 & -k_1 & & \\ & & ... & \\ & -k_{i-1} & k_{i-1} + k_i & -k_i \\ & & ... & \\ & & -k_{19} & k_{19} + k_{20} \end{bmatrix} \tag{5.6}$$

While the matrix $\vec{X}$ is the vector of the displacement:

$$\vec{X} = [\vec{x_1} \quad ... \quad \vec{x_i} \quad ... \quad \vec{x_n}] \tag{5.7}$$

The equation *(5.5)* is a system of n linear second order differential equations. In order for it to be numerically solved, it can be written as an extended system of 2n first degree differential equations, or:

$$M\ddot{\vec{X}} + C\dot{\vec{X}} + K\vec{X} = 0 \Longleftrightarrow \begin{cases} M\dot{\vec{X}_2} + C\vec{X_2} + K\vec{X_1} = 0 \\ \dot{\vec{X}_1} = \vec{X_1} \end{cases} \tag{5.8}$$

This is equivalent to:

$$\begin{bmatrix} \vec{X_1} \\ \vec{X_2} \end{bmatrix}' = \begin{bmatrix} 0 & I_1 \\ -M^{-1}K & -M^{-1}C \end{bmatrix} \begin{bmatrix} \vec{X_1} \\ \vec{X_2} \end{bmatrix} \tag{5.9}$$

Or in other words:

$$\begin{bmatrix} \vec{x_1} \\ \vec{x_2} \\ . \\ - \\ \dot{\vec{x_1}} \\ \dot{\vec{x_2}} \\ . \end{bmatrix}' = \left[\begin{array}{ccc|ccc} 0 & 0 & . & 1 & 0 & . \\ 0 & 0 & . & 0 & 1 & . \\ . & . & . & . & . & . \\ \hline - & - & - & - & - & - \\ \hline \frac{-k_0-k_1}{m_1} & \frac{k_1}{m_1} & . & \frac{-c_0-c_1}{m_1} & 0 & . \\ \frac{k_1}{m_2} & \frac{-k_1-k_2}{m_2} & \frac{k_2}{m_2} & 0 & \frac{-c_1-c_2}{m_2} & . \\ . & . & . & . & . & . \end{array}\right] \begin{bmatrix} \vec{x_1} \\ \vec{x_2} \\ . \\ - \\ \dot{\vec{x_1}} \\ \dot{\vec{x_2}} \\ . \end{bmatrix} \tag{5.10}$$

5.2.1 1^{st} numerical simulation.

For this numerical simulation $m_1 = m_2 = ... = m_i = m = 1kg$, $c_1 = c_2 = ... = c_i = c = 3Ns/mm$, $k_1 = k_2 = ...k_i = k = 400000N/mm$.

The system was solved using a 4^{th} order Runge-Kutta numerical method with an initial condition:

$$\vec{X} = \begin{bmatrix} \vec{x_1} = 0 \\ \vec{x_2} = 0 \\ . \\ . \\ \dot{\vec{x_1}} = 0.1 \\ \dot{\vec{x_2}} = 0 \\ . \end{bmatrix}$$

which is equivalent to an impulse excitation of the first mass, for a time span of approximately 0.8192 seconds at a sample rate of 5000Hz, resulting in 4096 samples for each mass.

The oscillation of the simulated masses, as expected, are ruled by simillar laws. As such, we shall analyze only one of them, for example mass No.6. Its oscillation can be seen in *figure 19*.

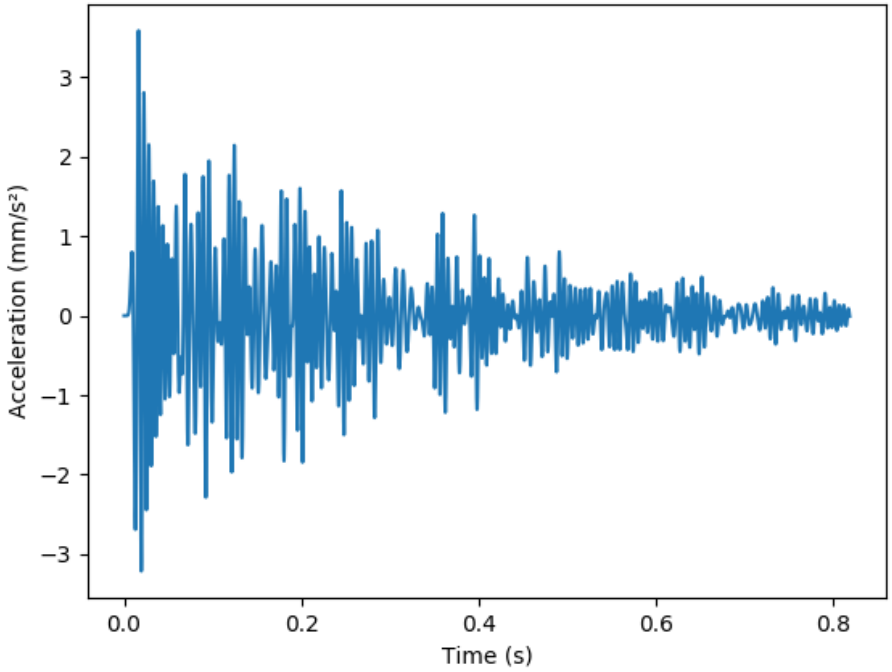

Figure 19: Raw oscillation of mass No.6 of the numerically simulated coupled linear dumped oscillators.

When examining the power spectrum of the signal, it is clear that the process has a bandwidth of about 200Hz, as shown in *figure 20*.

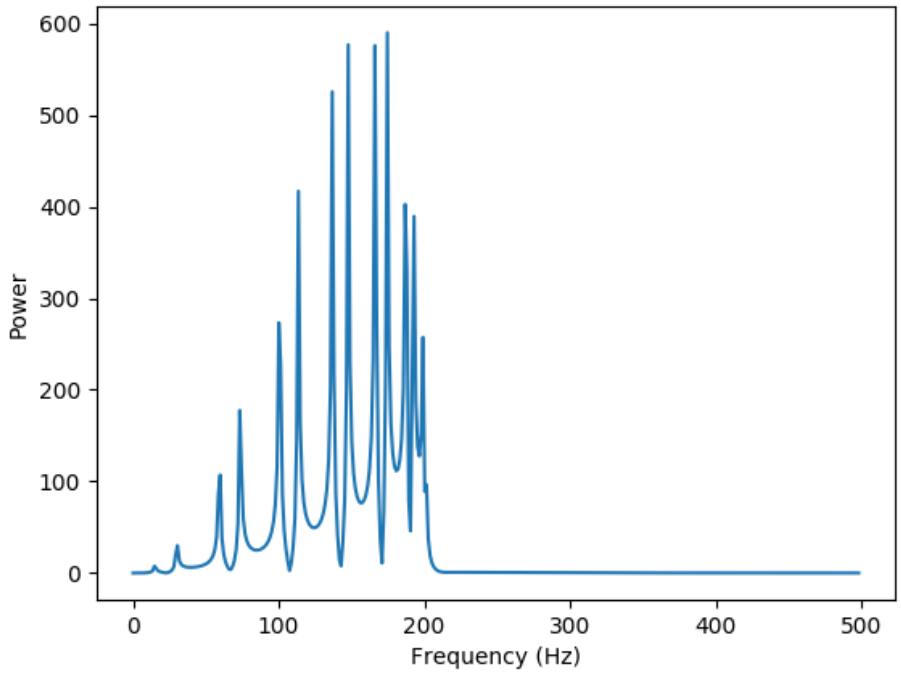

Figure 20: Power spectrum of the oscillation of mass No.6 of the numerically simulated coupled linear dumped oscillators.

Further more, since this is a linear oscillator, it is expected that the distribution of energy between frequencies and scales shall not vary over time, with the total energy decreasing exponentially. By examining the wavelet transform of the signal in *figure 21*, this exponential power decay can be seen.

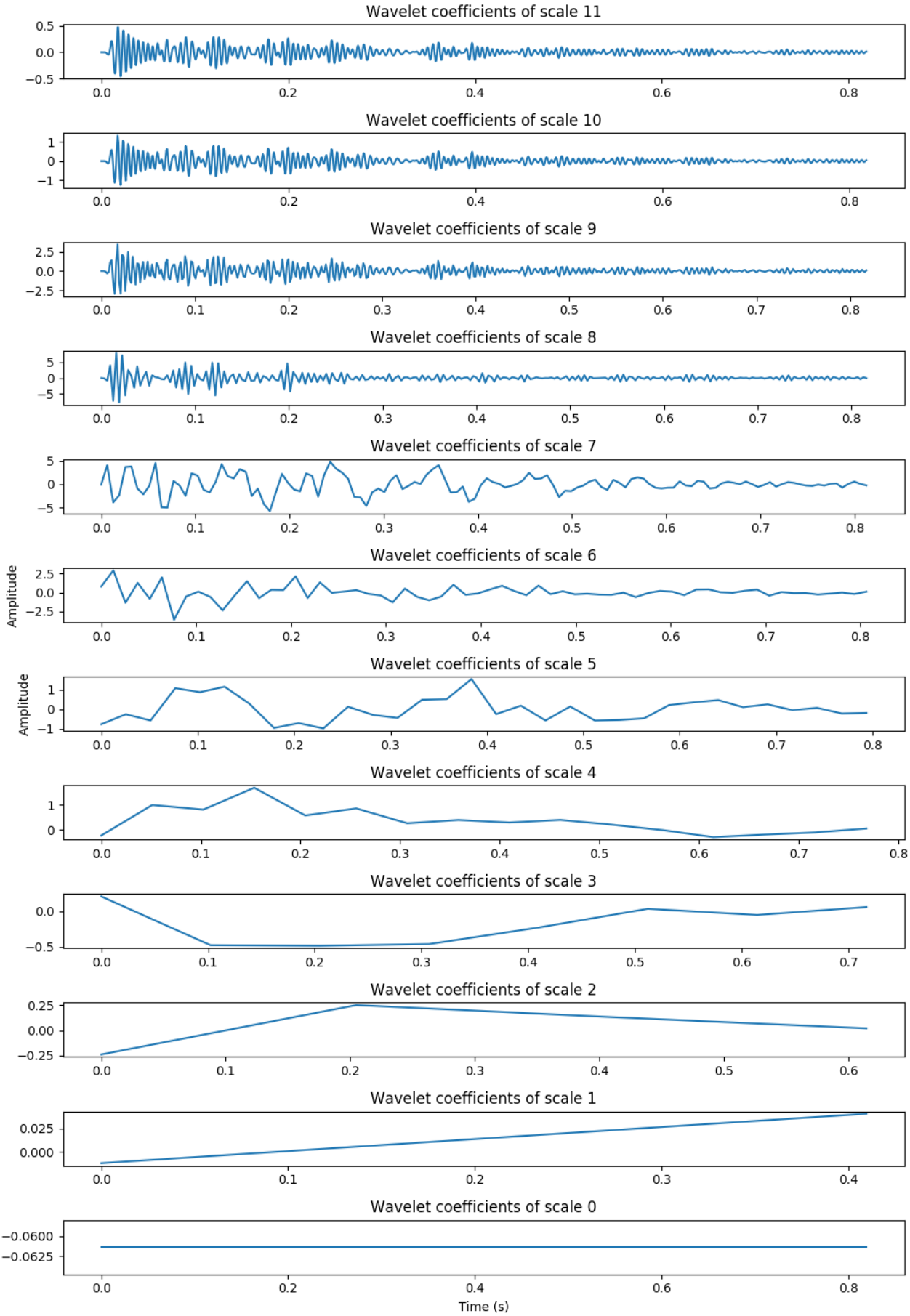

Figure 21: Wavelet decomposition of the oscillation of mass No.6 of the numerically simulated coupled linear dumped oscillators.

The Wavelet Entropy Time Series (*figure 23*), as expected, reveals that the energy distribution of the signal between different scales does not change over time. This is logical since the signal is sampled from an ideal linear oscillator whose analytical solution is by definition a superposition of exponentially decaying sine waves.

The oscillation of the wavelet entropy time series can be attributed once again to numerical calculations.

Furthermore, by examining the Spatial Wavelet Entropy from *equation 4.8* in (*figure 22*) for the series coupled oscillators we can see that the total Wavelet Entropy is approximately the same for all masses. The perturbation seen in the figure can once again be attributed to numerical calculations.

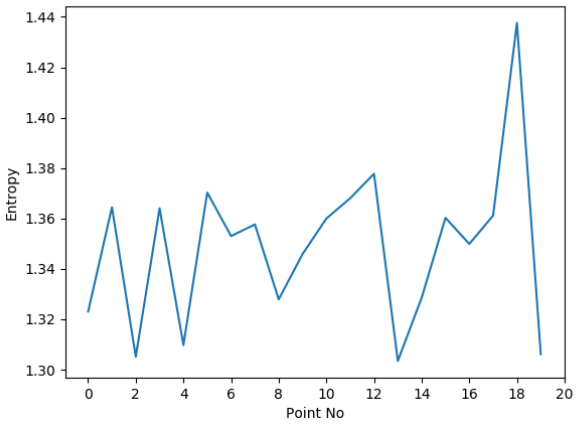

Figure 22: Spatial Wavelet Entropy of the ensemble of signals for this system.

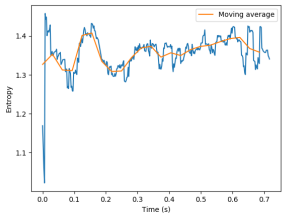

(a) Mass No. 0

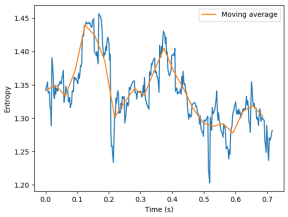

(a) Mass No. 5

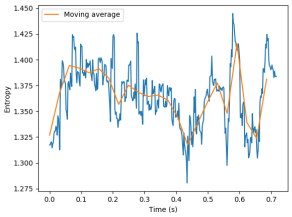

(f) Mass No. 10

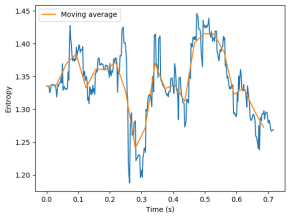

(k) Mass No. 15

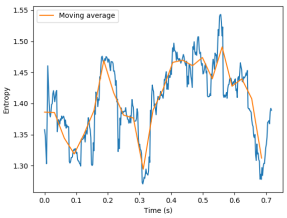

(b) Mass No. 1

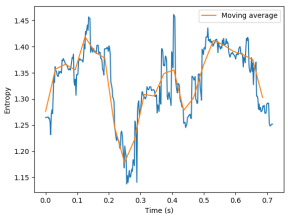

(b) Mass No. 6

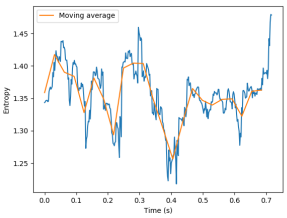

(g) Mass No. 11

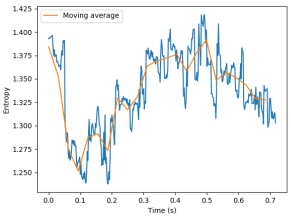

(l) Mass No. 16

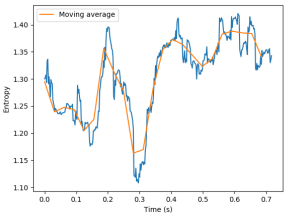

(c) Mass No. 2

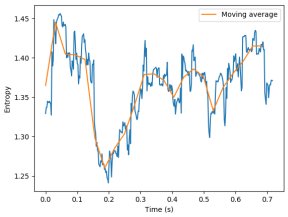

(c) Mass No. 7

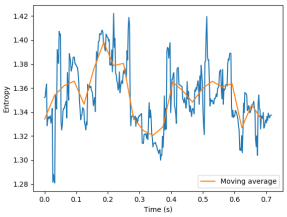

(h) Mass No. 12

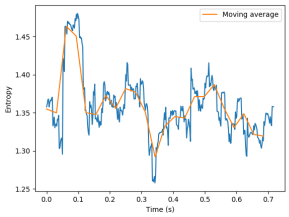

(m) Mass No. 17

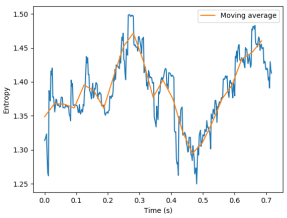

(d) Mass No. 3

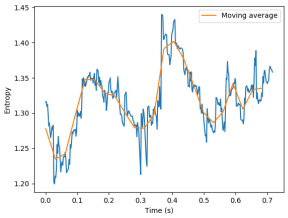

(d) Mass No. 8

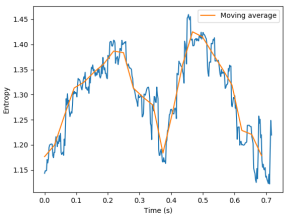

(i) Mass No. 13

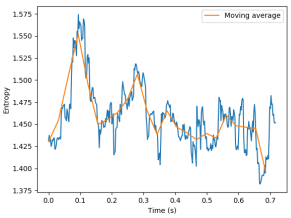

(n) Mass No. 18

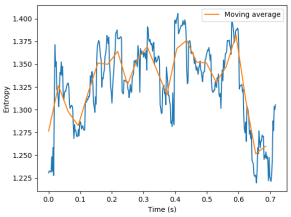

(e) Mass No. 4

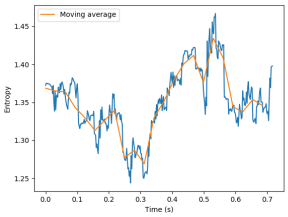

(e) Mass No. 9

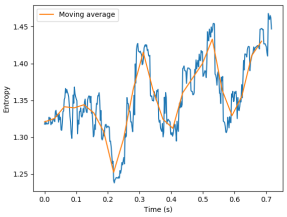

(j) Mass No. 14

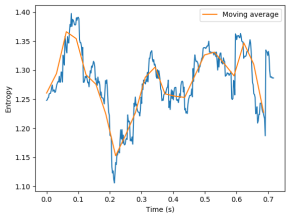

(o) Mass No. 19

Figure 23

5.2.2 2^{nd} numerical simulation.

For this numerical simulation $m_1 = m_2 = ... = m_i = m = 1kg$, $c_1 = c_2 = ... = c_i = c = 3Ns/mm$, $k_1 = k_2 = ...k_i = k = 400000N/mm$, except for $k_5 = 360000N/mm$ and

$c_5 = 2.7Ns/mm.$

The point of this second simulation is to investigate whether Wavelet Entropy Time Series can identify the mass with different properties than the rest of the masses.

The system was also solved using a 4^{th} order Runge-Kutta numerical method with an initial condition:

$$\vec{X} = \begin{bmatrix} \vec{x_1} = 0 \\ \vec{x_2} = 0 \\ . \\ . \\ \dot{\vec{x_1}} = 0.1 \\ \dot{\vec{x_2}} = 0 \\ . \end{bmatrix}$$

which is equivalent to an impulse excitation of the first mass, for a time span of approximately 0.8192 seconds at a sample rate of 5000Hz, resulting in 4096 samples for each mass.

Since the oscillation of the simulated masses are ruled by similar laws, as in the previous simulation.We shall once again analyze only one of them, mass No.6. Its oscillation can be seen in *figure 24*.

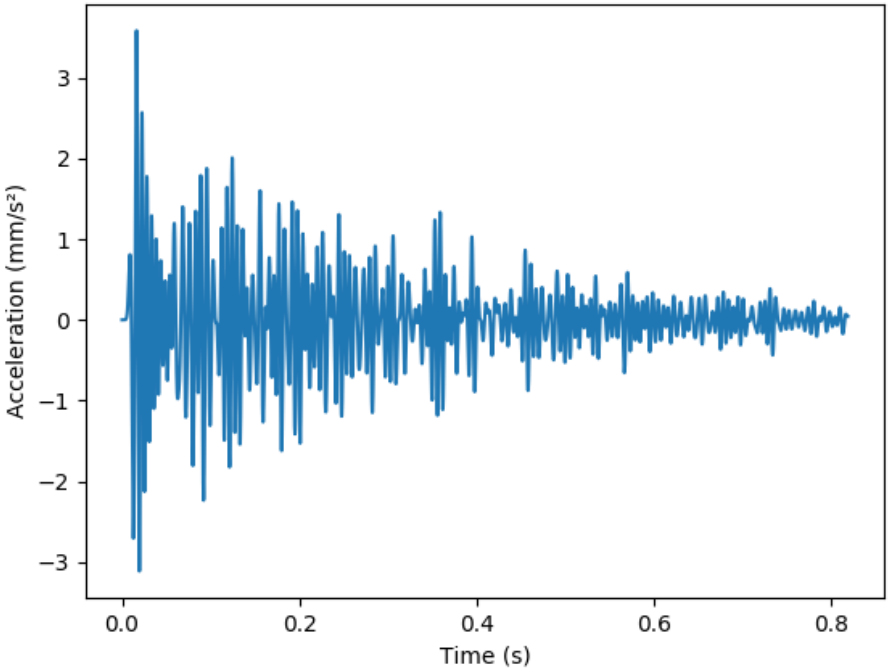

Figure 24: Raw oscillation of mass No.6 of the numerically simulated coupled linear dumped oscillators.

When examining the power spectrum of the signal, it is clear that the process has a bandwidth of about 200Hz, as shown in *figure 25*.

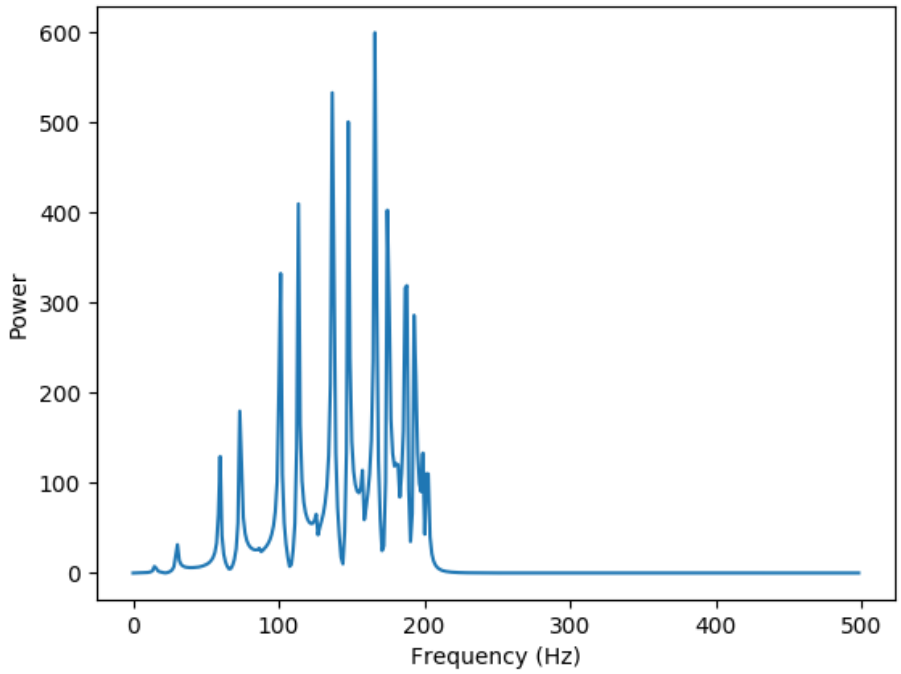

Figure 25: Power spectrum of the oscillation of mass No.6 of the numerically simulated coupled linear dumped oscillators.

Once again, the distribution of energy between frequencies and scales does not vary over time, with the total energy decreasing exponentially. By examining the wavelet transform of the signal in *figure 26*, the exponential power decay can be seen, but it is not clear whether or not the distribution of power experiences dispersion from this figure alone..

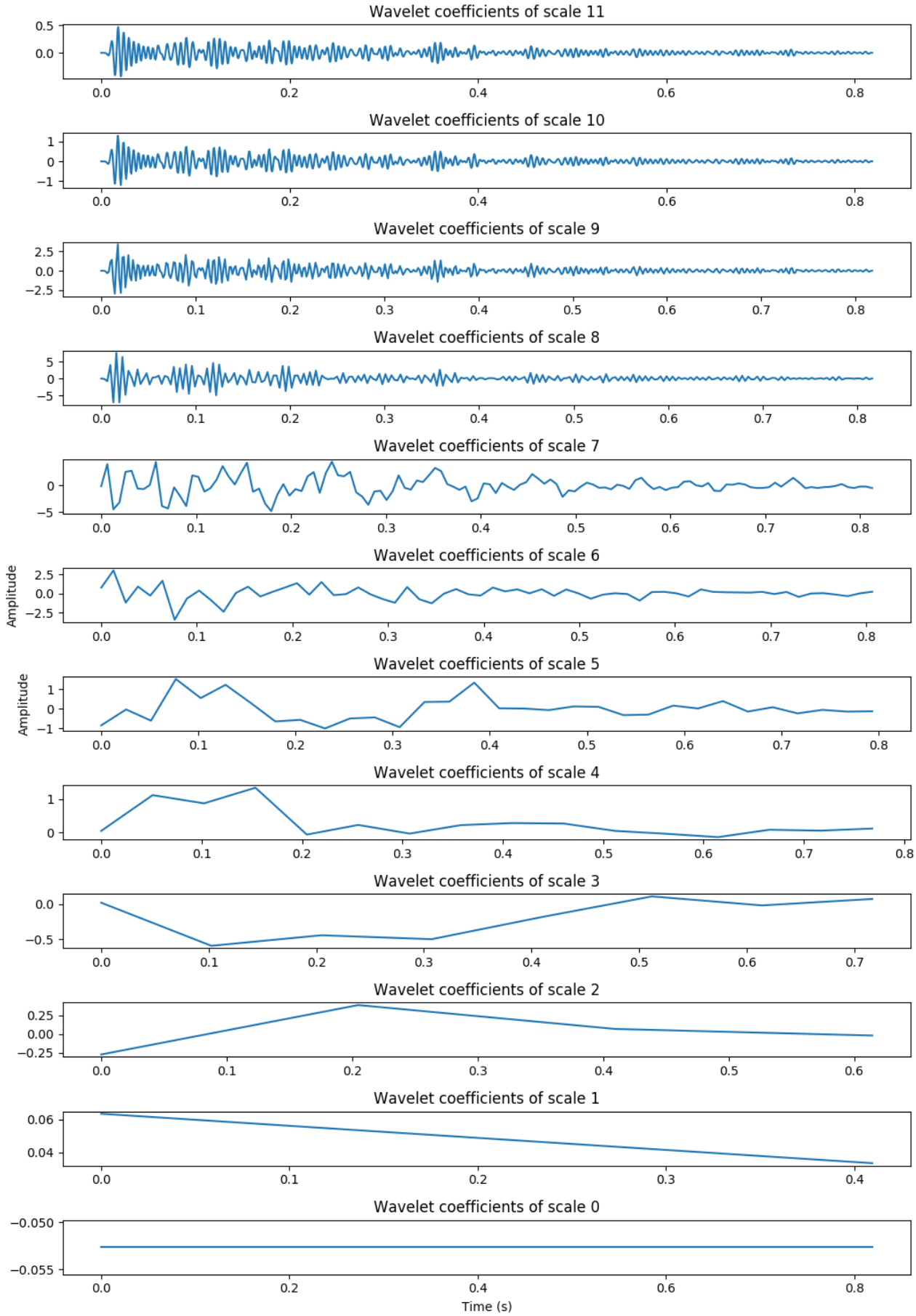

Figure 26: Wavelet decomposition of the oscillation of mass No.6 of the numerically simulated coupled linear dumped oscillators.

Furthermore, by examining the Spatial Wavelet Entropy from *equation 4.8* in (*figure 27*) for the series coupled oscillators we can see that the total Wavelet Entropy is approximately the same for all masses. The perturbation seen in the figure can once again be attributed to numerical calculations.

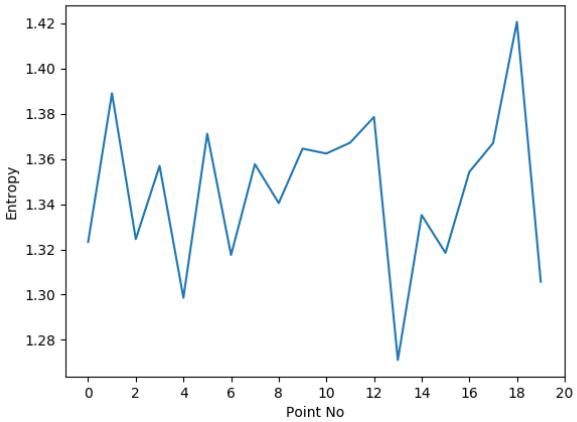

Figure 27: Spatial Wavelet Entropy of the ensemble of signals for this system.

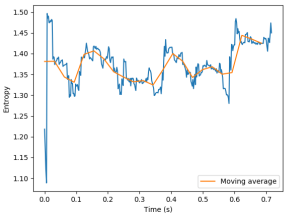

(a) Mass No. 0

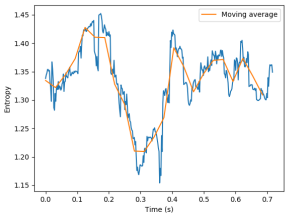

(a) Mass No. 5

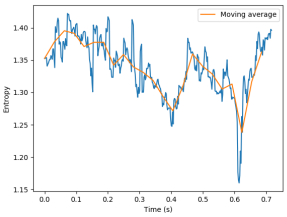

(f) Mass No. 10

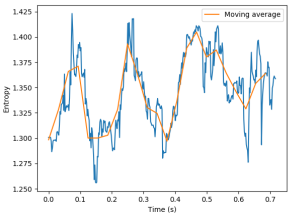

(k) Mass No. 15

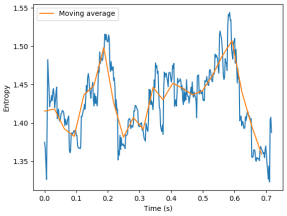

(b) Mass No. 1

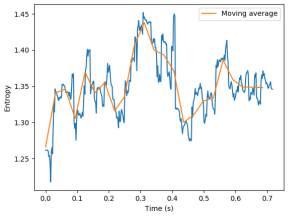

(b) Mass No. 6

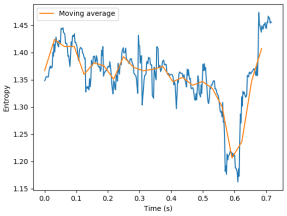

(g) Mass No. 11

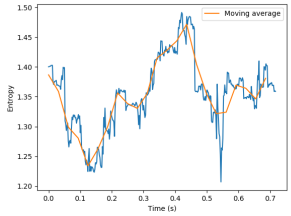

(l) Mass No. 16

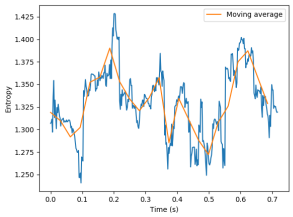

(c) Mass No. 2

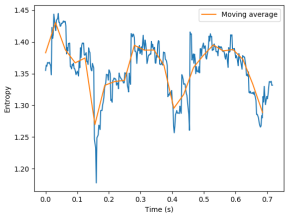

(c) Mass No. 7

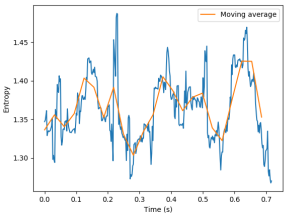

(h) Mass No. 12

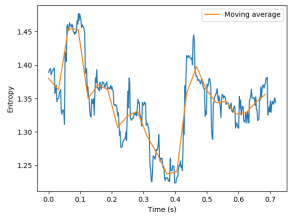

(m) Mass No. 17

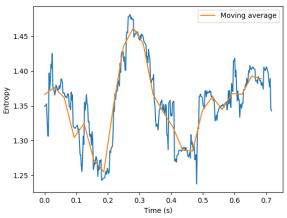

(d) Mass No. 3

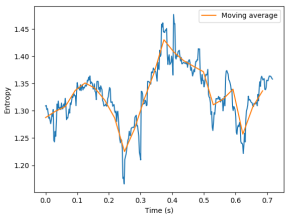

(d) Mass No. 8

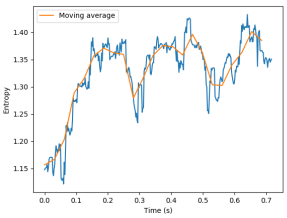

(i) Mass No. 13

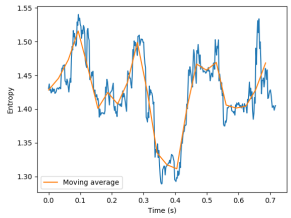

(n) Mass No. 18

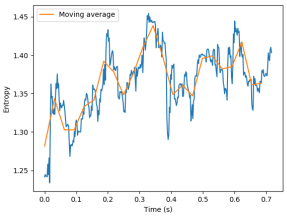

(e) Mass No. 4

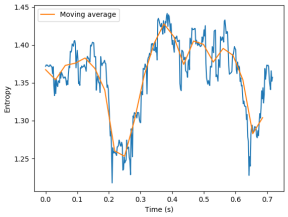

(e) Mass No. 9

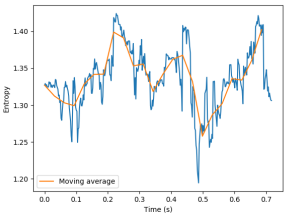

(j) Mass No. 14

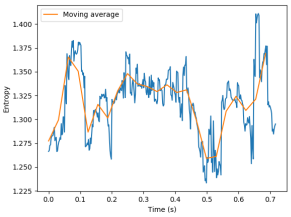

(o) Mass No. 19

Figure 28:

It is clear that Wavelet Entropy Time Series (*figure 28*) cannot identify a difference in a series of coupled oscillators, which is expected since the distribution of energy between frequencies and consecutively between different wavelet energy levels does not vary over time. For all masses, a small perturbation around a value can be observed. This small perturbation can be attributed to the numerical computations and can be seen in all calculations. Furthermore, the square nature of the "Haar" wavelet basis can also contribute in that oscillation. Smoother wavelet basis could possibly result in a decrease in the magnitude of the oscillation. The fact that the mean entropy value of all the above figures remains approximately constant is therefore an indication that the algorithm developed provides the expected outcome and functions properly.

6 Spatial Localization of Air Inclusions

The concept behind wavelet entropy analysis for damage identification derives from the idea that any wave when interacting with a discontinuity (e.g. crack, or in this case an air inclusion) will get diffracted, causing the vibration to become more complicated. Consequently, if the excitation point is close to any geometric abnormality, then the distribution of power between different scales over time will not be constant and, as a result, the disarray of the transformed signal will follow a seemingly unpredictable pattern. Wavelets are an excellent tool in analyzing transient events, as they exhibit the ability to isolate events in the time index. Therefore, the wavelet transform in conjunction with Shannon's entropy is able to distinguish trends in a system's dynamics.

6.1 Experimental arrangement

A carbon fiber T-beam of length L=1.5m with a pin support in both ends was sectioned every L/51 as designated by 50 stickers (positions 0-49), enumerated from right to left. Accelerometers were then mounted at positions 5 (accelerometer 3), 25 (accelerometer 2), 44 (accelerometer 1), as shown in figure 29. A tap-test was then carried out at each of the 50 locations designated by the stickers, using a tap hammer. The accelerometers saved the measured data as a column in a txt format file with a sample rate of 25kHz and a resolution of 16 bits. The experiment was then repeated twice. It has been proven [Georgiou, 2019] that for this particular database, there is not a spatial correlation between the accelerometer's position and observed statistics, meaning that it is unnecessary to move the accelerometers for each tap-test.

The beam was manufactured in such a way that it contains air inclusions, compromising its structural integrity, with the experiment trying to localize these inclusions.

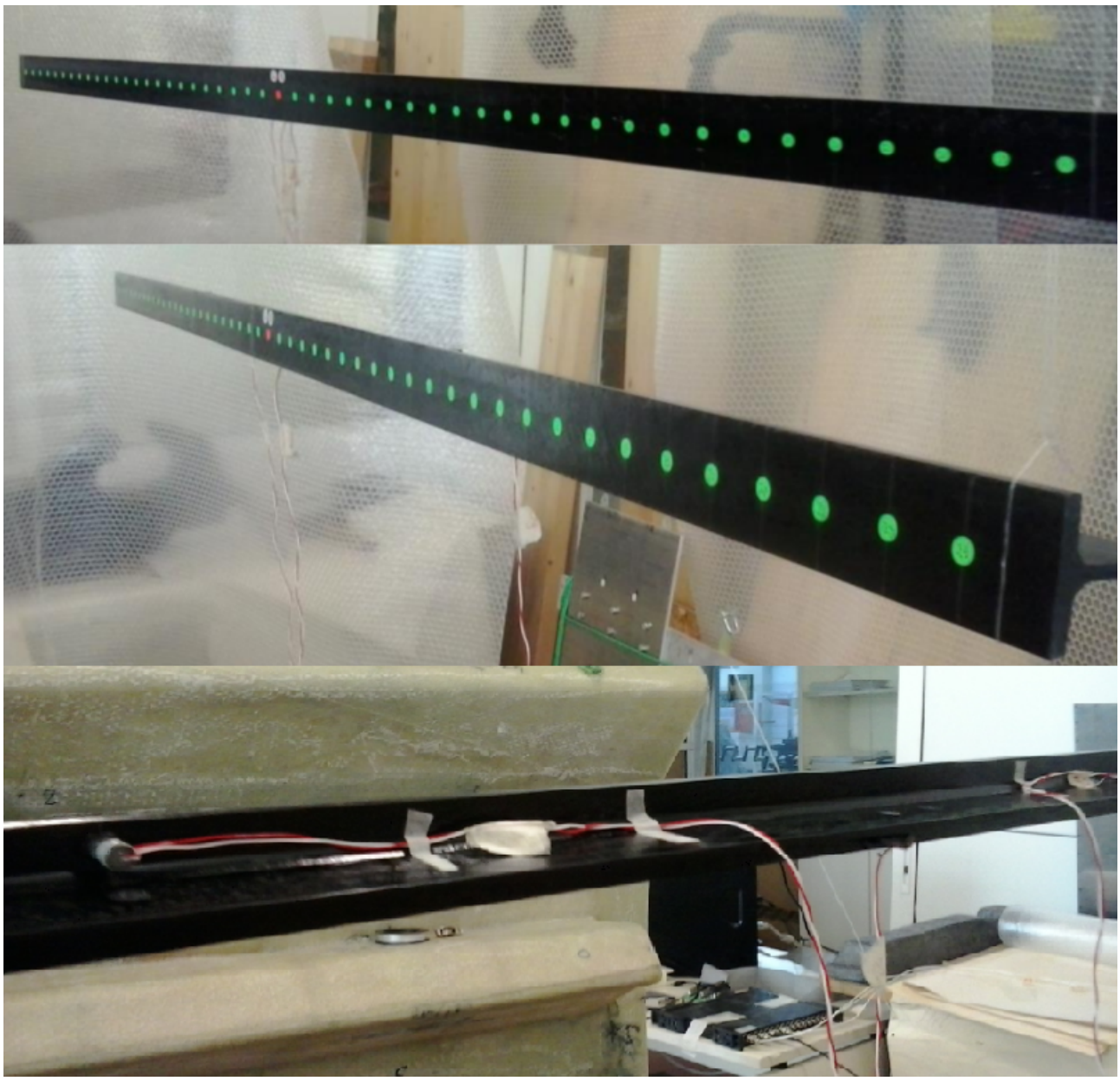

Figure 29: Experimental setup.

6.2 Results

6.2.1 Visual interpretation

An initial visual inspection of the results reveals a deconstructive interference in the data received by the accelerometer positioned at L/2, as shown by *figure 31*.

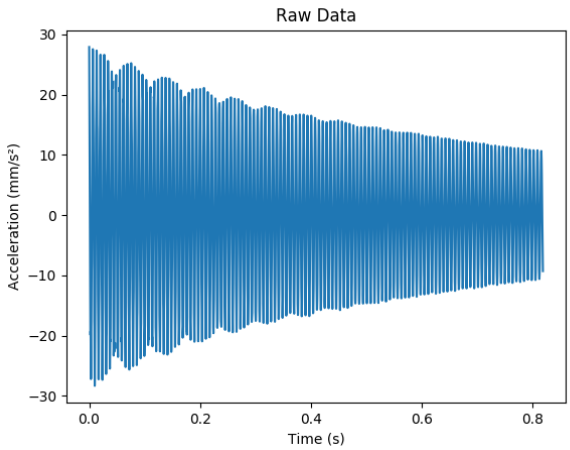

Figure 30: Vibration of the carbon fiber rod as sampled by the accelerometer No.2 when exciting the rod at point 0 during the 1^{st} test.

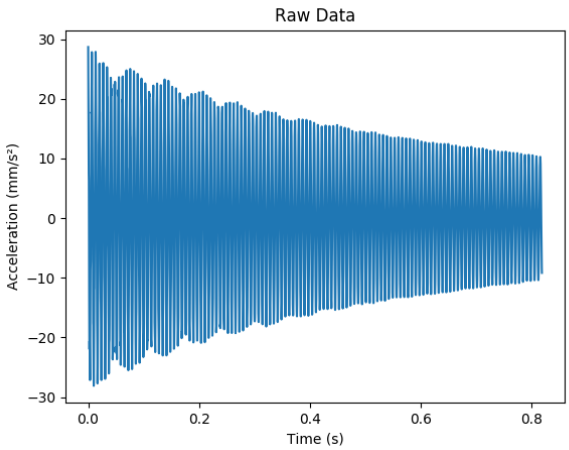

Figure 31: Vibration of the carbon fiber rod as sampled by the accelerometer No.2 when exciting the rod at point 0 during the 2^{nd} test.

A clear interference with a high amplitude of low-frequency can be seen in every measurement in both tests. This has most likely engendered from a defect in the mounting of the accelerometer, wherefore the data acquired from set accelerometer were discarded as deemed untrustworthy.

From the remainder of the data, as expected, a visual inspection proves to ineffectual at providing any valuable results.

6.2.2 Comparison between Fourier and Wavelet Transform.

A disadvantage of the Fourier analysis is that frequency information can be extracted for the complete duration of a signal $f(t)$. Since the integral in the Fourier Transform equation extends over all time, from $-\infty$ to $+\infty$, the information it provides arises from the average over the whole length of the signal. Any local phenomenons in the lifetime of $f(t)$, although they contribute to the calculation of the Fourier transform $F(\omega)$, their location in the time axis cannot be identified. As aforementioned however, wavelet analysis breaks down the signal to constituent parts and is allowing for resolution both in scale and in time.

This is evident if we examine both the wavelet and Fourier decomposition of one of the acquired signals.

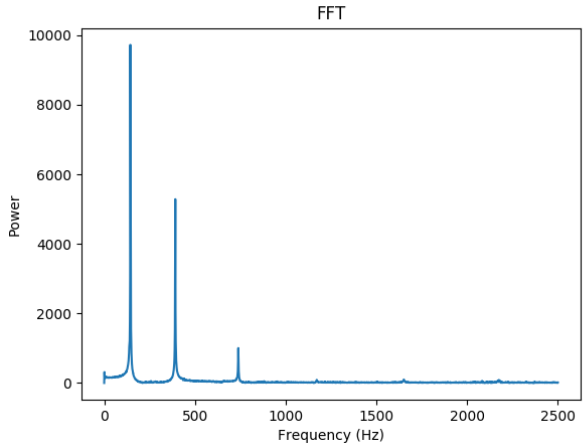

Figure 32: Power spectrum of vibration of the carbon fiber rod as sampled by the accelerometer No.1 when exciting the rod at point 0 during the 1^{st} test (30).

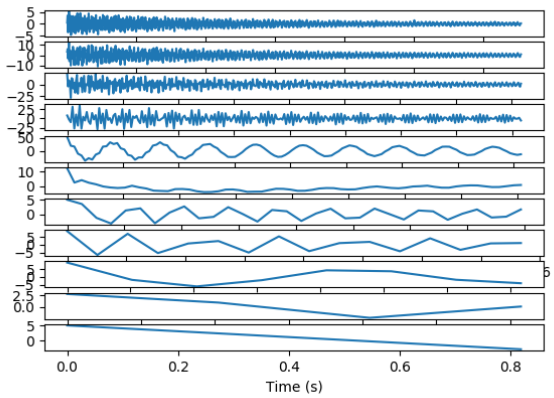

Figure 33: Discrete Haar wavelet transform of vibration of the carbon fiber rod as sampled by the accelerometer No.1 when exciting the rod at point 0 during the 1^{st} test (30).

In *figures 32, 33* we can see that while the Fast Fourier transform provides no resolution about the locality in the time index of events, the wavelet expansion gives reliable resolution in the time index. The next limitation is decoding that information in a helpful way to assist in structural health monitoring. The tool proposed for this assistance is Shannon's Entropy.

6.2.3 Wavelet Entropy Time Series analysis

Since a tap test is an impact test, the acceleration response is a free-decaying process. Therefore, for a healthy part of the structure it is expected that its entropy will also follow a seemingly exponentially decaying path, meaning the bandwidth of the signal will tend to narrow over time [Sorokin, 2002]. This is the case for the vast majority of points where the entropy from both accelerometers 1,3 evolves similar to figures 34, 35.

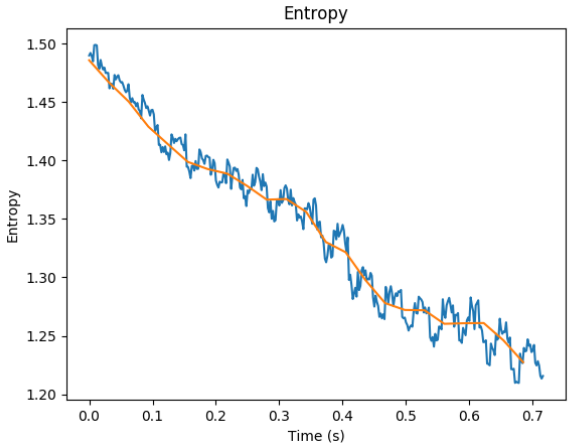

(a) Accelerometer 1

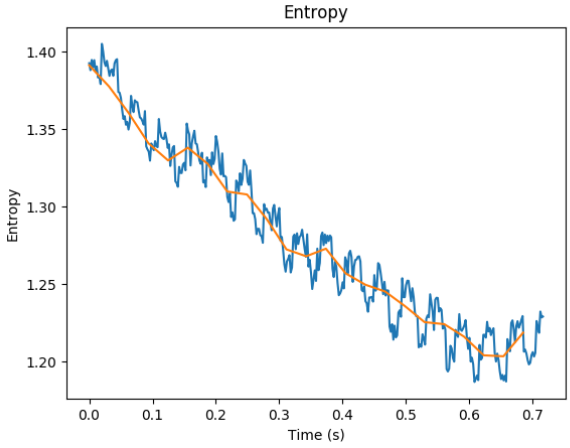

(b) Accelerometer 3

Figure 34: Wavelet Entropy Time series of vibration of the carbon fiber rod as sampled by the accelerometers No.1, 3 when exciting the rod at point 0 during the 1^{st} test.

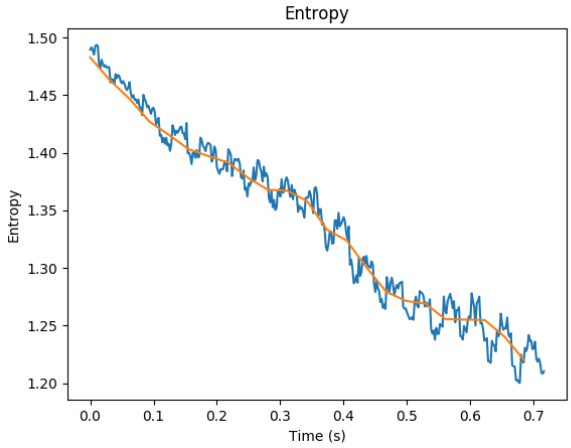

(a) Accelerometer 1

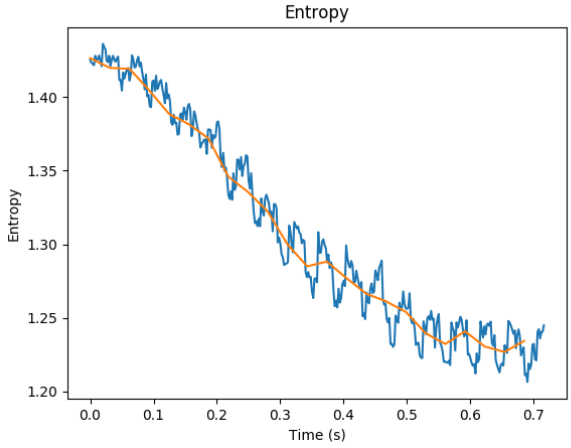

(b) Accelerometer 3

Figure 35: Wavelet Entropy Time series of vibration of the carbon fiber rod as sampled by the accelerometer No.1, 3 when exciting the rod at point 0 during the 2^{nd} test.

There are four areas however where the entropy evolution deviates from that aforementioned decaying behavior. These are areas around points 5, 44 and the regions 9-11 and 37-39. A keen reader would remember that the accelerometers were mounted on points 5, 25, 44; it is therefore expected that the received signal will differ in the neighborhood of those areas.

6.2.3.1 Neighbouring the acceleromers.

When the tap test occurs nearby an accelerometer, it has been observed that the Wavelet Entropy Time Series of the acquired signal from set accelerometer does provide definitive results.

Notwithstanding, the measurements from rest of the accelerometers are reliable; this can also be seen in figures 36, 37. On that basis, point 25 did not show any abnormal behavior since the data from the 2^{nd} accelerometer have already been discarded.

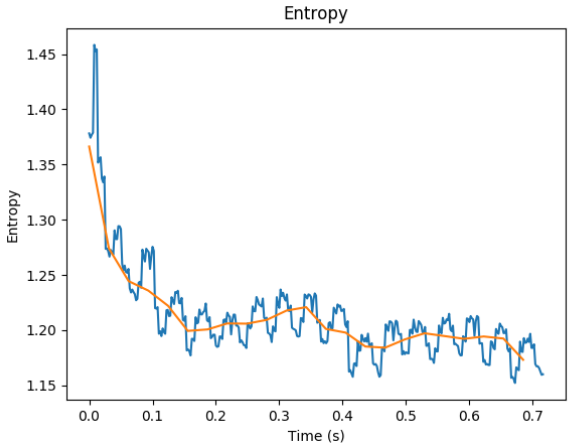

(a) Accelerometer 1

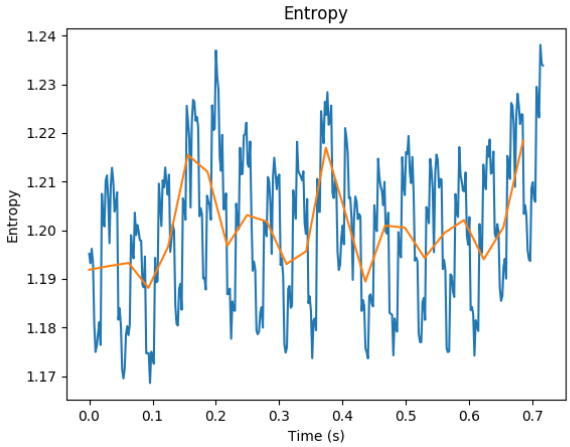

(b) Accelerometer 3

Figure 36: Wavelet Entropy Time series of vibration of the carbon fiber rod as sampled by the accelerometer No.1, 3 when exciting the rod at point 5 during the 1^{st} test. Figures a, b show that when exciting at the location of the No.3 accelerometer, that accelerometer does provide reliable readings, while the other accelerometer does.

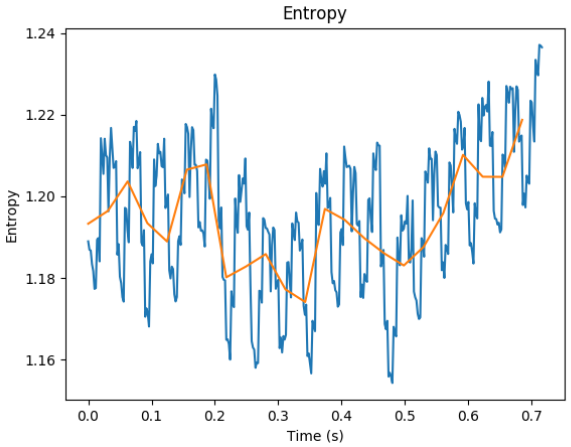

(a) Accelerometer 1

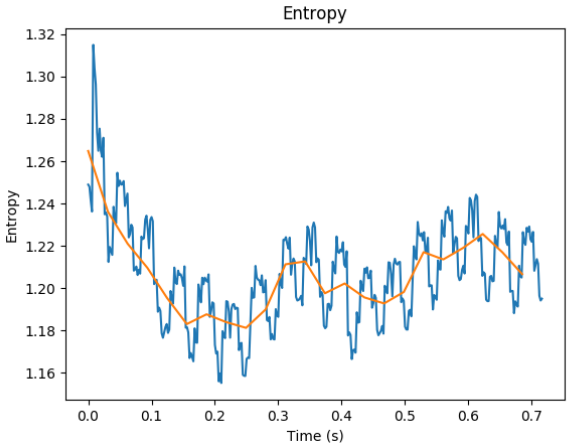

(b) Accelerometer 3

Figure 37: Wavelet Entropy Time series of vibration of the carbon fiber rod as sampled by the accelerometer No.1, 3 when exciting the rod at point 44 during the 1^{st} test. Figures a, b show that when exciting at the location of the No.1 accelerometer, that accelerometer does provide reliable readings, while the other accelerometer does.

The areas around points 5,44 (points 4-6 and 43-45) also exhibit similar behavior to figures 36, 37.

6.2.3.2 Points 9 - 11

Both accelerometers and both executions of the experiment displayed similar behavior in the area of points 9, 10, 11 with the wavelet entropy increasing over time instead.

At point 8 the entropy follows an exponentially decaying path as expected, shown in figures 38, 39.

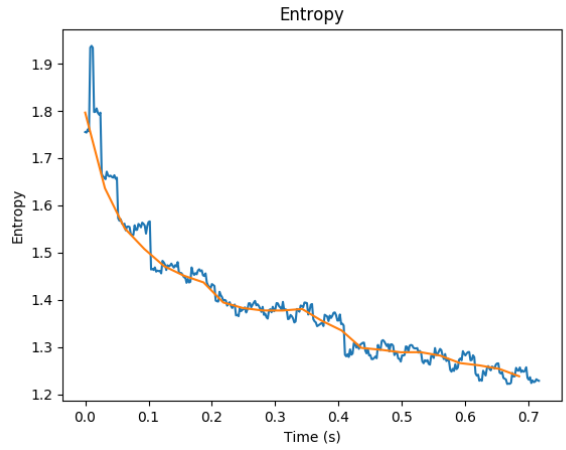

(a) Accelerometer 1

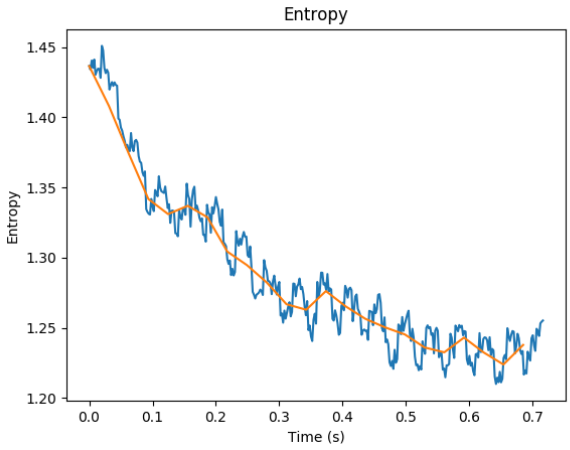

(b) Accelerometer 3

Figure 38: Wavelet Entropy Time series of vibration of the carbon fiber rod as sampled by the accelerometer No.1, 3 when exciting the rod at point 8 during the 1^{st} test.

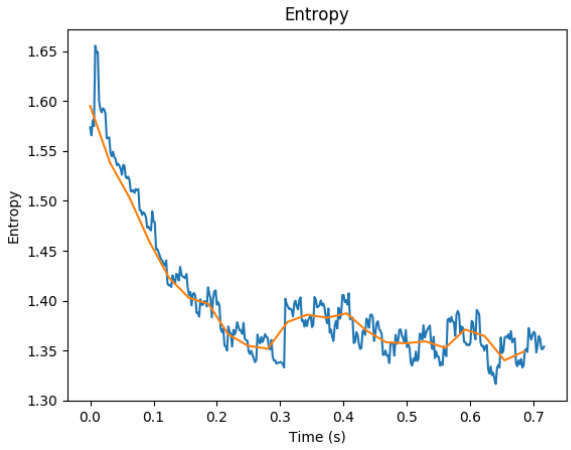

(a) Accelerometer 1

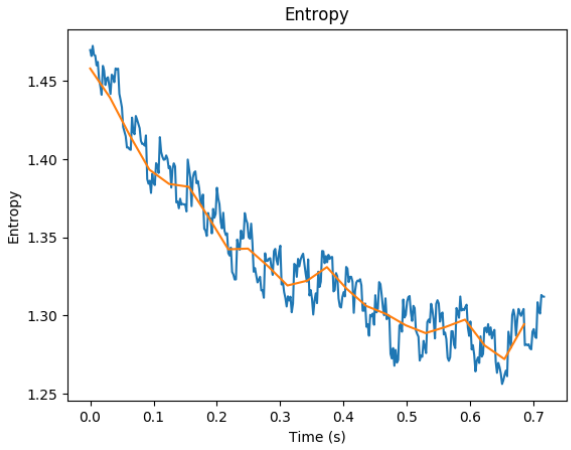

(b) Accelerometer 3

Figure 39: Wavelet Entropy Time series of vibration of the carbon fiber rod as sampled by the accelerometer No.1, 3 when exciting the rod at point 44 during the 2^{nd} test.

The entropy evolution trend for points is shown in figures 40, 41 for point 9; figures 42, 43 for point 10; figures 44, 45 for point 11.

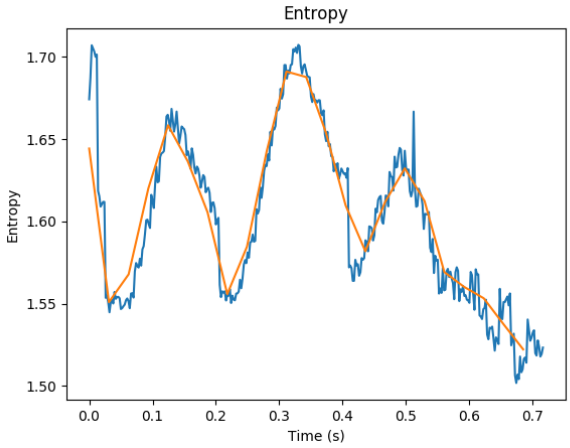

(a) Accelerometer 1

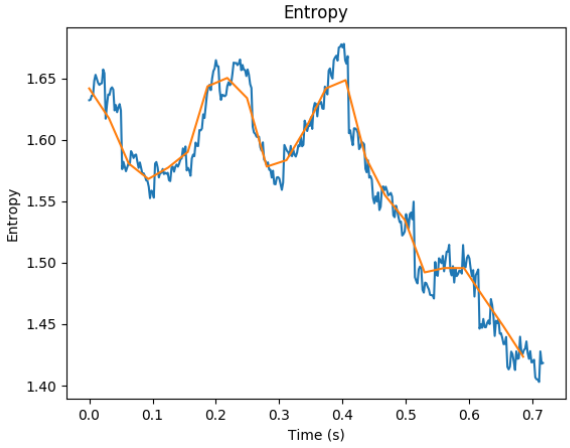

(b) Accelerometer 3

Figure 40: Wavelet Entropy Time series of vibration of the carbon fiber rod as sampled by the accelerometer No.1, 3 when exciting the rod at point 9 during the 1^{st} test.

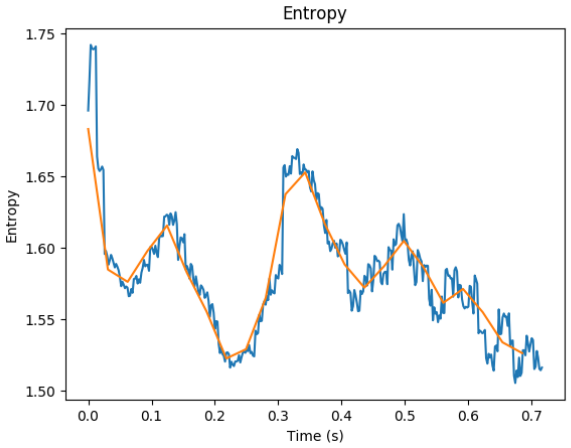

(a) Accelerometer 1

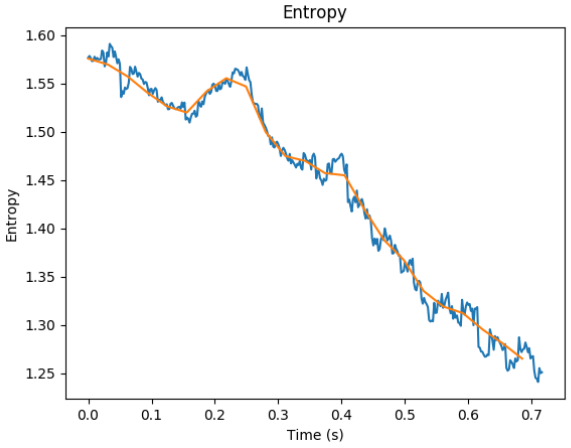

(b) Accelerometer 3

Figure 41: Wavelet Entropy Time series of vibration of the carbon fiber rod as sampled by the accelerometer No.1, 3 when exciting the rod at point 9 during the 2^{nd} test.

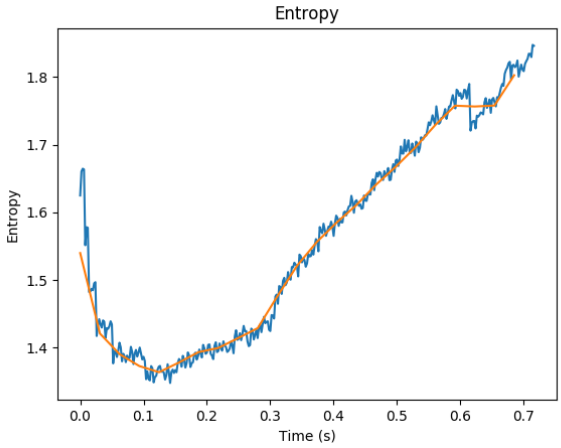

(a) Accelerometer 1

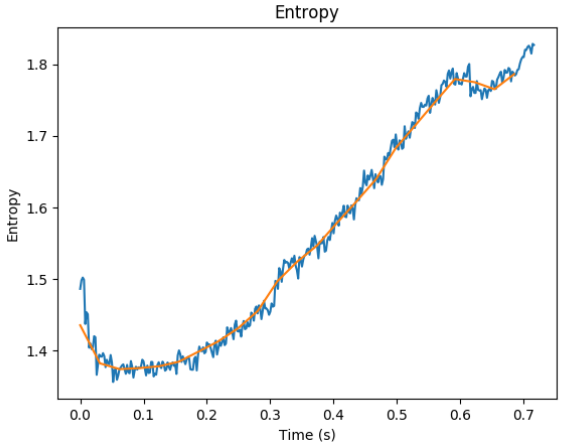

(b) Accelerometer 3

Figure 42: Wavelet Entropy Time series of vibration of the carbon fiber rod as sampled by the accelerometer No.1, 3 when exciting the rod at point 10 during the 1^{st} test.

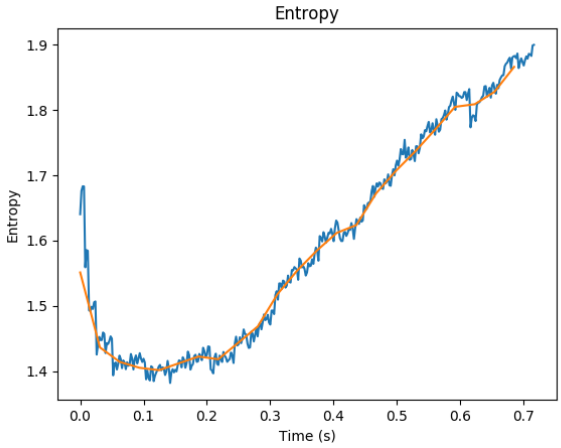

(a) Accelerometer 1

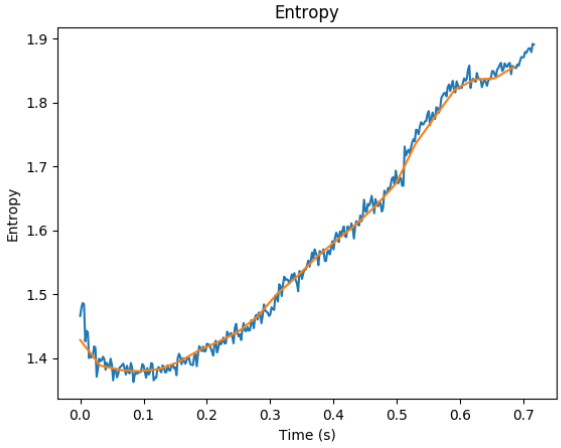

(b) Accelerometer 3

Figure 43: Wavelet Entropy Time series of vibration of the carbon fiber rod as sampled by the accelerometer No.1, 3 when exciting the rod at point 10 during the 2^{nd} test.

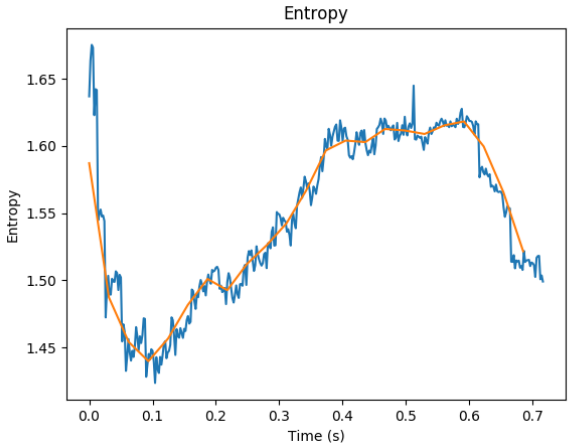

(a) Accelerometer 1

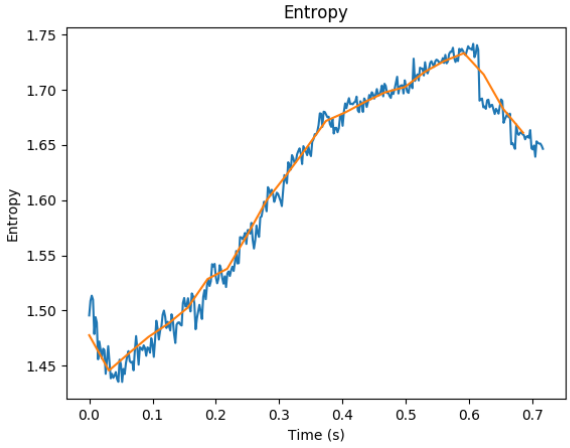

(b) Accelerometer 3

Figure 44: Wavelet Entropy Time series of vibration of the carbon fiber rod as sampled by the accelerometer No.1, 3 when exciting the rod at point 11 during the 1^{st} test.

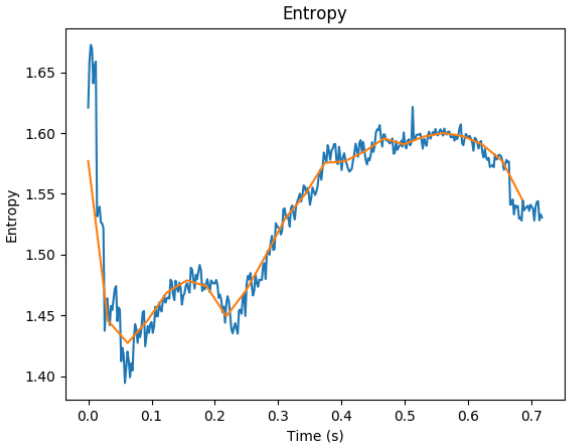

(a) Accelerometer 1

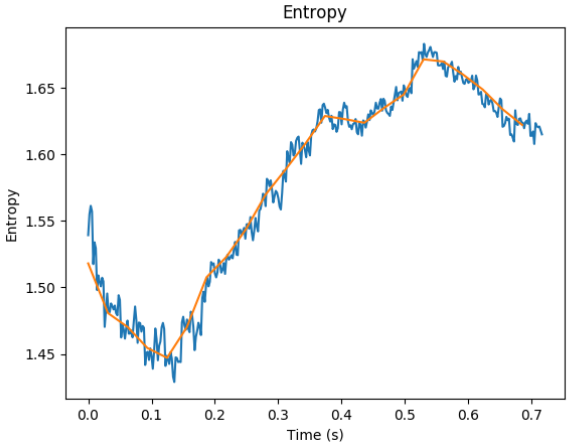

(b) Accelerometer 3

Figure 45: Wavelet Entropy Time series of vibration of the carbon fiber rod as sampled by the accelerometer No.1, 3 when exciting the rod at point 11 during the 2^{nd} test.

Eventually, in point 12 the entropy evolution gradually gets restored to an exponentially decaying path.

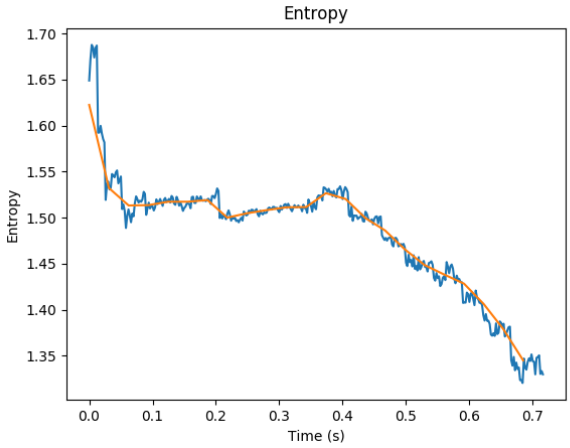

(a) Accelerometer 1

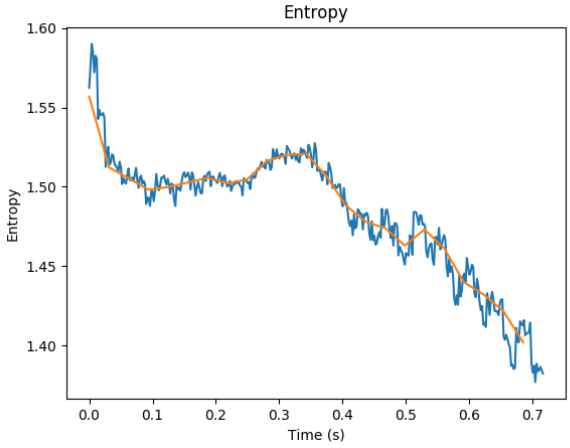

(b) Accelerometer 3

Figure 46: Wavelet Entropy Time series of vibration of the carbon fiber rod as sampled by the accelerometer No.1, 3 when exciting the rod at point 12 during the 1^{st} test.

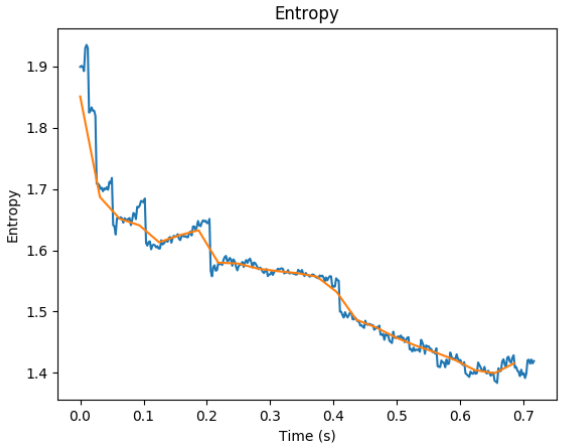

(a) Accelerometer 1

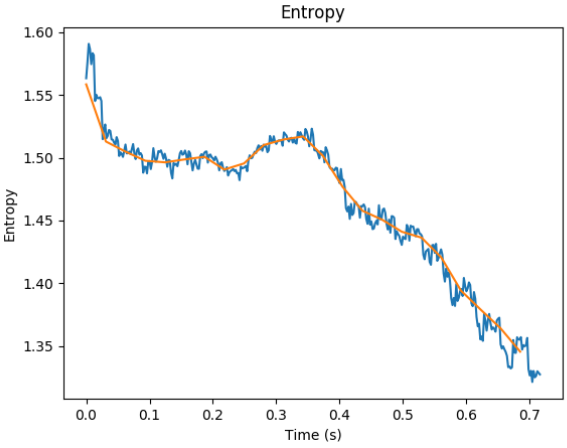

(b) Accelerometer 3

Figure 47: Wavelet Entropy Time series of vibration of the carbon fiber rod as sampled by the accelerometer No.1, 3 when exciting the rod at point 12 during the 2^{nd} test.

6.2.3.3 Points 37 - 39

Both accelerometers and both executions of the experiment displayed similar behavior in the area of points 9, 10, 11 with the wavelet entropy increasing over time instead.

At point 8 the entropy follows an exponentially decaying path, as expected, as shown in figures 48, 49.

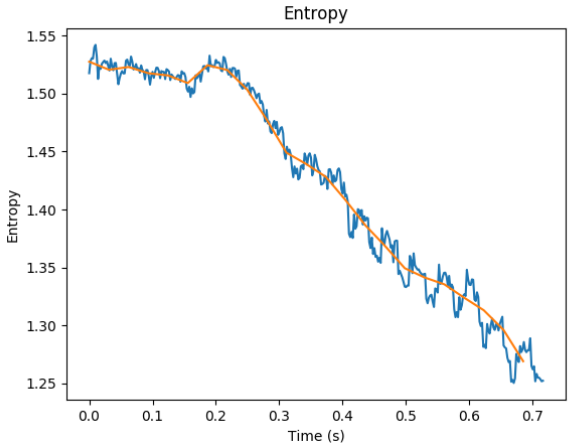

(a) Accelerometer 1

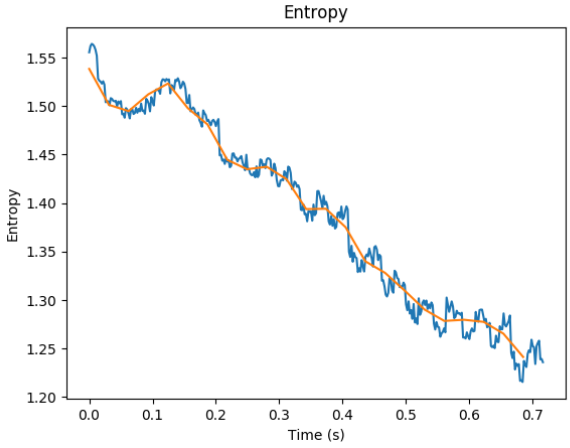

(b) Accelerometer 3

Figure 48: Wavelet Entropy Time series of vibration of the carbon fiber rod as sampled by the accelerometer No.1, 3 when exciting the rod at point 36 during the 1^{st} test.

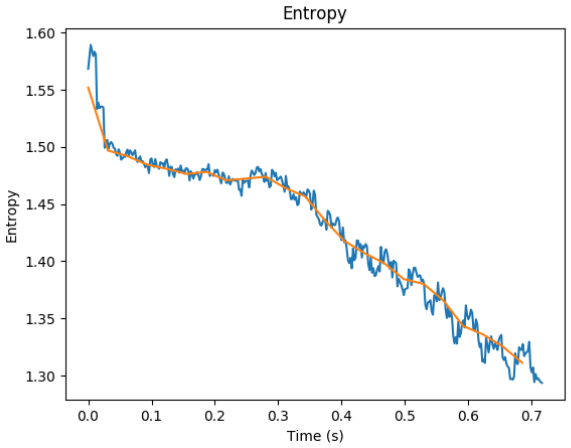

(a) Accelerometer 1

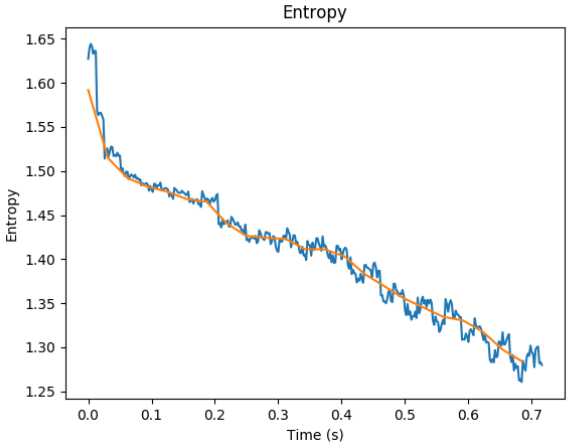

(b) Accelerometer 3

Figure 49: Wavelet Entropy Time series of vibration of the carbon fiber rod as sampled by the accelerometer No.1, 3 when exciting the rod at point 36 during the 2^{nd} test.

The entropy evolution trend for points is shown in figures 50, 51 for point 9; figures 52, 53 for point 10; figures 54, 55 for point 11.

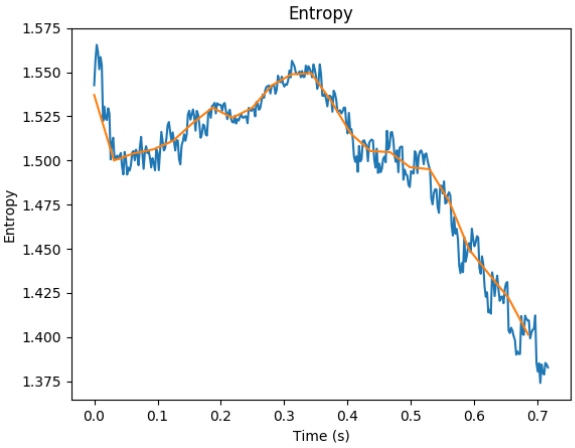

(a) Accelerometer 1

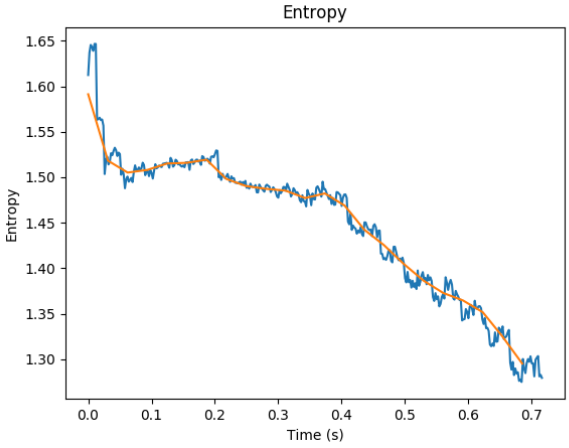

(b) Accelerometer 3

Figure 50: Wavelet Entropy Time series of vibration of the carbon fiber rod as sampled by the accelerometer No.1, 3 when exciting the rod at point 37 during the 1^{st} test.

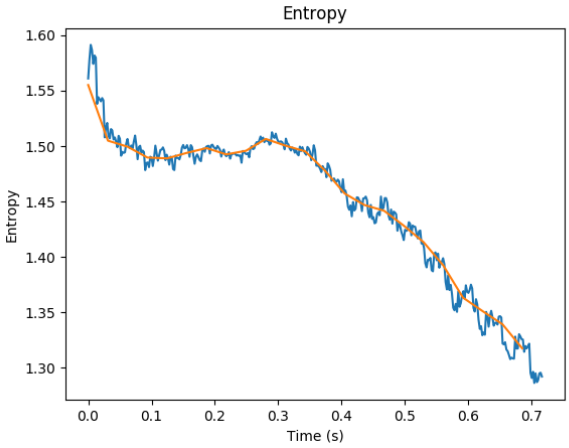

(a) Accelerometer 1

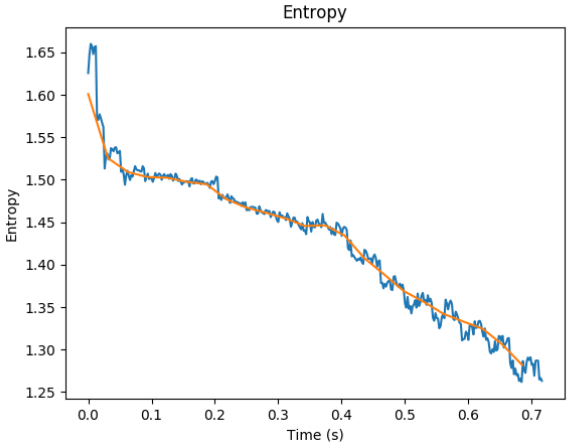

(b) Accelerometer 3

Figure 51: Wavelet Entropy Time series of vibration of the carbon fiber rod as sampled by the accelerometer No.1, 3 when exciting the rod at point 37 during the 2^{nd} test.

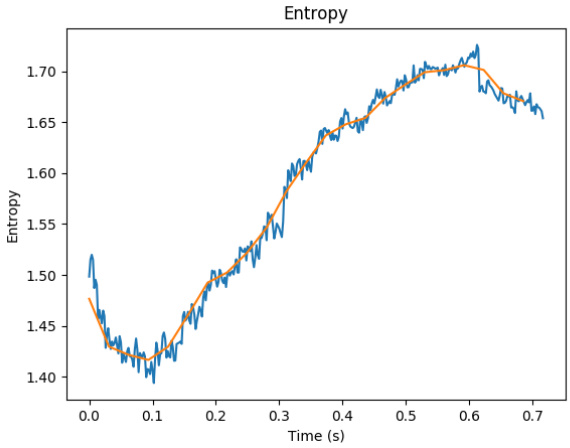

(a) Accelerometer 1

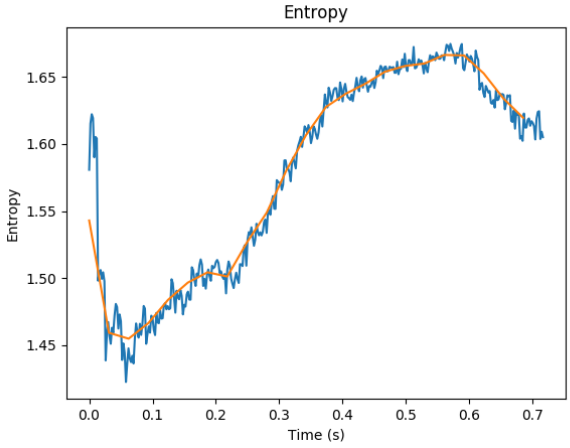

(b) Accelerometer 3

Figure 52: Wavelet Entropy Time series of vibration of the carbon fiber rod as sampled by the accelerometer No.1, 3 when exciting the rod at point 38 during the 1^{st} test.

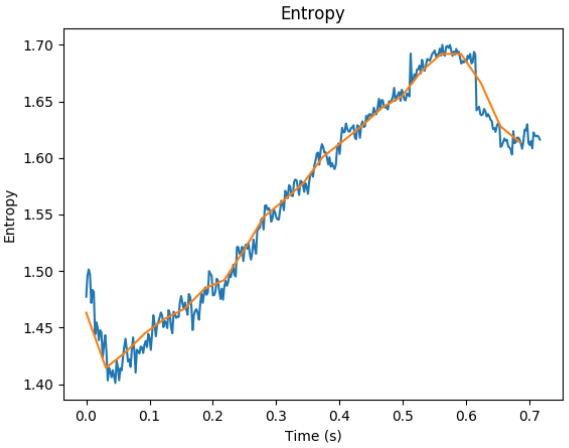

(a) Accelerometer 1

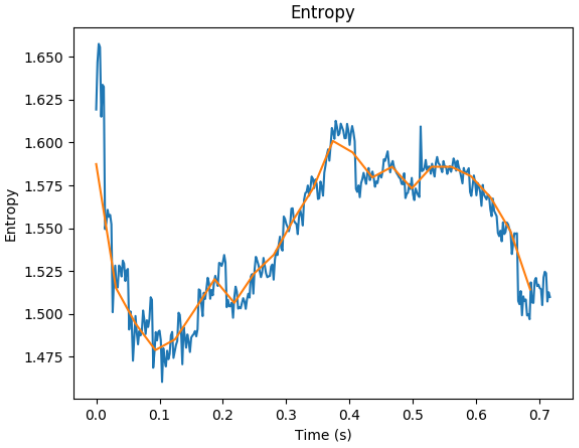

(b) Accelerometer 3

Figure 53: Wavelet Entropy Time series of vibration of the carbon fiber rod as sampled by the accelerometer No.1, 3 when exciting the rod at point 38 during the 2^{nd} test.

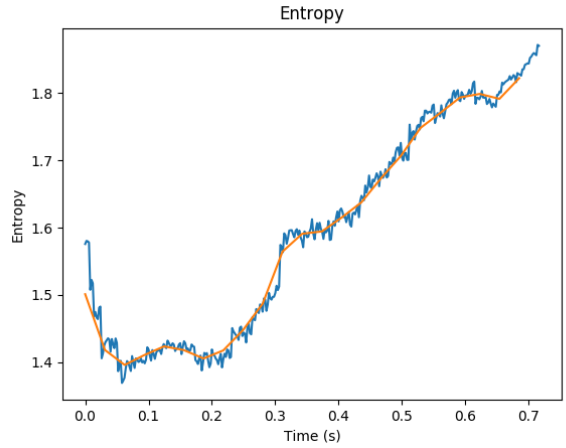

(a) Accelerometer 1

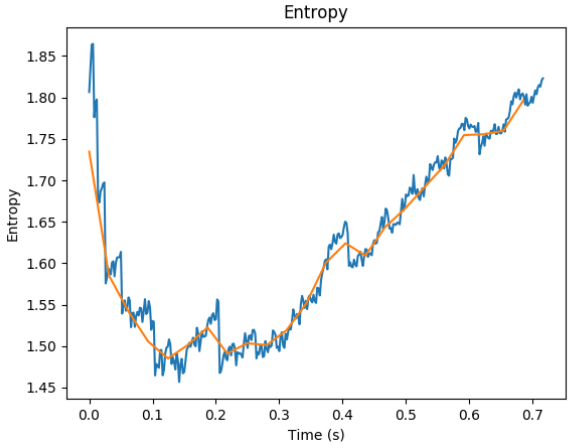

(b) Accelerometer 3

Figure 54: Wavelet Entropy Time series of vibration of the carbon fiber rod as sampled by the accelerometer No.1, 3 when exciting the rod at point 39 during the 1^{st} test.

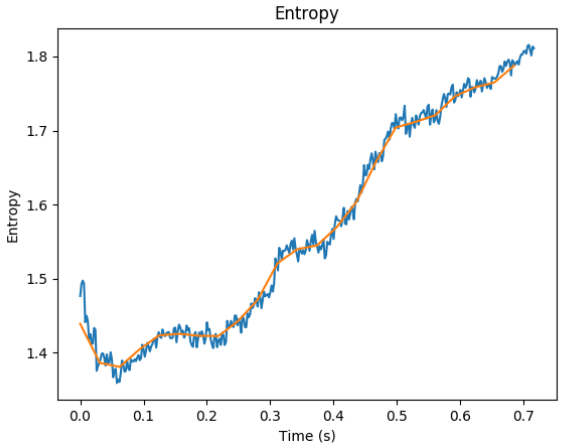

(a) Accelerometer 1

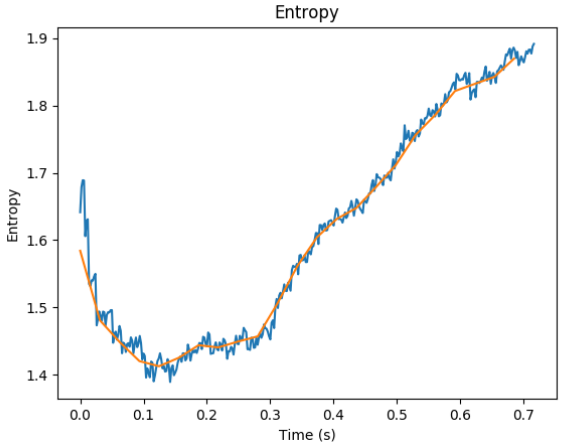

(b) Accelerometer 3

Figure 55: Wavelet Entropy Time series of vibration of the carbon fiber rod as sampled by the accelerometer No.1, 3 when exciting the rod at point 39 during the 2^{nd} test.

Eventually, in point 40 the entropy evolution gradually gets restored to an exponentially decaying path.

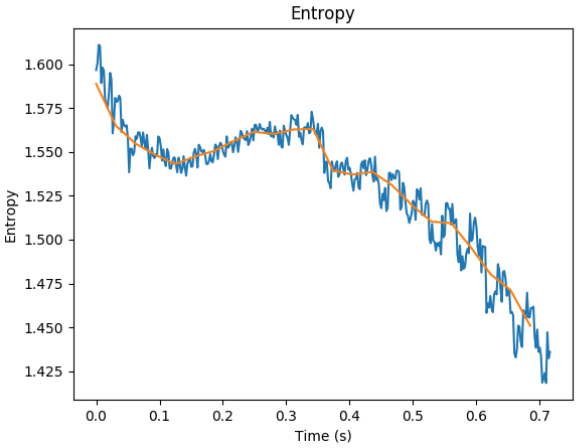

(a) Accelerometer 1

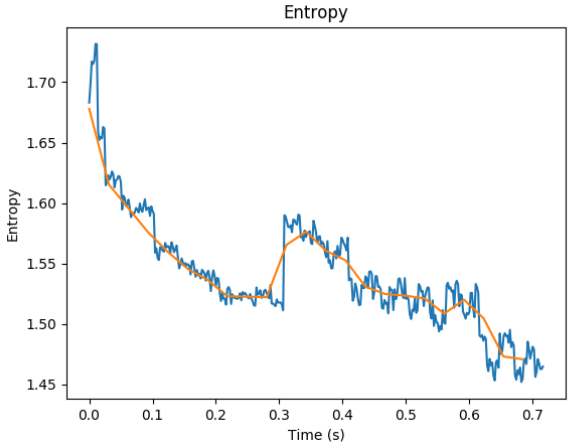

(b) Accelerometer 3

Figure 56: Wavelet Entropy Time series of vibration of the carbon fiber rod as sampled by the accelerometer No.1, 3 when exciting the rod at point 40 during the 1^{st} test.

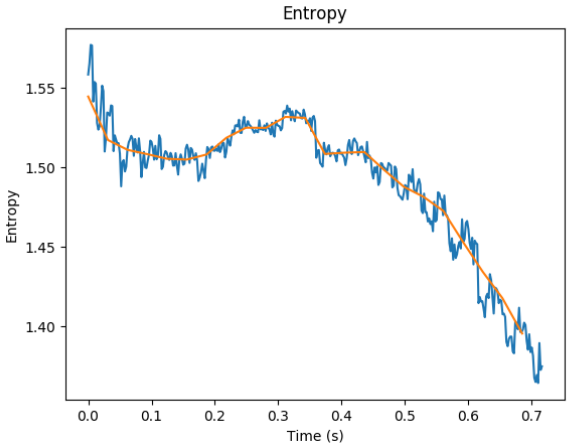

(a) Accelerometer 1

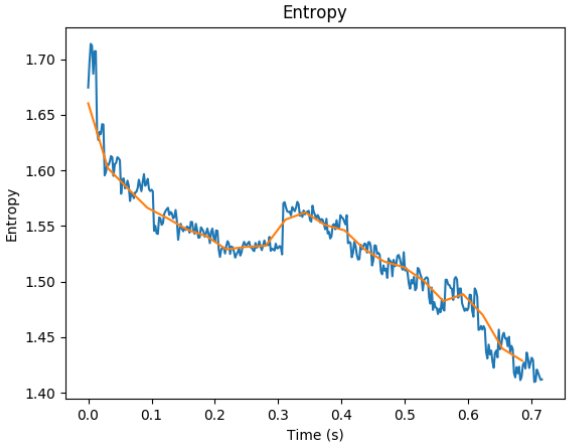

(b) Accelerometer 3

Figure 57: Wavelet Entropy Time series of vibration of the carbon fiber rod as sampled by the accelerometer No.1, 3 when exciting the rod at point 40 during the 2^{nd} test.

6.2.4 Spatial Wavelet Entropy

Following the extrapolation of the Wavelet Entropy Time Series for all locations, the total entropy of the signals was calculated using equation *4.8* and plotted as a function of the location of the tap test (Spatial Wavelet Entropy). For both accelerometers No.1, 3 and both executions of the experiment, the Spatial Wavelet Entropy displayed extreme values at locations 10 and 38 with an increasing trend for the locations neighboring those positions.

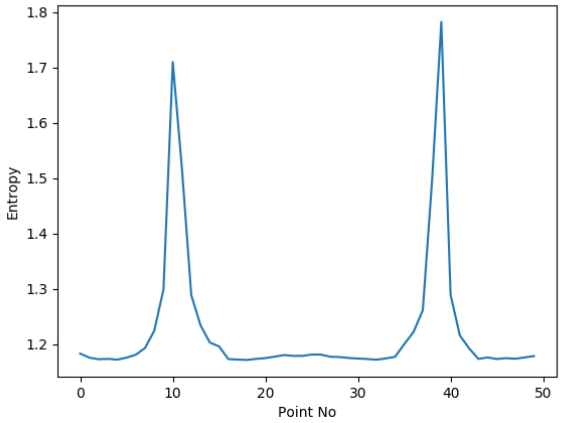

(a) Accelerometer 1

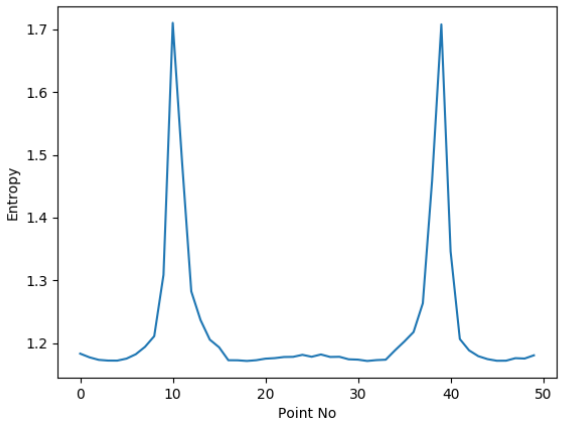

(b) Accelerometer 3

Figure 58: Spatial Wavelet Entropy of the ensemble of signals from the 1^{st} set of tap-tests for accelerometers No.1, 3.

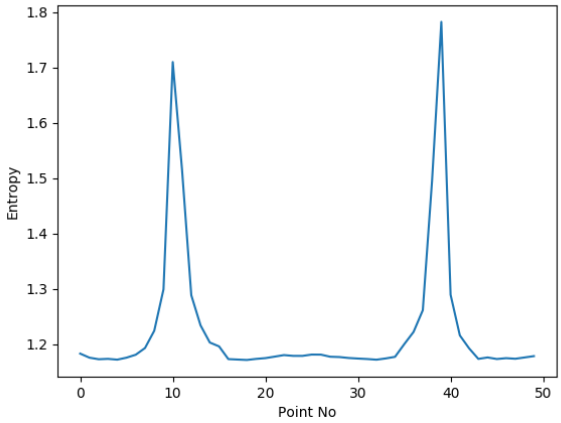

(a) Accelerometer 1

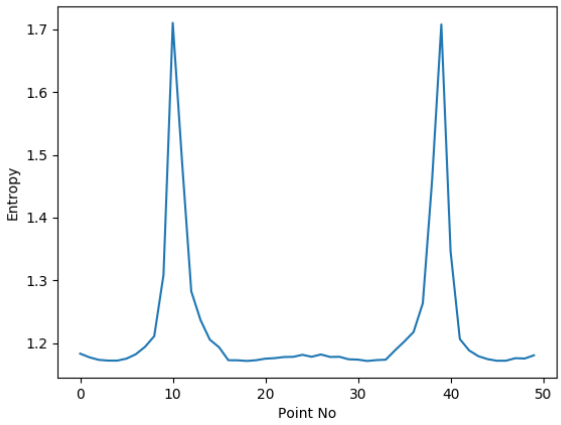

(b) Accelerometer 3

Figure 59: Spatial Wavelet Entropy of the ensemble of signals from the 2^{nd} set of tap-tests for accelerometers No.1, 3.

6.3 Interpretation of results

Wavelet Entropy Time Series identifies two locations, neighboring positions 10 and 38, that when excited by a pulse, the signal acquired exhibits an increasing trend in its informational entropy. Both accelerometers No.1, 3 for both repetitions of the experiment display similar results. The repeatability aspect of the method proves that the exciting the area around these points causes the generated wave to behave differently. This can also be seen when examining the Spatial Wavelet Entropy plots which indicate that the overall signals when exciting in the neighborhood of positions 10 and 38 are significantly more complicated that the rest of the signals. This in combination with the preexisting knowledge that the beam contains air inclusions gives us strong indication that their location is in the proximity of positions 10 and 38.

Any elastic wave traveling through any polycrystalline or multicellular media will generate noise when scattered by the microstructure boundaries [Lobkis and Rokhlin, 2010]. Whilst a composite structure is regarded as anisotropic, it experiences lattice symmetry. The agglomeration of quasi-randomly oriented cells exhibits directional periodicity, similarly to the hypothesis R.J. Haüy [Haüy, 1784] made for a crystalline structure which was then proven by Von Laue Friedrich [von Laue, 1912] using X-Ray diffraction. Therefore, the noise generated when a chirp elastic wave travels through medium has a low signal to noise ratio, as subsequent scattering waves tend to cancel one another [Tant et al., 2015]. Any geometric discontinuities break the pattern of the structure causing waves to scatter differently. An air inclusion can be considered as a smooth geometric discontinuity. Hence, an elastic wave when interacting with it, will scatter [Mow and Pao, 1971]. [Rayleigh, 1872]. The lesser the distance of the air inclusion to the wave source (position of tap test), the more potent the scattering [Kumar et al., 2010], [Mauceri et al., 1999], [Cook and Berthelot, 2001]. Every point of the air inclusion acts like a secondary spherical wave source; these secondary waves therefore are of greater intensity the closer the discontinuity is to the source [Mow and Pao, 1971]. The constructive interference which occurs when the initial wave and the scattered waves add in superposition, essentially increasing the complicatedness of the received signal. This complicatedness can be quantified

by means of the Wavelet Entropy Time Series. An increasing trend in the wavelet Wavelet Entropy Time Series indicates a gradual dispersion of the energy of the signal over time. The assumption made in this thesis is that such a dispersion originates from the scattering caused by a geometric discontinuity inside the specimen.

6.4 Viability of Wavelet Entropy Vibration Testing

Evidently, the proposed method is still in its infancy and therefore, further research is required to investigate its viability. Supposing a destructive testing confirms the existence of air inclusions in the examined carbon fiber beam, Wavelet Entropy Time Series will appear to provide accurate indications for damage in simple geometry composite materials with lattice symmetry.

As Wavelet Entropy Time Series has not been extensively researched, many questions regarding the applicability of the method arise. For start, the robustness of the method for specimens of different materials needs investigating. Furthermore, the effect abrupt geometric changes, including welded joints, as well as, the interaction of the specimen with the accelerometer, have on the accuracy of the damage assessment is yet unclear. From a computational point of view, the *Gibbs* phenomenon presents a mathematical obstacle that needs to be addressed in order to mitigate the numerical interference. Finally, the statistical accuracy of the method demands extensive testing to determine and minimize its p-value.

Should the viability and reliability of the method be verified, Wavelet Entropy Time Series could be a powerful tool in the arsenal of a testing inspector. The only instruments required is a hammer, a relatively low sample rate accelerometer and a processing unit to run a code. Therefore, the testing should requires no experienced testers and can provide quick, effortless results, while being a low cost method.

7 Conclusions

A wavelet entropy based method called Wavelet Entropy Time Series for structural health monitoring is proposed and demonstrated experimentally in this report. Numerical simulations in appendix B proved that Wavelet Entropy Time Series is capable of identifying very subtle but abrupt changes in the dynamics of a system. When the method was applied to a triple harmonic signal with a sudden shift in frequency of a magnitude of 0.1% for one of the sine waves, the method identified correctly the moment of that shift. Appendix C presented a different numerical simulation of the method applied to series of linearly coupled oscillators. This simulation showed, as expected, that the application of the method to linear systems causes the Wavelet Entropy Time Series to have small perturbations around a constant value. Those perturbations derive from the numerical aspect of the computation and also due to the lack of smoothness of the Haar mother wavelet used. In the experimental approach, a composite T-beam which was constructed with air inclusions that locally lower the stiffness of the beam was examined using Wavelet Entropy Time Series from signals obtained from the vibration of the structure after momentary excitation from a composite hammer in different locations. The method seems to identify 2 locations of interest and the attribute of repeatability confirms that locally the response from chirp excitation differs from that of the remainder of the structure. In order to fully comprehend the cause of that different response, a destructive testing is essential. However, the preexisting knowledge that the beam suffers from local air inclusions makes us strongly suspect that they are located in those 2 locations. It is therefore the authors opinion that the method shows promising results with further research required to validate the findings.

Nondestructive characterization for composite materials is generally considered a tedious task [Haldipur and Boone, 2014] and therefore further investigation of the proposed method could prove useful, since the use of only one portable accelerometer with a sample rate of 5000Hz could probably provide adequate information to inspect a composite structure or even other non-composite structures.

Appendices

Appendix A : Signal Processing

Internet, image, sound, phones, radars, sensors, the 21^{st} century is the age of digital information. The dataflow is constant and dominates almost every human aspect of life. But information is useless without a proper way to be processed. Typing your pin number at a bank would produce no results had it not been for a computer to verify your account number. Signal processing hides behind every interaction with an electronic machine, working constantly to produce an outcome from the information given. Now, due to the evolution of computer science and the augmentation of processing power, computers can receive even greater quantities of data and provide almost real time decision making. Wall-Street uses algorithms to predict trends in the stock market by using hundreds of indicators, autonomous vehicles receive data from multiple censors and by running complex algorithms, navigate the vehicle safely.

Obviously, while real life is continuous, computers can only function in a discrete manner. No matter how much the sample rate of a sensor is increased, it will always be unable to measure in a continuous manner. That signal can then be interpreted as a function of real time t, or:

$$signal = function\ x(t),\ t \in \mathbb{R}$$

Signals can also be represented using a Dirac function. If a signal X delineates the measured values of a function $g(t)$ with a sample period T, starting from t_0, X can be defined as:

$$X(t) = \sum_{i=0} g(t)\delta(t_0 + iT - t)$$

The way that signal $X(t)$ will be analyzed in order for desirable result to be accomplished is the subject of signal processing. Fourier transform, Regression analysis, Recurrence relation, Wavelet transform are just a handful of the numerous techniques developed over years

of research that aspired to introduce new ways of extracting useful information from a cluster of seemingly random data. The notion of Wavelet transform is utilized in this thesis to assist in extracting some useful information concerning the health of structure from a cluster of seemingly quasirandom time series describing the vibration of the structure.

A.1 Fourier Analysis

Most, if not all physical phenomenons seem to be far too complicated to be explained simply. How can one describe the insanity of the sea waves? What if those elaborate waves could magically transform and have a new look equivalent to the previous, but effortlessly comprehensible? That was exactly what Jean-Baptiste Joseph Fourier discovered in 1807 by accident, while trying to solve the differential equation of heat diffusion, proving that any periodic function can be represented as an infinite sum of harmonic sinusoids. Albeit it took half a century for the significance of this discovery to be understood, the implications of his work revolutionized many scientific fields.

A.1.1 Fourier Series

Any function of time *f(t)* with a period T can be expressed as an infinite trigonometric series (Fourier series) as shown in equation A.1.

$$\begin{aligned} f(t) = a_0 + a_1 cos\frac{2\pi t}{T} + a_2 cos\frac{4\pi t}{T} + ... \\ + b_1 sin\frac{2\pi t}{T} + b_2 sin\frac{4\pi t}{T} + ... \end{aligned} \tag{A.1}$$

Or:

$$f(t) = a_0 + \sum_{k=1}^{\infty} \left(a_k cos\frac{2\pi kt}{T} + b_k sin\frac{2\pi kt}{T} \right)$$

Where the Fourier coefficients a_0, a_k, b_k are given by:

$$
\begin{aligned}
a_0 &= \frac{1}{T}\int_{-T/2}^{T} f(t)dt \\
a_k &= \frac{2}{T}\int_{-T/2}^{T} f(t)cos\frac{2\pi kt}{T}dt \qquad \text{, k>0} \\
a_k &= \frac{2}{T}\int_{-T/2}^{T} f(t)sin\frac{2\pi kt}{T}dt \qquad \text{, k>0}
\end{aligned} \tag{A.2}
$$

The coefficients a_k, b_k represent the amplitude of the frequency of the k^{th} harmonic:

$$\omega_k = \frac{2k\pi}{T} \tag{A.3}$$

The spacing between adjacent harmonics is:

$$\Delta\omega = \frac{2\pi}{T} \tag{A.4}$$

A.1.2 Fourier Integral

It is clear that an increase in the period T is tantamount to an analogous increase in the spacing of the harmonics. For a non-periodic phenomenon, where T essentially increases to infinity (∞) the spacing is also infinite, thus making it impossible to analyze f into discrete frequency components. The Fourier series then turns into Fourier integral called Fourier Transform, which instead of discrete components a_k, b_k has continuous functions of frequency.

By substituting A.2 into A.1 for a normalized f (a_0=0):

$$
\begin{aligned}
f(t) = &\sum_{k=1}^{\infty}\Big[\frac{2}{T}\int_{-T/2}^{T/2} f(t)cos\frac{2k\pi t}{T}dt\Big]cos\frac{2k\pi t}{T} + \\
&+\sum_{k=1}^{\infty}\Big[\frac{2}{T}\int_{-T/2}^{T/2} f(t)sin\frac{2k\pi t}{T}dt\Big]sin\frac{2k\pi t}{T}
\end{aligned}
$$

Using A.3 and A.4 the above equation becomes:

$$f(t) = \sum_{k=1}^{\infty} \Big[\frac{\Delta\omega}{\pi} \int_{-T/2}^{T/2} f(t) cos(\omega_k t) dt \Big] cos(\omega_k t) + \\ + \sum_{k=1}^{\infty} \Big[\frac{\Delta\omega}{\pi} \int_{-T/2}^{T/2} f(t) sin(\omega_k t) dt \Big] sin(\omega_k t)$$

For $T \to \infty$, $\Delta\omega \to d\omega$, therefore:

$$f(t) = \int_{\omega=0}^{\infty} \frac{1}{\pi} \int_{-\infty}^{\infty} f(t) cos(\omega t) dt cos(\omega t) d\omega \\ + \int_{\omega=0}^{\infty} \frac{1}{\pi} \int_{-\infty}^{\infty} f(t) sin(\omega t) dt sin(\omega t) d\omega$$

By setting

$$A(\omega) = \frac{1}{2\pi} \int_{-\infty}^{\infty} f(t) cos(\omega t) dt$$
$$B(\omega) = \frac{1}{2\pi} \int_{-\infty}^{\infty} f(t) sin(\omega t) dt$$

f(t) becomes:

$$f(t) = \int_{0}^{\infty} A(\omega) cos(\omega t) d\omega + \int_{0}^{\infty} B(\omega) sin(\omega t) d\omega \tag{A.5}$$

Terms A(ω) and B(ω) are the components of the Fourier Transform of f and A.5 is the representation of f by means of the Fourier integral, or simply put the inverse Fourier transform.

In order for the Fourier Transform to represent a function *f(t)*, the function needs to decay to zero as $t \to \infty$ (this condition can be removed when dealing with impulse functions).

A.1.3 Complex Fourier Transform

Since many phenomenons are written in a complex form, by using Euler's formula:

$$e^{it} = cost + isint$$

the Fourier components of a function *f(t)* can be written as:

$$F(\omega) = A(\omega) + iB(\omega)$$

Therefore:

$$\begin{aligned} F(\omega) &= \frac{1}{2\pi}\int_{-\infty}^{\infty} f(t)(cos(\omega t) - isin(\omega t))dt \\ &= \frac{1}{2\pi}\int_{-\infty}^{\infty} f(t)e^{-i\omega t}dt \end{aligned} \tag{A.6}$$

Equation A.6 is considered as the formal definition of the Fourier transform of a function *f(t)*.

Similarly to equation A.5, equation A.7 inverse Fourier Transform gives perfect representation of f from *F(ω)*.

$$f(t) = \int_{0}^{\infty} F(\omega)e^{i\omega t}d\omega \tag{A.7}$$

A.1.4 Discrete Fourier Transform of a Signal x(n)

When using the term signal, one usually refers to a sequence of numbers which may or may not be infinite. A discrete-time signal *x(n)* with n ranging anywhere in $\mathbb{Z}$ is a vector with a format:

$$x = (..., x_{-1}, x_0, x_1, ...) \qquad or \qquad \begin{bmatrix} . \\ x(-1) \\ x(0) \\ x(1) \\ . \end{bmatrix} \tag{A.8}$$

Signals usually represent a value in a specific time moment and are generally measured at a constant sample rate; meaning that if x_k occurred at t_k then, x_{k+1} was measured at $t_{k+1} = t_k + \delta t$, starting from x_o to x_N. In this case, the Fourier integral of *equation A.6* can be replaced by:

$$X_k = \frac{1}{N} \sum_{r=0}^{N-1} x_r e^{-i2\pi kr/N}, \qquad k = 0, 1, .., N-1 \tag{A.9}$$

Equation A.9 is the formal definition of the discrete Fourier transform (DFT) of a signal $\{x_r\}$, r=0,1,2...,N-1. With the inverse discrete Fourier transform (IDFT) giving perfect reconstruction of the initial signal $\{x_r\}$ (*equation A.10*).

$$x_r = \sum_{r=0}^{N-1} X_r e^{i2\pi kr/N} \tag{A.10}$$

The algorithm for calculating the discrete Fourier transform has been improved for providing faster results and called Fast Fourier Transform (FFT).

Suppose we try calculating the values of X_k for k greater than (N-1), suppose (N+m). Then:

$$\begin{aligned} X_{N+m} &= \frac{1}{N} \sum_{r=0}^{N-1} x_r e^{-i2\pi r/N(N+m)} \\ &= \frac{1}{N} \sum_{r=0}^{N-1} x_r e^{-i2\pi mr/N} e^{-i2\pi r} \end{aligned} \tag{A.11}$$

Since the value $e^{-i2\pi mr/N}$ is always equal to 1 for all integer r,

$$X_{N+m} = X_m \tag{A.12}$$

The magnitudes —X_r— therefore, repeat themselves periodically along a frequency axis $\omega_k = 2\pi k/N\Delta$. Furthermore, for real $\{x_r\}$, X_m=-$X_m{}^*$ (complex conjugate of X_m). Therefore, the unique part of the DFT of the signal is in the frequency range:

$$0 \leq \omega_k \leq \frac{2\pi k}{N\delta t} = \frac{\pi}{\delta t} \tag{A.13}$$

Any frequencies above $\frac{\pi}{\delta t}$ present in the signal introduce a distortion called aliasing. As such, when attempting to sample an event with a maximum frequency f, the sampling frequency should be at least F=2f. When sampling with a sampling frequency F, the frequency F/2 is called nyquist frequency and is the maximum frequency of an event that can be detected without causing aliasing.

A.2 Wavelet Transform

Gilbert Strang in a very poetic paper discusses the different means of signal representation and comparing them to an orchestra playing a symphony by Mozart [Strang, 1994]. He compared the Fourier transform to an "infinite orchestra" playing a single steady note. The short time Fourier Transform is then equivalent to the same orchestra with the difference that every instrument changes the note every section; as result, the music piece has abrupt changes at the end of each segment. Both orchestras have significant flaws. The first lacks the ability to display singularities, for example a flute solo, in the symphony. Although, the second can play such singularities the piece sounds really rough at the end of each section. A wavelet orchestra is then a lot closer to how Mozart intended the piece to be played; all instruments play the notes as the mother wavelet ($W(t)$) some sped up, while others slowed down, with the combination giving a smooth piece that can play rhythmic changes.

Wavelet transformation is a relatively young and versatile technique that allows multi-resolution analysis both in time and scale (energy levels) domain. Wavelets ($w_{\alpha,b}(t)$) are small wavelike functions that oscillate for finite time. A special feature of wavelets is that they can be constructed from a single function called mother wavelet ($W(t)$) by scaling α times and shifting the origin time by b, thus allowing the examination of the original signal at different time intervals and scale ranges.

$$w_{\alpha,b}(t) = W\Big(\frac{t-b}{\alpha}\Big), \quad \alpha \in \mathbb{R}^*, b > 0 \tag{A.14}$$

α, b can be continuous in $\mathbb{R}$ (continuous wavelet transform) or discrete (discrete wavelet transform) taking values $\alpha = \alpha_0^m$, $b = nb_0a_0^m$, $\alpha_0 > 1$, $b_0 > 0$ fixed with m,n ranging over $\mathbb{Z}$.

The wavelet transform of a function f(t) is:

$$\begin{aligned} w(\alpha, b; W, f) &= |\alpha|^{-1/2} \int_{-\infty}^{+\infty} f(t)\overline{W\Big(\frac{t-b}{\alpha}\Big)}dt \\ &= \langle f(t)\ ,\ w_{\alpha,b}\rangle \end{aligned} \tag{A.15}$$

A similarity between the Window Fourier Transform and the wavelet transform is that they both take the inner products of the function with a family of functions

The wavelets have a zero average, for that reason, wavelet coefficients can measure the variation of a function f in a neighborhood b proportional to a. Wavelet transform, therefore, excels at characterizing transient events. Sharp signal transitions create large amplitude wavelet coefficients. Singularities can be detected by examining the local maxima of different scales of the wavelet transform.

A.2.1 Continuous Wavelet Transform

For a function $f(t)$, its continuous wavelet transform is given by equation A.16, with the dilation (scaling) and translation (shift of origin) parameters α and b varying continuously.

$$\begin{aligned} w(\alpha, b; W, f) &= |\alpha|^{-1/2} \int_{-\infty}^{+\infty} f(t) \overline{W\Big(\frac{t-b}{\alpha}\Big)} dt \\ &= \langle f(t)\ ,\ w_{\alpha,b} \rangle \end{aligned} \tag{A.16}$$

Equation A.16 essentially is the L^2 inner product of $f(t)$ and $w_{\alpha,b}$.

The function $f(t)$ can then be reconstructed from its wavelet transform by means of the "resolution of identity" formula:

$$f(t) = C_w^{-1} \int_{-\infty}^{+\infty} \int_{-\infty}^{+\infty} \frac{1}{a^2} \langle f(t), w_{\alpha,b}(t) \rangle w_{\alpha,b} d\alpha db \tag{A.17}$$

Where C_w depends only on the mother wavelet function and is given by:

$$C_w = 2\pi \int_{-\infty}^{+\infty} |\hat{W}(\xi)|^2 |\xi|^{-1} d\xi \tag{A.18}$$

Assuming $C_w < \infty$ in order for the math to make physical sense.

Equation A.17 essentially analyses f(t) as a superposition of wavelets $w_{a,b}(t)$, with the coefficients of the basis given from the wavelet transform of f (equation A.16). Therefore, reconstruction of f is possible from its wavelet transform.

A.2.2 Discrete Wavelet Transform

In practice, the CWT is scarcely used, as all digital information is discrete, making the use of discrete wavelet transform (DTW) a one-way. DWT is similar to the CWT with the basic difference that the scaling and translation parameters take discrete values $\alpha = \alpha_0^m$ and $b = nb_0\alpha_0^m$, with $\alpha_o > 1$(for convenience only, it can take any value in $\mathbb{R}$ although the most common value for a_0 is 2 since changing scales means doubling of halving the transitional step), $b_0 > 0$ fixed and $n, m \in \mathbb{Z}$. Therefore, the corresponding family of wavelets $w_{m,n}(t)$ for a mother wavelet $W(t)$ is:

$$\begin{aligned} w_{m,n}(t) &= \alpha_0^{-m/2} W\Big(\frac{t - nb_0\alpha_0^m}{\alpha^m}\Big) \\ &= \alpha_0^{-m/2} W(\alpha_0^m t - nb_o) \end{aligned} \tag{A.19}$$

The Wavelets, $w_{m,n}$, form a base of linearly independent functions that are able to model all admissible functions f(t).

Similarly to CWT, the discrete wavelet transform of a function f(t) is the inner product of $f(t)$ and $w_{\alpha,b} = w_{m,n}$ and is also calculated using equation A.16, meaning the wavelet coefficients of the transform are:

$$b_{mn} = a_0^{-m/2} \int_{-\infty}^{+\infty} f(t)\overline{W(\alpha_0^m t - nb_o)}dt \tag{A.20}$$

For a time series f(t), it must have a power of 2 (2^N) samples in order for the discrete wavelet transform to be calculated.

A.2.3 Mother Wavelet

Any wavelike function can be a wavelet. However, when looking for the property of orthogonality, the mother wavelet (W(t)) should be a function following a specific set of rules [Newland, 2012]. W(t) should come from a dilation equation, or in other words, W(t) should be expressed as a finite series of W(t), where each term is positioned at a different place on the time axis at (2t-k), $k \in \mathbb{Z}$. The dilation equation can be seen in equation A.21.

$$W(t) = c_0 W(2t) + c_1 W(2t-1) + c_2 W(2t-2) + ... \qquad c_i \in \mathbb{R} \tag{A.21}$$

or

$$W(t) = \sum_k c_k W(2t-k), \qquad c_i \in \mathbb{R} \tag{A.22}$$

The equation can not always be solved analytically but is generally solved analytically with consecutive approximations $W_j(x)$ for an initial $W_0(x)$ until it converges to a $W(x)$ that is indistinguishable from the previous.

These coefficients c_i need to follow some conditions in order for the wavelet to be orthogonal.

- Conservation of Area

  Since W(t) is used for a transform, the area under the scaling function should be unitary, or

  $$\int_{-\infty}^{\infty} W(t)dt = 1$$

  However:

  $$\int_{-\infty}^{\infty} W(t)dt = \sum_k c_k \int_{-\infty}^{\infty} W(2t-k)dt$$

  By changing the variable of integration from 2x-k to y then:

  $$\int_{-\infty}^{\infty} W(t)dt = \frac{1}{2}\sum_k c_k \int_{-\infty}^{\infty} W(y)dy = 1$$

  Therefore:

  $$\sum_k c_k = 2$$

- Accuracy (as called by Strang)

  Strang proved [Strang, 1989] that in order for a wavelet expansion to represent accurately a function f(t), the Fourier transform of the scaling function needs to be periodically zero.

  This can be achieved if:

  $$\sum_k (-1)^k k^m e^{-i\pi k} = 0, \qquad \text{for m =0,1,2, ..n-1}$$

- Orthogonality (as called by Strang)

  Gilbert Strang also proved [Strang, 1989] that in order for the wavelets to be bases of an orthogonal basis:

$$\sum_k c_k c_{k+2m} = 0, \qquad \text{for all m except m= 0}$$

  For example, for 6 coefficient wavelet ($c_0 ... c_5$) the condition is:

$$c_0 c_1 + c_1 c_3 + c_2 c_4 + c_3 c_5 = 0, \qquad \text{for m=1}$$

$$c_0 c_4 + c_1 c_5 = 0, \qquad \text{for m=2}$$

As the number of coefficients c_i increases, the wavelets become smoother and resemble closer a smooth harmonic function.

There exists a variety of mother-wavelets, the use of which can significantly alter the wavelet coefficients obtained. Therefore, a dilemma always exists concerning the selection of the best mother wavelet for accurate signal representation. Generally, the ideal mother wavelet is one that resembles the shape of the original signal. As mentioned before, wavelets are wavelike functions that oscillate briefly. An important property of wavelets is that they are well localized both in frequency and time. However, wavelets are not at a single frequency, not even a finite range of frequencies, but they do extend over a finite time period. Nonetheless, scales can be associated with frequency, with different scales providing unique information for subsequent energy levels. Heisenberg's uncertainty principle dictates that as the accuracy of the time localization increases, the frequency accuracy decreases and vice versa. Or more simply put, the more the oscillations in the mother wavelet, the less likely it is for momentary events to be detected. Therefore, since the subject of this research revolves around abrupt changes in the energy distribution of the signal, the simplest mother wavelet the "Haar" wavelet (or Daubechies 1, DB1, wavelet as it is also called) was used.

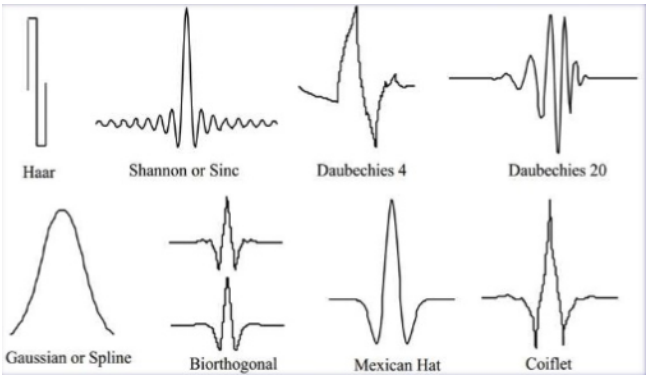

Figure 60: Some mother wavelets

A.2.4 Haar Wavelet

The *Haar* wavelet family is the simplest one. It's mother wavelet function can be described as:

$$W(t) = \begin{cases} 1 & 0 \leq t < \frac{1}{2} \\ -1 & \frac{1}{2} \leq t < 1 \\ 0 & otherwise \end{cases}$$

Where the rescaled *Haar* wavelets are:

$$w_{jk}(t) = 2^{j/2} w(2^j t - k)$$

The *Haar* wavelets constitute an orthogonal basis of the Hilbert space $L^2(\mathbb{R})$ [Strang and Nguyen, 1996]. The orthogonality can be proven by direct integration:

$$\int_{-\infty}^{+\infty} w_{jk}(t) w_{JK}(t) = \delta(j - J)\delta(k - K) \tag{A.23}$$

The main reason $L^2(\mathbb{R})$ space of functions was used instead of $L^p(\mathbb{R})$ [Strang and Nguyen, 1996] is because for an orthogonal wavelet basis, the L^2 norm of $f(t)$ is

$$
\begin{aligned}
||f(t)||^2 = \int_{-\infty}^{+\infty} |f(t)|^2 dt &= \int_{-\infty}^{+\infty} \sum b_{jk} w_{jk}(t)^2 \\
&= \sum \sum b_{jk} bJK \int_{-\infty}^{+\infty} w_{jk}(t) w_{JK}(t) dt \\
&= \sum b_{jk}^2
\end{aligned}
$$

The *Haar* wavelet transform is also invertible, meaning there can be perfect reconstruction of the original signal, using the inverse *Haar* wavelet transform.

For a signal whose length N must be $N = 2^k$, $k \in \mathbb{Z}^*$, its 'Haar" Wavelet Transform has k+1 wavelet scales (or levels as they are also called), the first one being it's mean (scale -1). Scale 0 also has one coefficient and is the convolution of the entire signal with one wavelet the size of the signal. After that, each scale j has 2^j coefficients corresponding to the convolution of consecutive sections of the signal of length $N' = 2^{k-j}$ with wavelets of the same size.

The Haar wavelet transform is essentially a sequence of subsequent highpass and lowpass filtering. The lowpass is a moving average, while the highpass is a moving difference.

For more information on the construction as well as properties of the *Haar* Wavelet, or Wavelets in general refer to [Mallat, 1999] and [Daubechies, 1992].

Appendix B Runge-Kutta Method

In every scientific field, generally speaking, the mathematical description of any phenomenon is represented by the form of a differential equation. Many ordinary differential equations, especially linear ones, can be solved analytically although, many times an analytical solution of an equation can be cumbersome or even straight impossible. Furthermore, in many cases, especially when dealing with a large system of equations, it can be very tedious to attempt an analytical solution. As such, numerical methods are very often used to obtain the solution of such equations.

Numerical solutions are step methods, meaning that they solve they approximate the solution of the differential equations in a space [a,b] with a specific time step. The finer the time step, the more accurate the approximation.

There are many different numerical methods for solving differential equations (Taylor, Runge-Kutta, etc) The most commonly used is the *Runge-Kutta* method.

Runge-Kutta can solve an equation:

$$\begin{cases} y'(x) = f(x, y(x)) \quad , x \in [a, b] \\ y(a) = y_0 \end{cases} \tag{B.1}$$

Where y is the unknown function and y_0 is an initial value. In order for the equation to be solvable, the uniqueness of the solution needs to be reassured.

The *Lipschitz* theorem can prove the uniqueness of the solution of a differential equation.

If the function f is a continuous function in $\mathbb{R}$ that satisfies the *Lipschitz* condition on [a,b], or there exists $L \in \mathbb{R}$ such that for all (x, y_1), (x, y_2), where $x \in [a, b]$, $y_1, y_2 \in \mathbb{R}$:

$$|f(x, y_1) - f(x, y_2)| \leqslant L|y_1 - y_2| \tag{B.2}$$

then the differential equation *(B.1)* has a unique solution.

For an equation:

$$\begin{cases} y'(x) = f(x, y(x)) \quad , x \in [a, b] \\ y(a) = y_0 \end{cases} \tag{B.3}$$

for the pth order *Runge-Kutta* method, an ascending series $\{x_k\}_{k=0}^{n}$ at the interval $[a, b]$ needs to be established.

$$\begin{cases} x_{k+1} = x_k + h_k, \quad k = 0, 1, ...n - 1 \\ x_0 = a \\ X - n = b \end{cases} \tag{B.4}$$

also, $p + 1$ interim points x_{ki} for every $[x_k, x_{k+1}]$ interval need to be defined:

$$\begin{cases} x_{ki} = x_k + a_i h_k, \quad i = 0, 1, ...p \\ a \leqslant a_i \leqslant 1 \\ a_0 = 0, \\ a_p = 1 \end{cases} \tag{B.5}$$

Then the method is defines as:

$$\begin{cases} y_{k0} = y_k \\ y_{ki} = y_k + h_k \sum_{j=0}^{i-1} c_{ij} f(x_k j, y_k j) \\ i = 1, ..., p \\ y_{k+1} = y_{kp} \end{cases} \tag{B.6}$$

Assuming $y_k = y(x_k)$ the coefficients a_i, $c_i j$ are assigned accordingly, in or the *Taylor* expansion

of both variables of every $y_k i,\ i = 1, ..., p$ at (x_k, y_k) to coincide with the Taylor expansion of the exact solution $y(x_k i)$ at x_k. Should $i = p$, then those *Taylor* expansions coincide up to the terms h_k^m, and the method is of order m.

The 4^{th} order *Runge-Kutta* method is the one used in this thesis for it: $m = p = 4$. The process for a differential equation,

$$\begin{cases} y'(x) = f(x, y(x)) \quad , x \in [a, b] \\ y(a) = y_0 \end{cases} \tag{B.7}$$

where $x \in \{x_k\}_{k=0}^n = x_0, ...x_n$ with $x_{k+1} = x_k + h$ and $x_0 = a$, $x_n = b$ is given as:

$$\begin{cases} z_1 = hf(x_k, y_k) \\ z_2 = hf(x_k + \frac{h}{2}, y_k + \frac{z_1}{2}) \\ z_3 = h_f(x_k + \frac{h}{2}, y_k + \frac{z_2}{2}) \\ z_4 = hf(x_k + h, y_k + z_3) \\ y_{k+1} = y_k + \frac{1}{6}(z_1 + 2z_2 + 2z_3 + z_4) \end{cases} \tag{B.8}$$

This method was used for the numerical approximation of the system of linear dumped oscillations in the numerical simulation of Appendix C.

Appendix C : Algorithms developed for the purpose of this thesis

For the purpose of this thesis, an algorithm was developed with regard to analyzing vibration signals, transforming them using the *Haar* wavelet transform, computing the wavelet entropy time series, plotting, and saving it. That algorithm was implemented in a *Python* programming language and was run in a Unix operating system. Both numerical simulations, in order to

produce the signal, were solved in a *Matlab* environment. Especially, for the coupled linear oscillators, a 4^{rth} order Runge-Kutta was developed in order to solve their differential equation.

The initial signals, both from the structure vibration, and the simulations were saved in a txt file format and read by the script, having their sampling frequency adjusted to 5000Hz by skipping an appropriate number of samples.

The libraries:

- *NumPy* [Harris et al., 2020]
- *SciPy* [Virtanen et al., 2020]
- *Pandas* [pandas development team, 2020], [Wes McKinney, 2010]
- *Math* [Van Rossum, 2020]

were utilized for various mathematical computations, while the library *Matplotlib* [Hunter, 2007a] availed itself of plotting and saving all the figures and diagrams. Finally, the wavelet transform was computed using the *PyWavelets* library [Lee et al., 2019b].

The python script, although long, is rather straight forward and the process is explained in detail over this thesis. That being said, the selection of wavelet coefficients that are active in each window according to *section* 4.5.1 could be baffling. As such, the function of the script for that selection can be seen here.

```
def coefficients_of_section(coefficients, section_starting_point, section_ending_point, signal_length):
    # The purpose of this function is to identify the wavelet coefficients which are active at the section examined.
    # The function takes arguments:
    #                                 the wavelet coefficients "coefficients"
    #                                 the starting point of the section "section_starting_point"
    #                                 the ending point of the section "section_ending_point"
    #                                 the length of the section "signal_length"
    #
    # Each level j has 2^j coefficients each spanning over  "signal_length/(2^j)"  points.
    # Therefore, coefficient Dj(k), or level j and translation k:
    #
    #                           starts at             coefficient_starting_point = k*signal_length/(2^j)
    #                           ends at               coefficient_ending_point = (k+1)*signal_length/(2^j)
    #
    # A coefficient is considered to be active in the section, if its span interlaps with the span of the section.
    #
    #
    #
    #
    # the final section of the signal will not be a valid one if it has an ending point greater than the signal length.
    # This will happen if the step is not a power of 2 for signal lengths that are a power of 2.
    if section_ending_point > signal_length:
        return None

    number_of_levels = np.shape(coefficients)[0]    # The total number of scales/levels of the transform.
    section_coefficients = [[] for x in range(0, number_of_levels)]     # Creating a list with as many empty items as
    # the total number of scales/levels of the transform. The nth item of the list shall be the coefficients of the
    # nth scale that are active on the window.
    for jj in range(0, number_of_levels):   # for every level/scale jj
        first_value = True
        No_of_coefficients_in_level = len(coefficients[jj])
        coefficient_active = False
        for kk in range(0, No_of_coefficients_in_level):
            # For every translation k
            flag = coefficient_active
            coefficient_active = False
            coefficient_starting_point = kk * signal_length / (2 ** jj)     # Beginning of the span of the coefficient
            # in the time domain.
            coefficient_ending_point = (kk + 1) * signal_length / (2 ** jj)     # End of the span of the coefficient
            # in the time domain.
            #
            #
            # Conditions for the coefficient to be active on the window
            if (section_starting_point <= coefficient_starting_point <= section_ending_point) or \
               (section_starting_point <= coefficient_ending_point <= section_ending_point) or \
               (coefficient_starting_point <= section_starting_point <= coefficient_ending_point) or \
               (coefficient_starting_point <= section_ending_point <= coefficient_ending_point):
                coefficient_active = True
            elif flag and not coefficient_active:
                # if previous coefficient was active and this is not, no need to check anymore at that level
                break

            if coefficient_active:
                if first_value:
                    if jj == 0:
                        section_coefficients[jj] = [coefficients[jj]]
                        first_value = False
                    else:
                        section_coefficients[jj] = [coefficients[jj][kk]]
                        first_value = False
                else:
                    section_coefficients[jj] = np.append(section_coefficients[jj], coefficients[jj][kk])
    return section_coefficients
```

Appendix D : Wavelet Entropy Time Series figures

Wavelet Entropy Time Series of Point 0

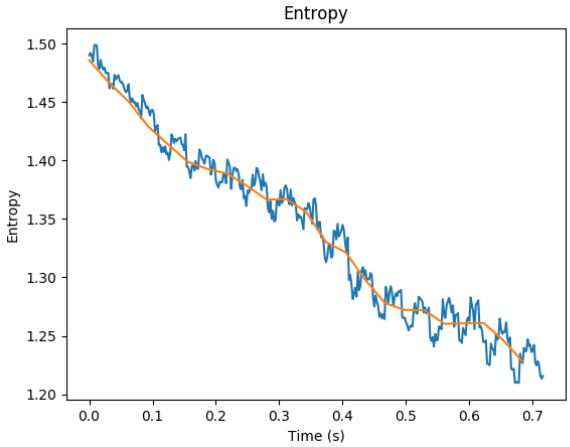

(a) Accelerometer 1

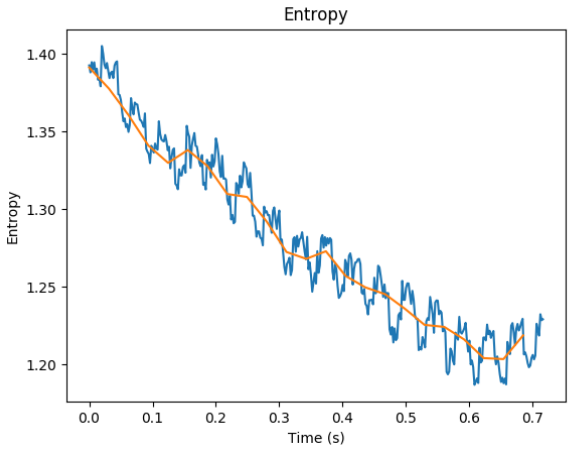

(b) Accelerometer 3

Figure 61: Wavelet Entropy Time series of vibration of the carbon fiber rod as sampled by the accelerometer No.1, 3 when exciting the rod at point 0 during the 1^{st} test.

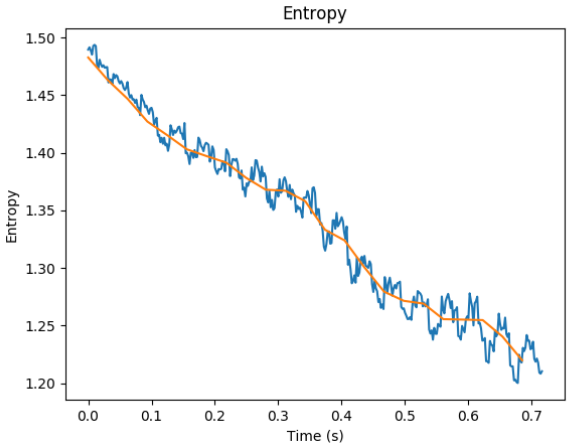

(a) Accelerometer 1

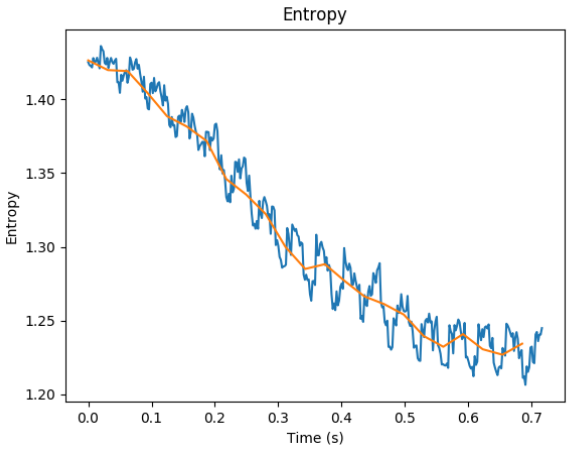

(b) Accelerometer 3

Figure 62: Wavelet Entropy Time series of vibration of the carbon fiber rod as sampled by the accelerometer No.1, 3 when exciting the rod at point 0 during the 2^{nd} test.

Wavelet Entropy Time Series of Point 1

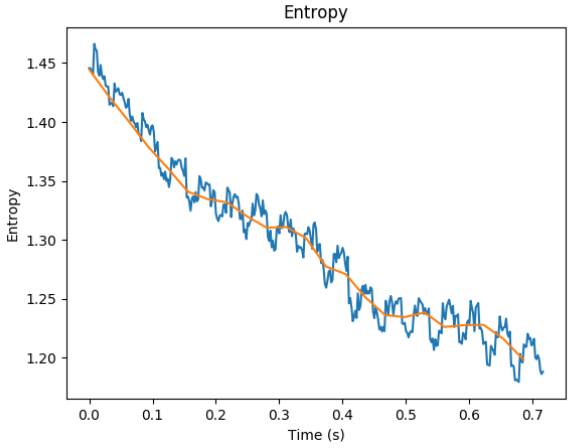

(a) Accelerometer 1

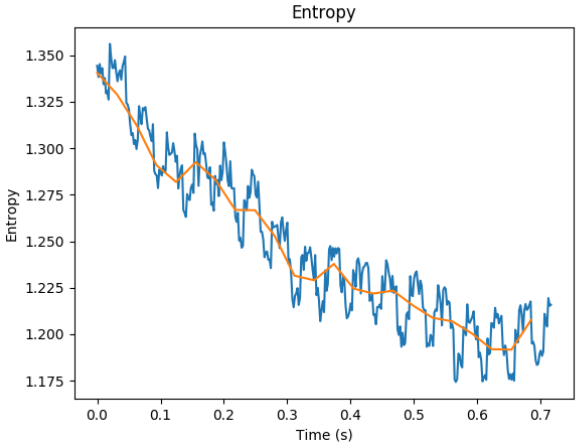

(b) Accelerometer 3

Figure 63: Wavelet Entropy Time series of vibration of the carbon fiber rod as sampled by the accelerometer No.1, 3 when exciting the rod at point 1 during the 1^{st} test.

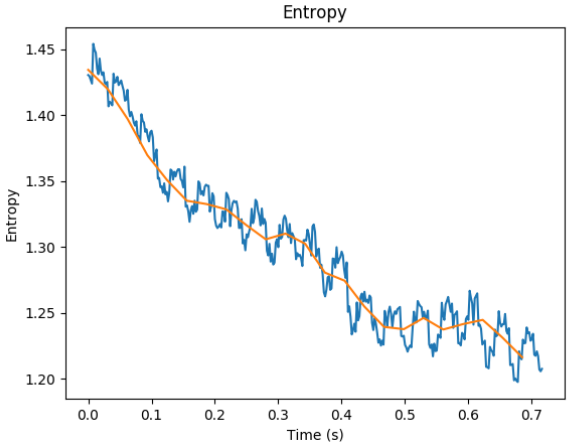

(a) Accelerometer 1

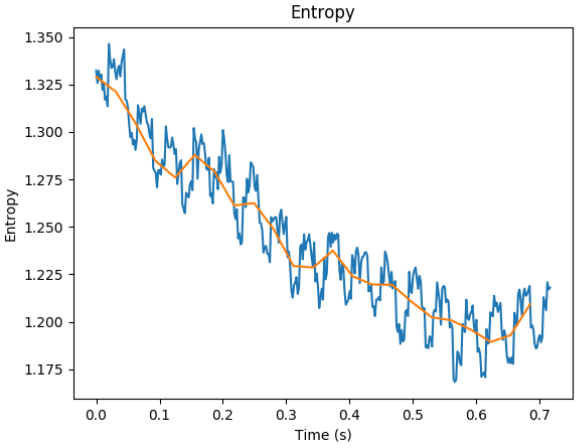

(b) Accelerometer 3

Figure 64: Wavelet Entropy Time series of vibration of the carbon fiber rod as sampled by the accelerometer No.1, 3 when exciting the rod at point 1 during the 2^{nd} test.

Wavelet Entropy Time Series of Point 2

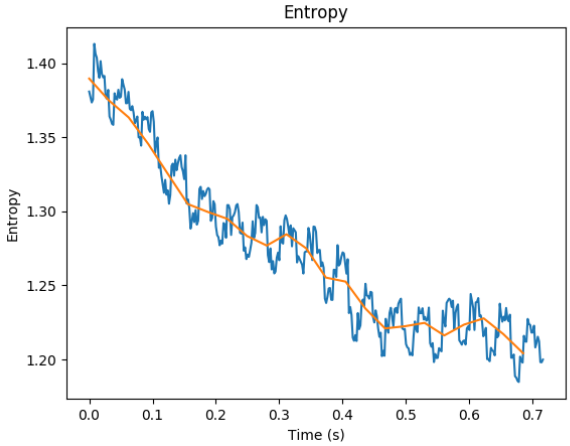

(a) Accelerometer 1

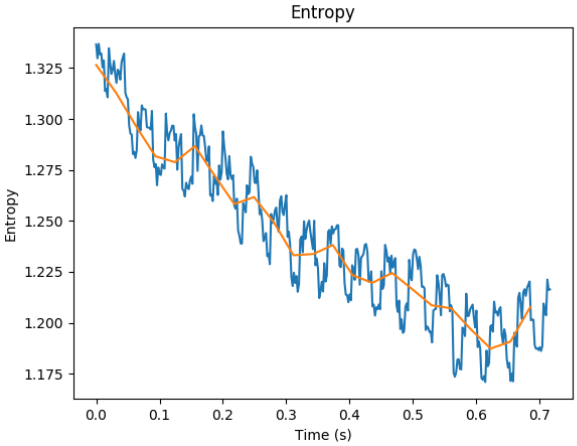

(b) Accelerometer 3

Figure 65: Wavelet Entropy Time series of vibration of the carbon fiber rod as sampled by the accelerometer No.1, 3 when exciting the rod at point 2 during the 1^{st} test.

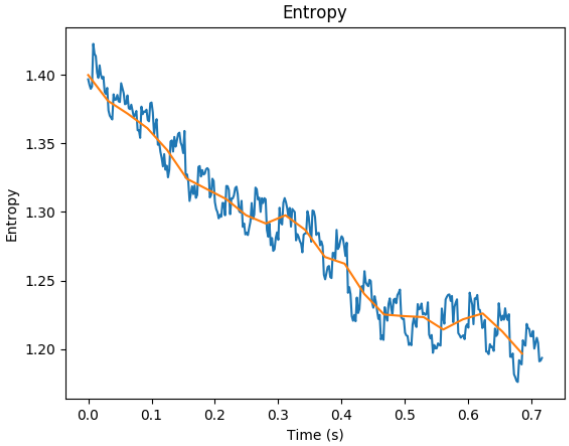

(a) Accelerometer 1

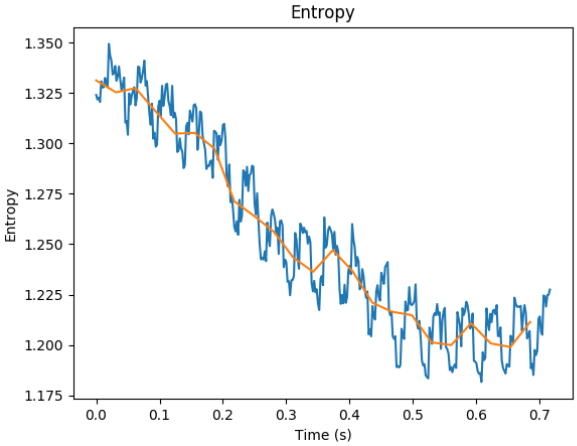

(b) Accelerometer 3

Figure 66: Wavelet Entropy Time series of vibration of the carbon fiber rod as sampled by the accelerometer No.1, 3 when exciting the rod at point 2 during the 2^{nd} test.

Wavelet Entropy Time Series of Point 3

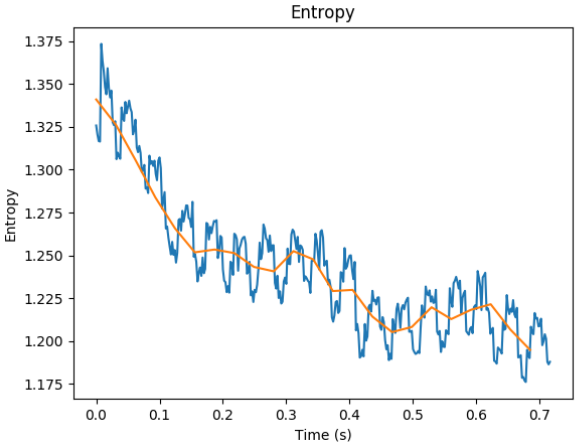

(a) Accelerometer 1

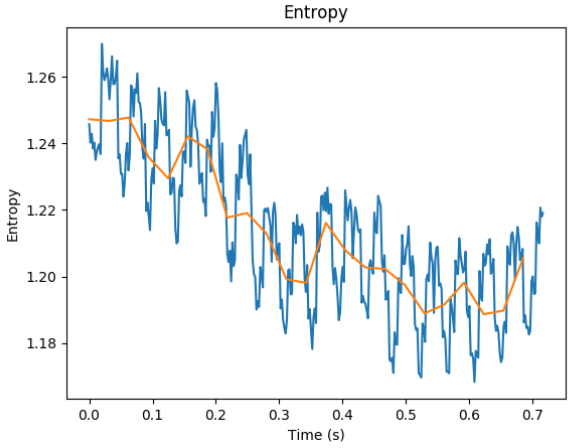

(b) Accelerometer 3

Figure 67: Wavelet Entropy Time series of vibration of the carbon fiber rod as sampled by the accelerometer No.1, 3 when exciting the rod at point 3 during the 1^{st} test.

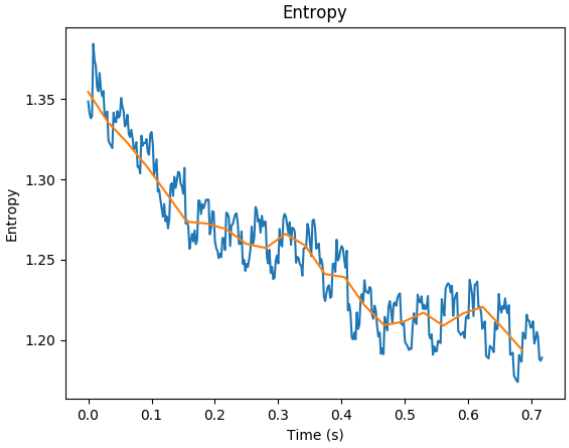

(a) Accelerometer 1

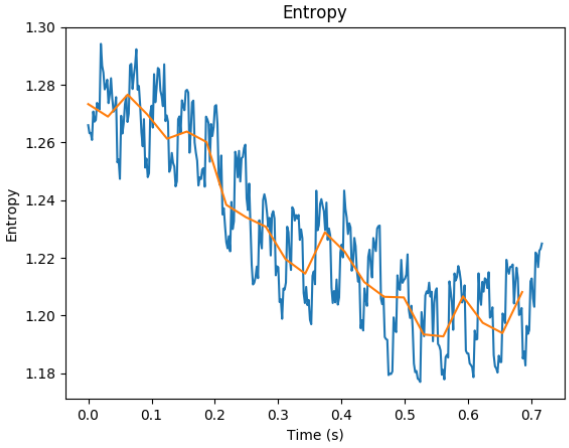

(b) Accelerometer 3

Figure 68: Wavelet Entropy Time series of vibration of the carbon fiber rod as sampled by the accelerometer No.1, 3 when exciting the rod at point 3 during the 2^{nd} test.

Wavelet Entropy Time Series of Point 4

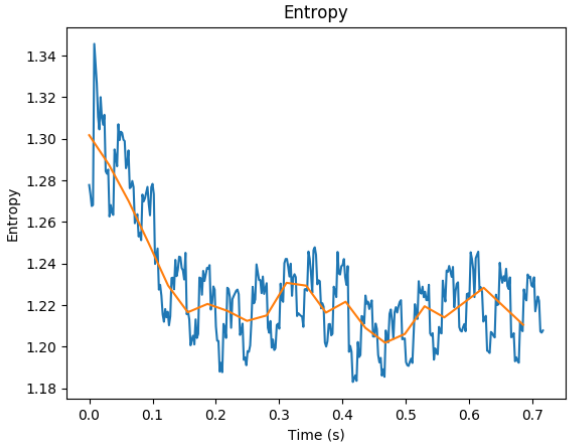

(a) Accelerometer 1

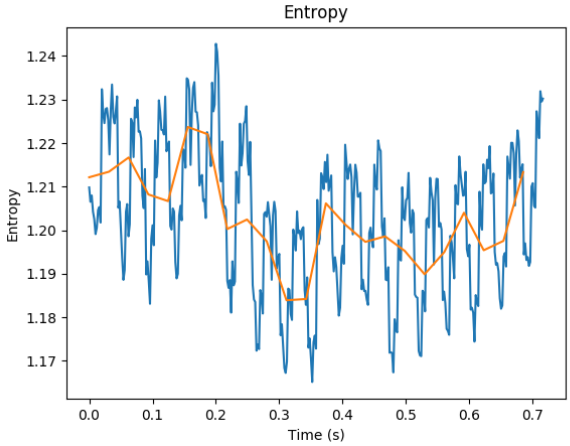

(b) Accelerometer 3

Figure 69: Wavelet Entropy Time series of vibration of the carbon fiber rod as sampled by the accelerometer No.1, 3 when exciting the rod at point 4 during the 1^{st} test.

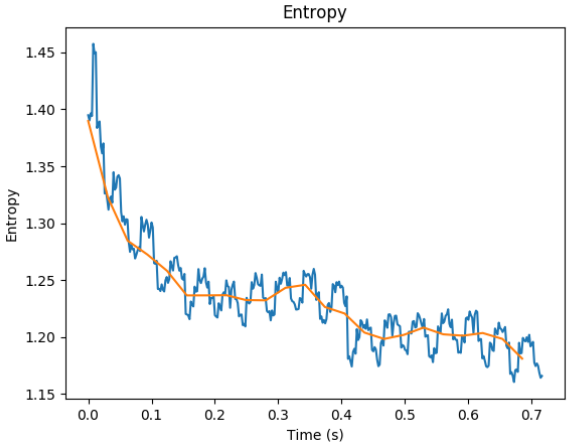

(a) Accelerometer 1

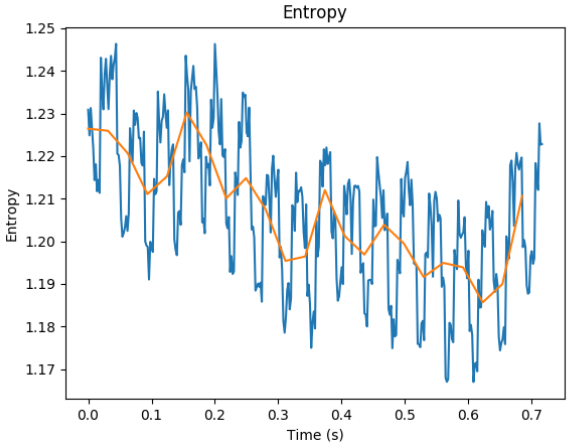

(b) Accelerometer 3

Figure 70: Wavelet Entropy Time series of vibration of the carbon fiber rod as sampled by the accelerometer No.1, 3 when exciting the rod at point 4 during the 2^{nd} test.

Wavelet Entropy Time Series of Point 5

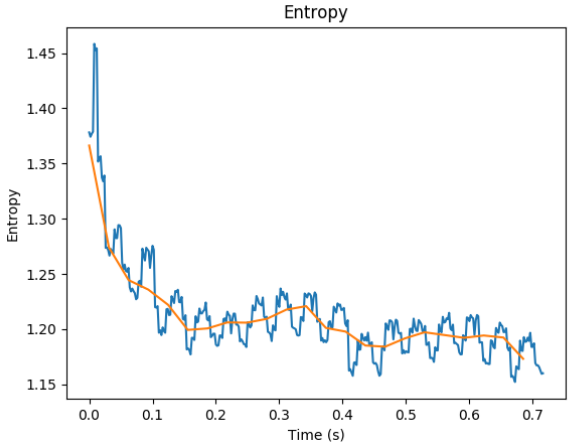

(a) Accelerometer 1

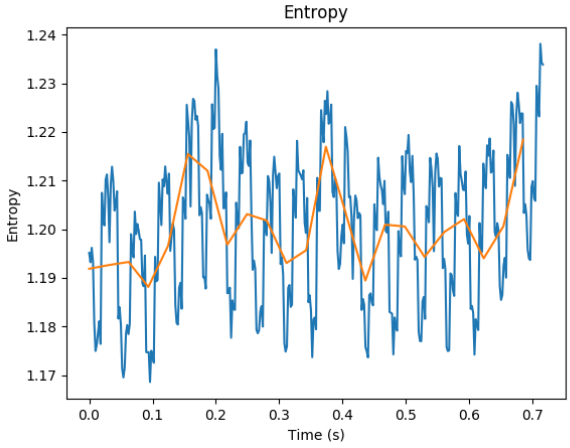

(b) Accelerometer 3

Figure 71: Wavelet Entropy Time series of vibration of the carbon fiber rod as sampled by the accelerometer No.1, 3 when exciting the rod at point 5 during the 1^{st} test.

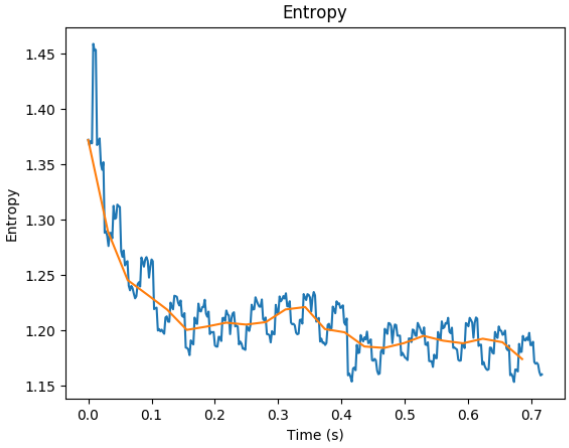

(a) Accelerometer 1

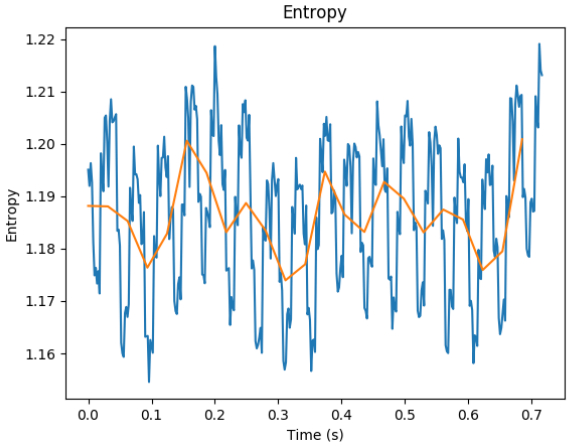

(b) Accelerometer 3

Figure 72: Wavelet Entropy Time series of vibration of the carbon fiber rod as sampled by the accelerometer No.1, 3 when exciting the rod at point 5 during the 2^{nd} test.

Wavelet Entropy Time Series of Point 6

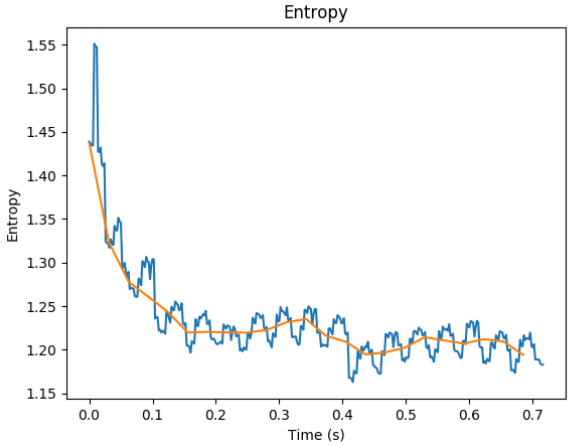

(a) Accelerometer 1

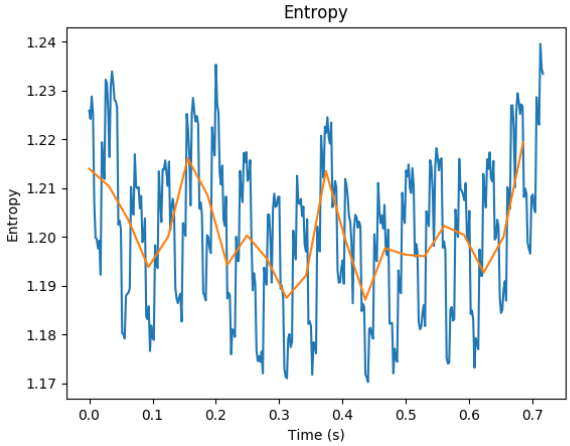

(b) Accelerometer 3

Figure 73: Wavelet Entropy Time series of vibration of the carbon fiber rod as sampled by the accelerometer No.1, 3 when exciting the rod at point 6 during the 1^{st} test.

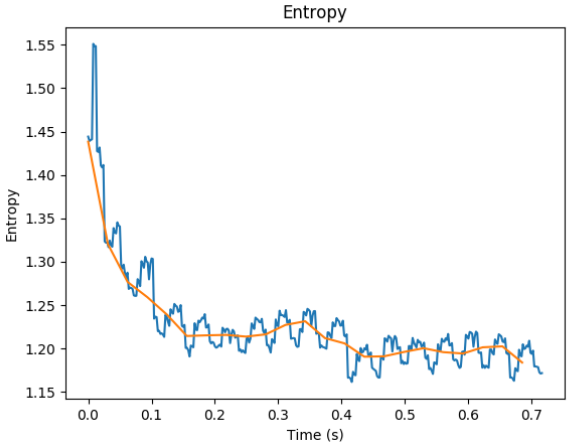

(a) Accelerometer 1

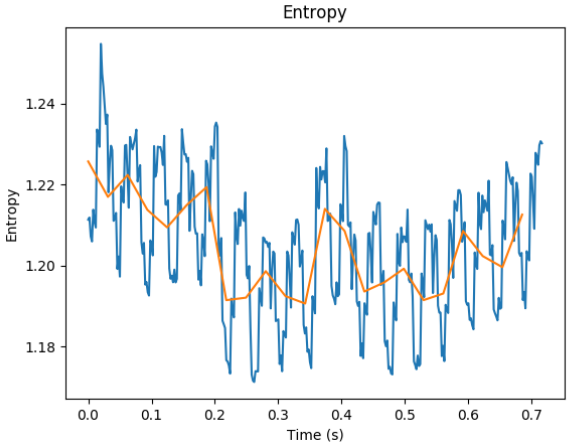

(b) Accelerometer 3

Figure 74: Wavelet Entropy Time series of vibration of the carbon fiber rod as sampled by the accelerometer No.1, 3 when exciting the rod at point 6 during the 2^{nd} test.

Wavelet Entropy Time Series of Point 7

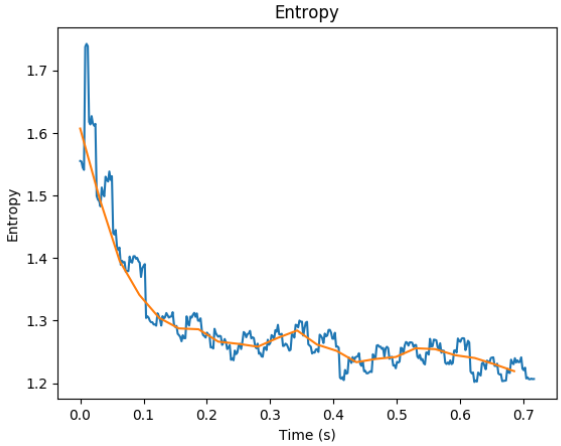

(a) Accelerometer 1

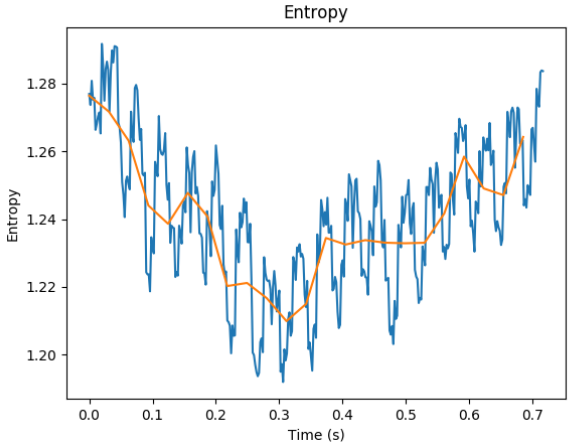

(b) Accelerometer 3

Figure 75: Wavelet Entropy Time series of vibration of the carbon fiber rod as sampled by the accelerometer No.1, 3 when exciting the rod at point 7 during the 1^{st} test.

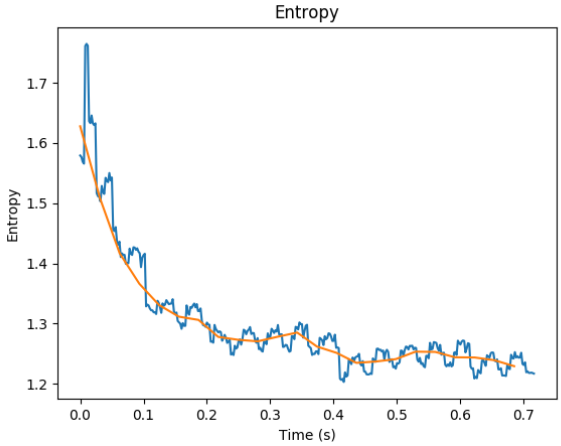

(a) Accelerometer 1

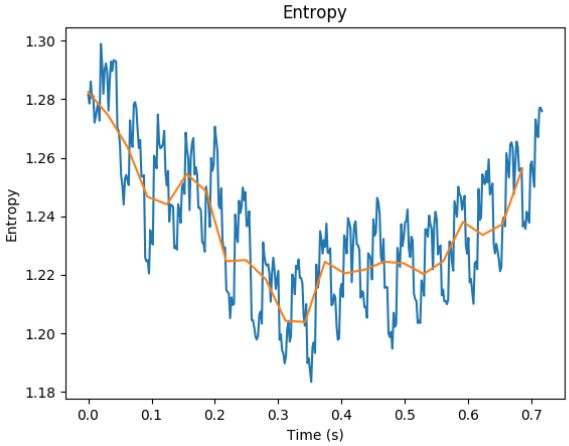

(b) Accelerometer 3

Figure 76: Wavelet Entropy Time series of vibration of the carbon fiber rod as sampled by the accelerometer No.1, 3 when exciting the rod at point 7 during the 2^{nd} test.

Wavelet Entropy Time Series of Point 8

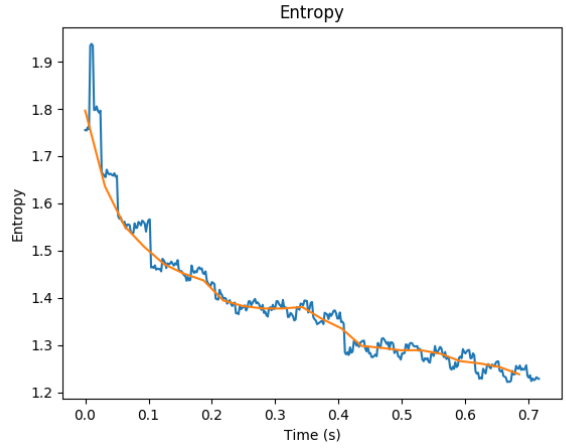

(a) Accelerometer 1

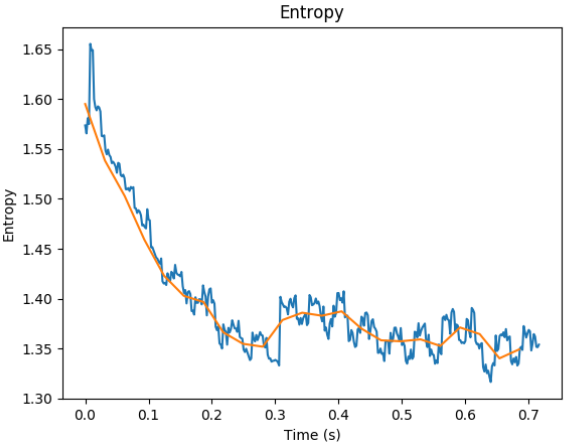

(a) Accelerometer 1

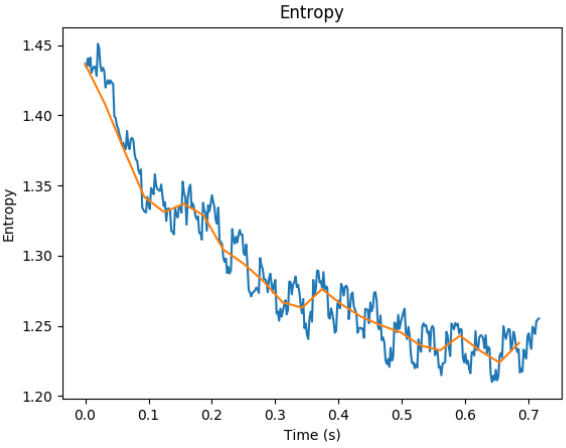

(b) Accelerometer 3

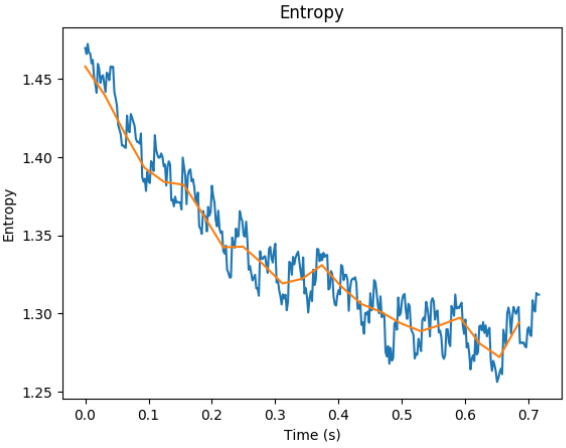

(b) Accelerometer 3

Figure 77: Wavelet Entropy Time series of vibration of the carbon fiber rod as sampled by the accelerometer No.1, 3 when exciting the rod at point 8 during the 1^{st} test.

Figure 78: Wavelet Entropy Time series of vibration of the carbon fiber rod as sampled by the accelerometer No.1, 3 when exciting the rod at point 8 during the 2^{nd} test.

Wavelet Entropy Time Series of Point 9

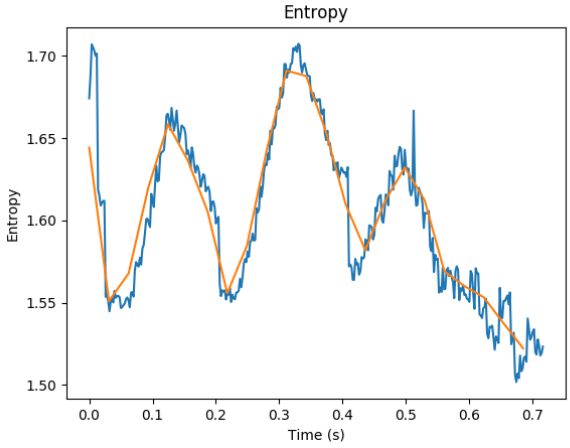

(a) Accelerometer 1

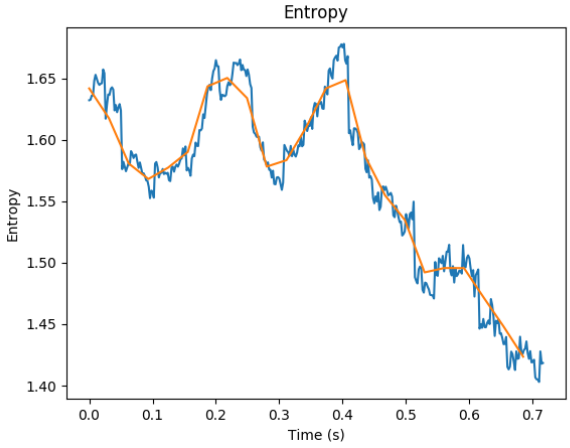

(b) Accelerometer 3

Figure 79: Wavelet Entropy Time series of vibration of the carbon fiber rod as sampled by the accelerometer No.1, 3 when exciting the rod at point 9 during the 1^{st} test.

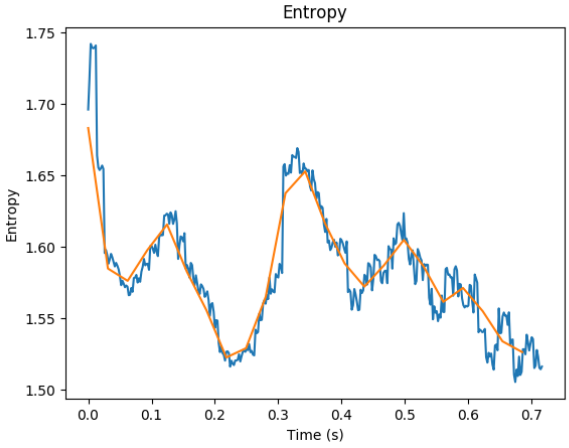

(a) Accelerometer 1

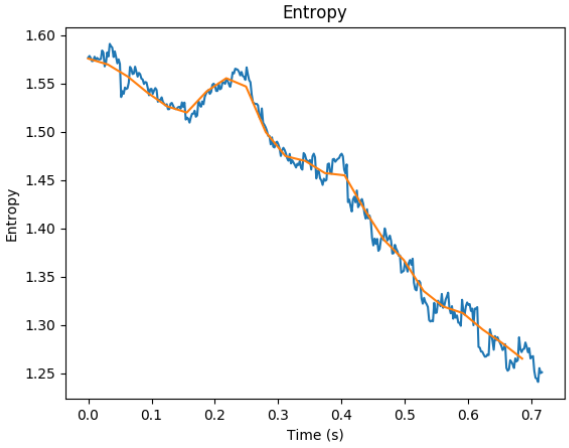

(b) Accelerometer 3

Figure 80: Wavelet Entropy Time series of vibration of the carbon fiber rod as sampled by the accelerometer No.1, 3 when exciting the rod at point 9 during the 2^{nd} test.

Wavelet Entropy Time Series of Point 10

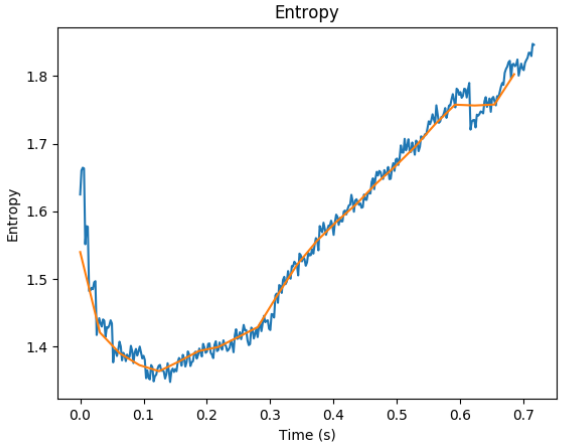

(a) Accelerometer 1

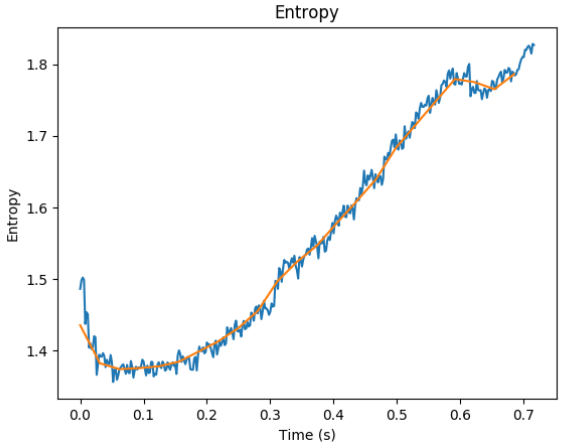

(b) Accelerometer 3

Figure 81: Wavelet Entropy Time series of vibration of the carbon fiber rod as sampled by the accelerometer No.1, 3 when exciting the rod at point 10 during the 1^{st} test.

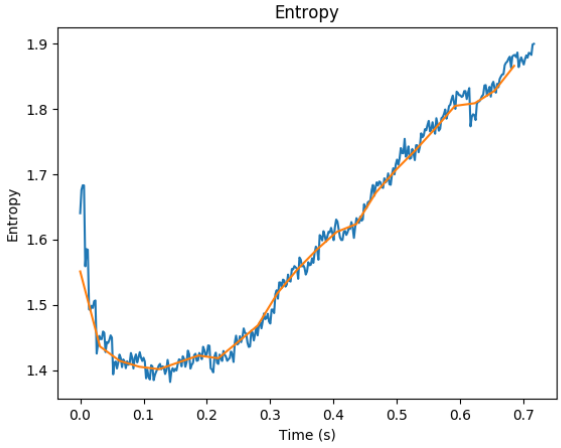

(a) Accelerometer 1

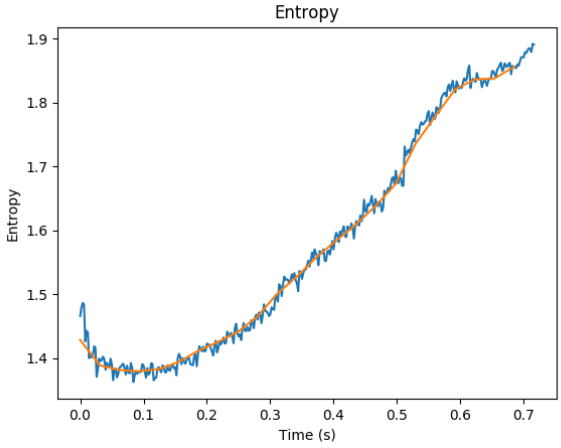

(b) Accelerometer 3

Figure 82: Wavelet Entropy Time series of vibration of the carbon fiber rod as sampled by the accelerometer No.1, 3 when exciting the rod at point 10 during the 2^{nd} test.

Wavelet Entropy Time Series of Point 11

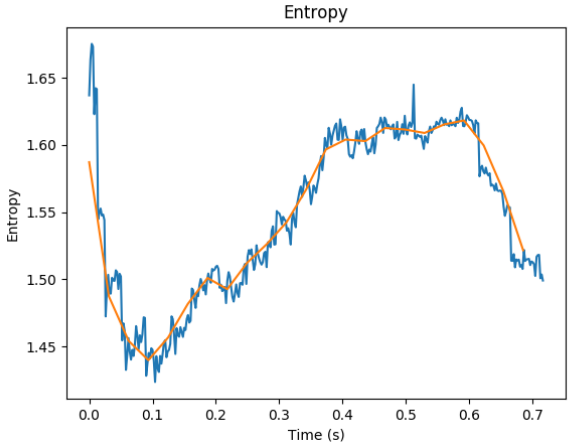

(a) Accelerometer 1

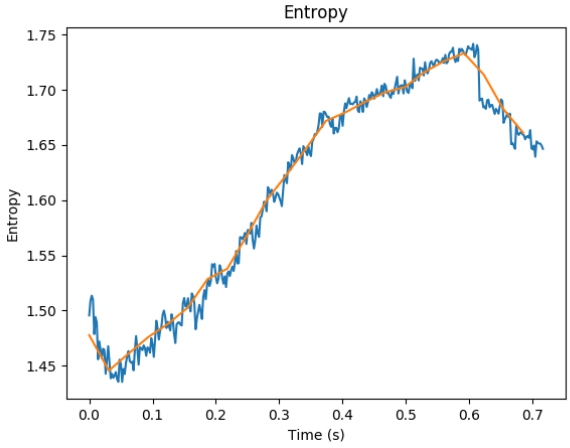

(b) Accelerometer 3

Figure 83: Wavelet Entropy Time series of vibration of the carbon fiber rod as sampled by the accelerometer No.1, 3 when exciting the rod at point 11 during the 1^{st} test.

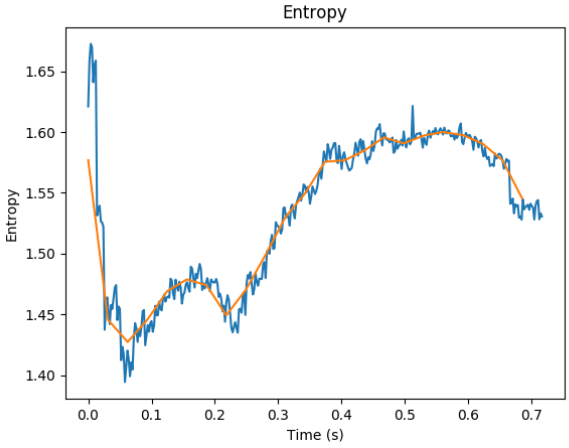

(a) Accelerometer 1

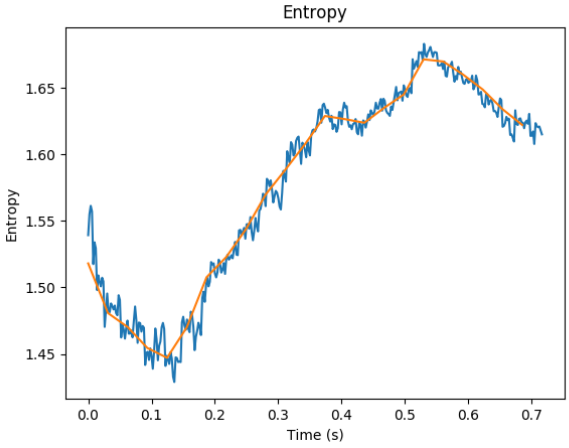

(b) Accelerometer 3

Figure 84: Wavelet Entropy Time series of vibration of the carbon fiber rod as sampled by the accelerometer No.1, 3 when exciting the rod at point 11 during the 2^{nd} test.

Wavelet Entropy Time Series of Point 12

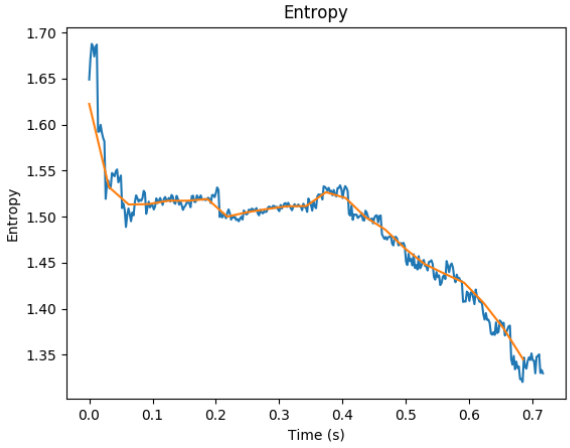

(a) Accelerometer 1

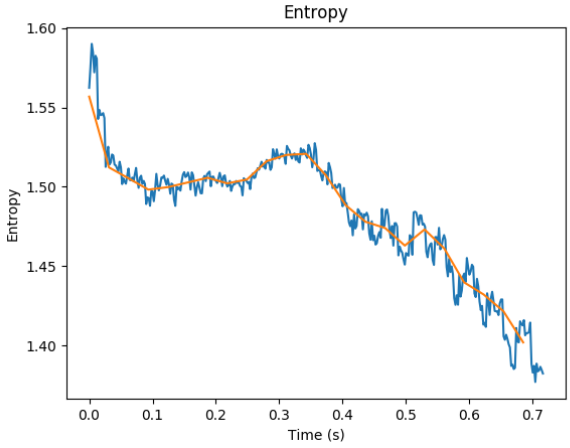

(b) Accelerometer 3

Figure 85: Wavelet Entropy Time series of vibration of the carbon fiber rod as sampled by the accelerometer No.1, 3 when exciting the rod at point 12 during the 1^{st} test.

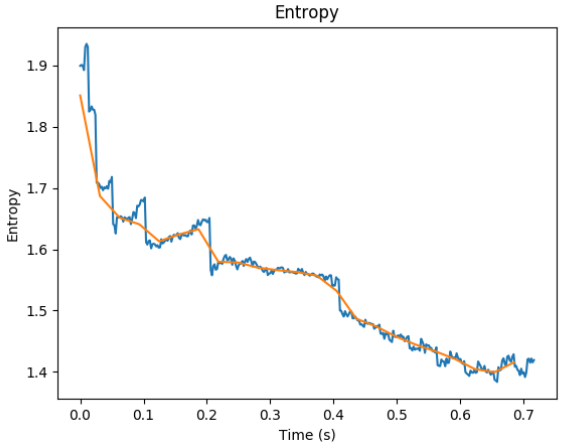

(a) Accelerometer 1

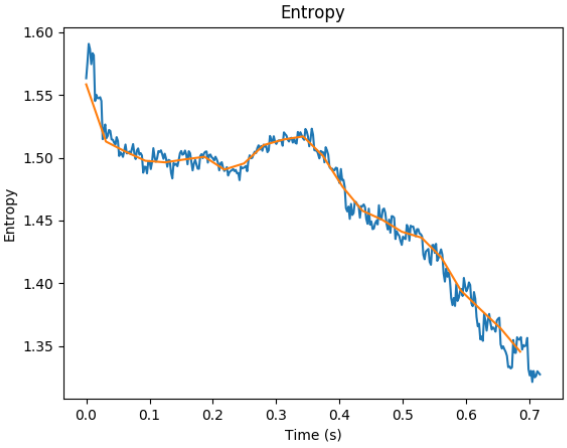

(b) Accelerometer 3

Figure 86: Wavelet Entropy Time series of vibration of the carbon fiber rod as sampled by the accelerometer No.1, 3 when exciting the rod at point 12 during the 2^{nd} test.

Wavelet Entropy Time Series of Point 13

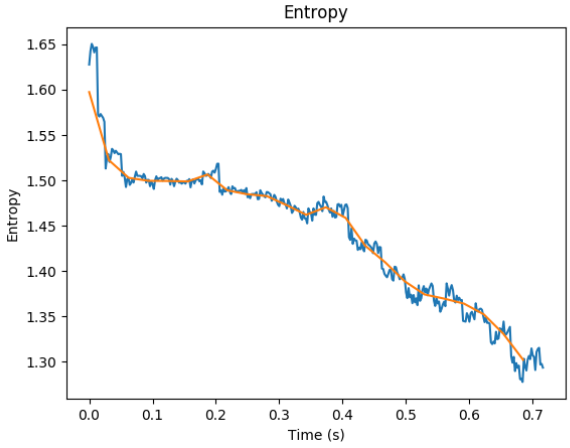

(a) Accelerometer 1

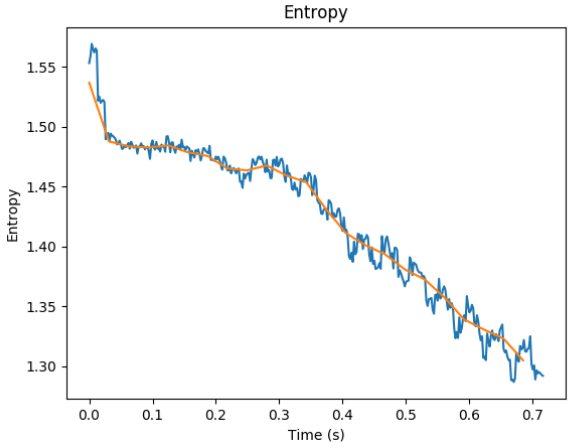

(b) Accelerometer 3

Figure 87: Wavelet Entropy Time series of vibration of the carbon fiber rod as sampled by the accelerometer No.1, 3 when exciting the rod at point 13 during the 1^{st} test.

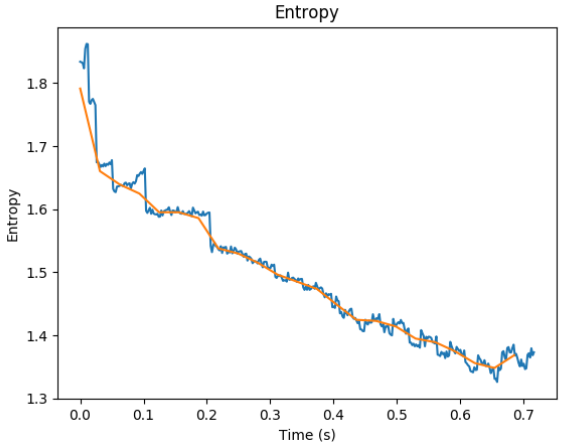

(a) Accelerometer 1

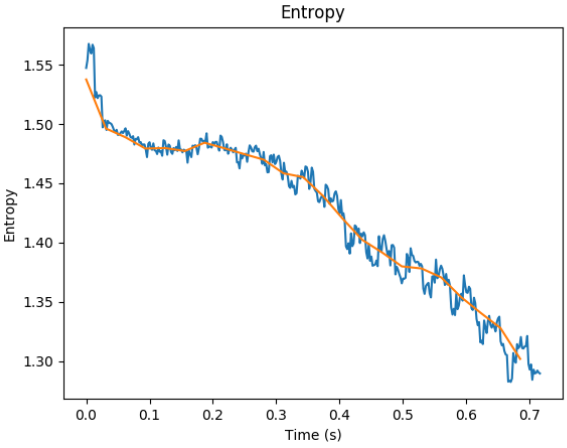

(b) Accelerometer 3

Figure 88: Wavelet Entropy Time series of vibration of the carbon fiber rod as sampled by the accelerometer No.1, 3 when exciting the rod at point 13 during the 2^{nd} test.

Wavelet Entropy Time Series of Point 14

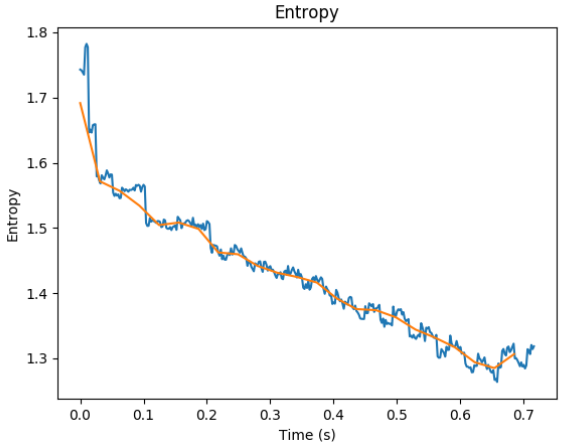

(a) Accelerometer 1

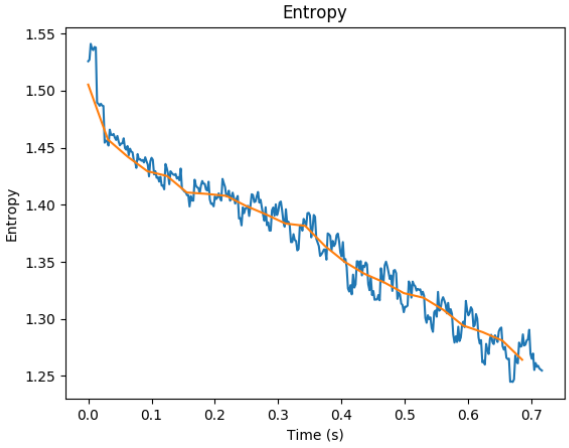

(b) Accelerometer 3

Figure 89: Wavelet Entropy Time series of vibration of the carbon fiber rod as sampled by the accelerometer No.1, 3 when exciting the rod at point 14 during the 1^{st} test.

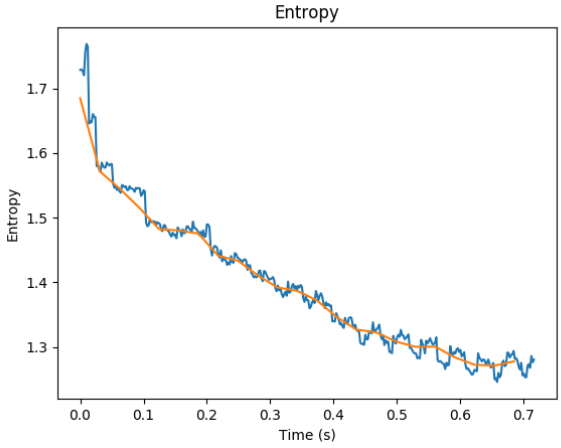

(a) Accelerometer 1

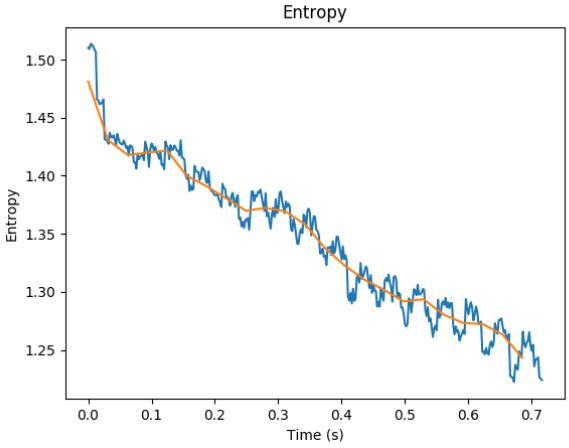

(b) Accelerometer 3

Figure 90: Wavelet Entropy Time series of vibration of the carbon fiber rod as sampled by the accelerometer No.1, 3 when exciting the rod at point 14 during the 2^{nd} test.

Wavelet Entropy Time Series of Point 15

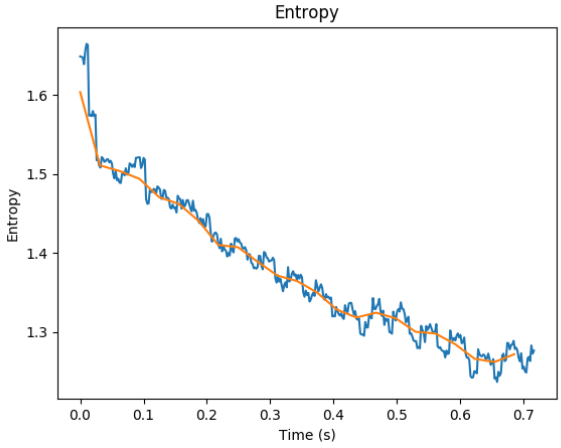

(a) Accelerometer 1

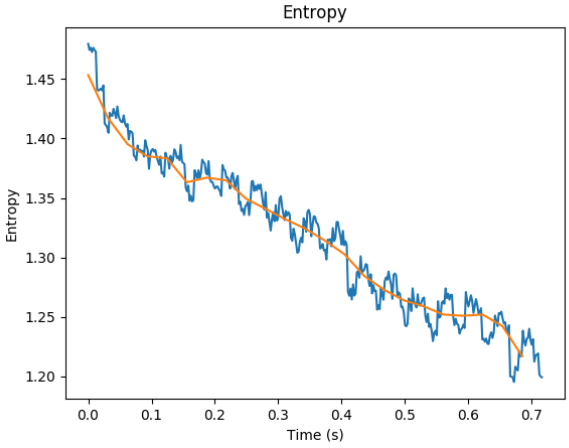

(b) Accelerometer 3

Figure 91: Wavelet Entropy Time series of vibration of the carbon fiber rod as sampled by the accelerometer No.1, 3 when exciting the rod at point 15 during the 1^{st} test.

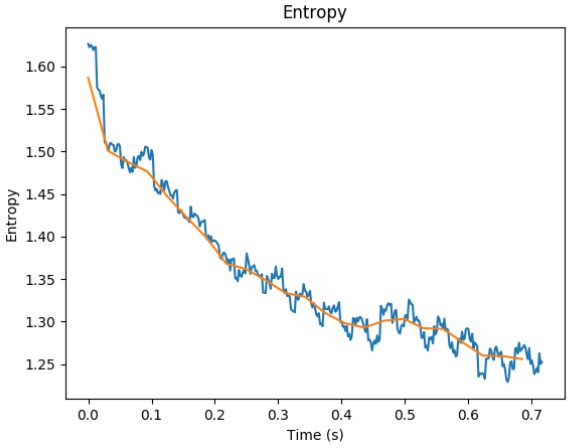

(a) Accelerometer 1

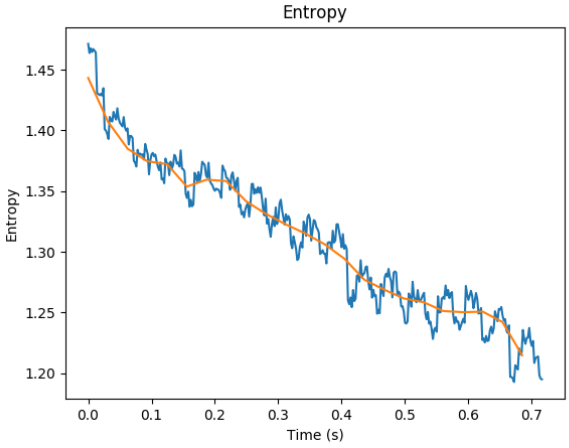

(b) Accelerometer 3

Figure 92: Wavelet Entropy Time series of vibration of the carbon fiber rod as sampled by the accelerometer No.1, 3 when exciting the rod at point 15 during the 2^{nd} test.

Wavelet Entropy Time Series of Point 16

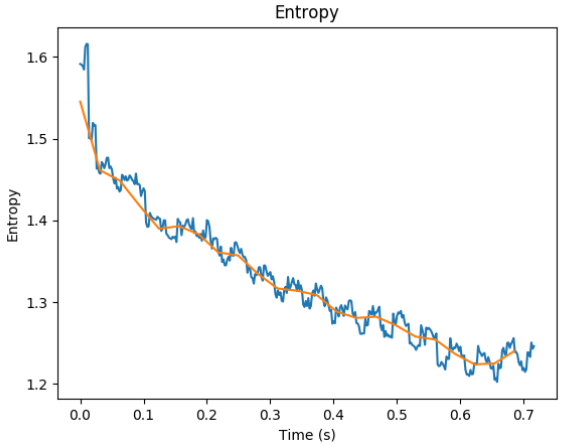

(a) Accelerometer 1

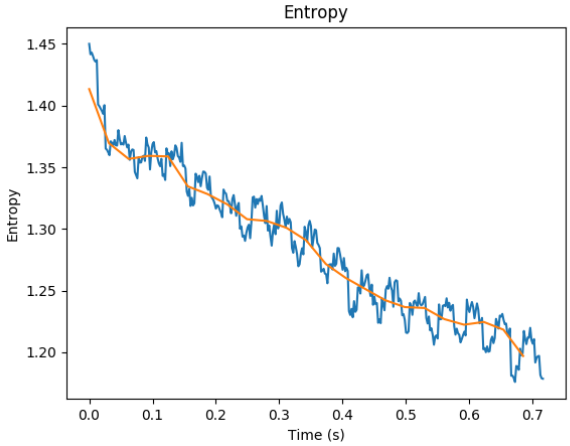

(b) Accelerometer 3

Figure 93: Wavelet Entropy Time series of vibration of the carbon fiber rod as sampled by the accelerometer No.1, 3 when exciting the rod at point 16 during the 1^{st} test.

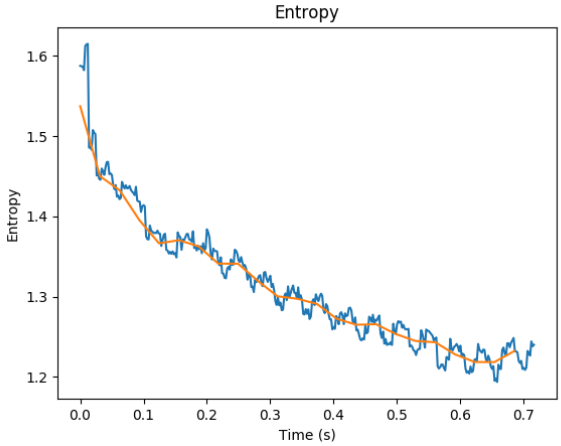

(a) Accelerometer 1

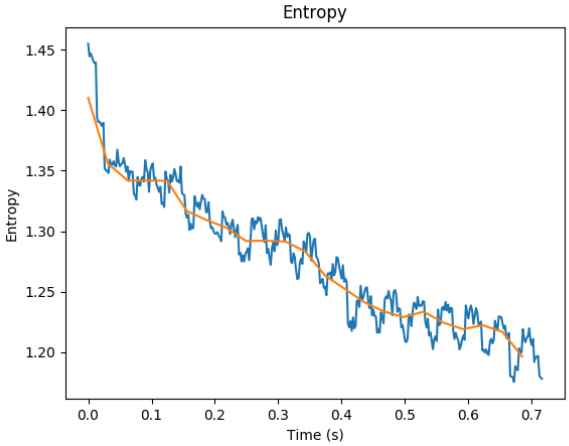

(b) Accelerometer 3

Figure 94: Wavelet Entropy Time series of vibration of the carbon fiber rod as sampled by the accelerometer No.1, 3 when exciting the rod at point 16 during the 2^{nd} test.

Wavelet Entropy Time Series of Point 17

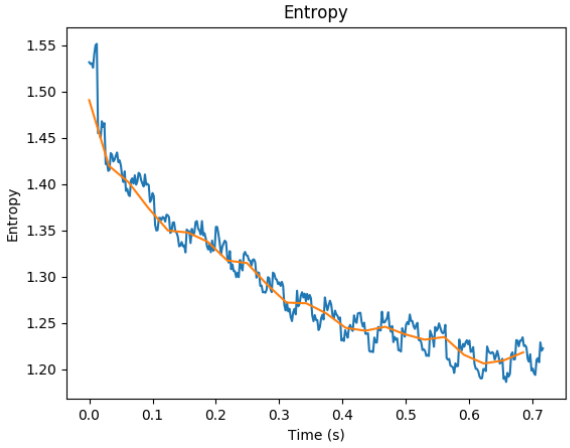

(a) Accelerometer 1

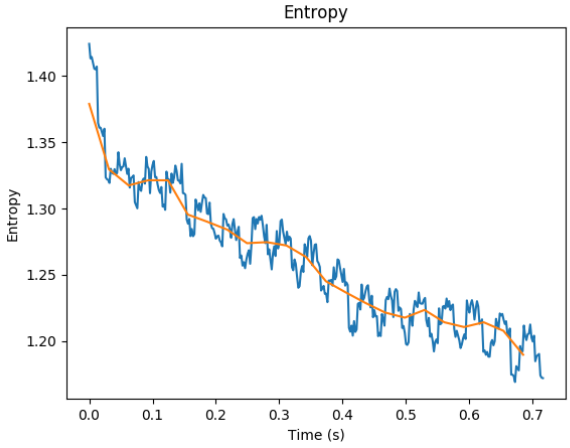

(b) Accelerometer 3

Figure 95: Wavelet Entropy Time series of vibration of the carbon fiber rod as sampled by the accelerometer No.1, 3 when exciting the rod at point 17 during the 1^{st} test.

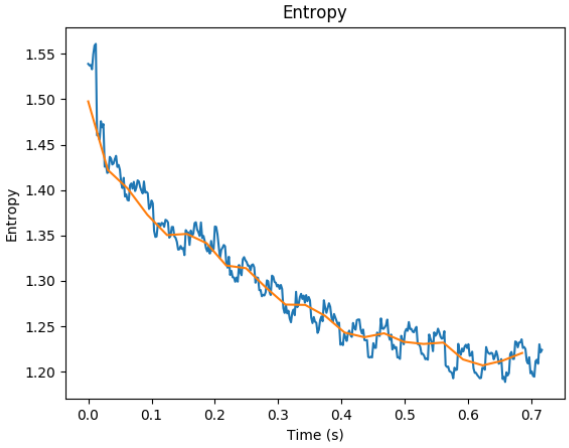

(a) Accelerometer 1

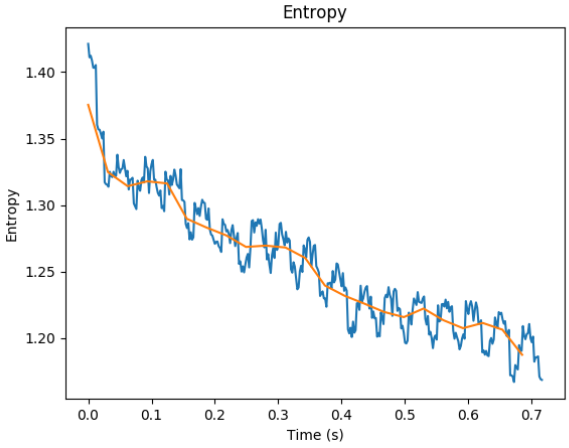

(b) Accelerometer 3

Figure 96: Wavelet Entropy Time series of vibration of the carbon fiber rod as sampled by the accelerometer No.1, 3 when exciting the rod at point 17 during the 2^{nd} test.

Wavelet Entropy Time Series of Point 18

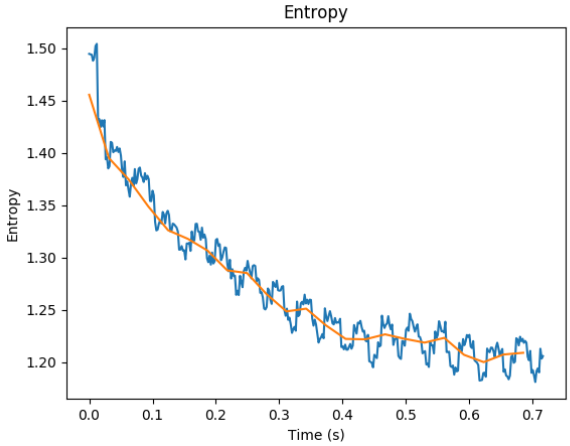

(a) Accelerometer 1

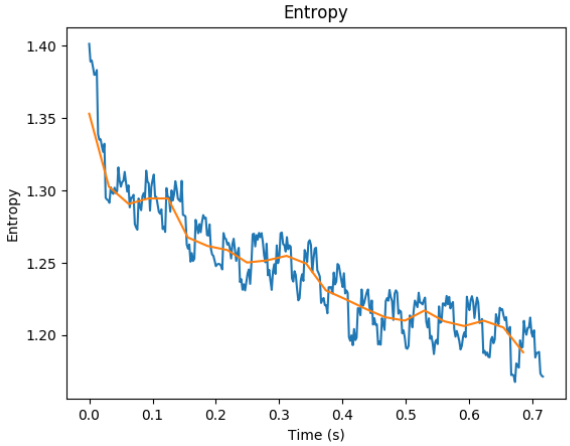

(b) Accelerometer 3

Figure 97: Wavelet Entropy Time series of vibration of the carbon fiber rod as sampled by the accelerometer No.1, 3 when exciting the rod at point 18 during the 1^{st} test.

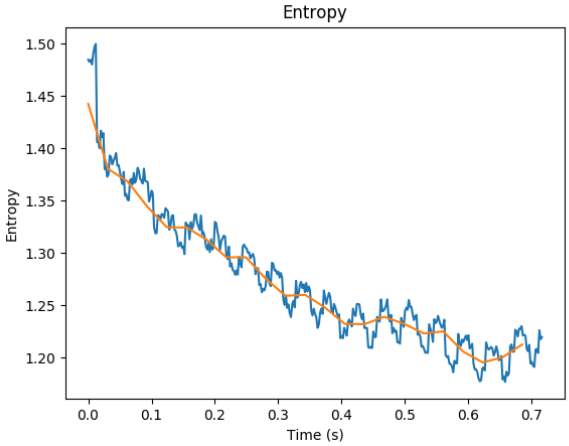

(a) Accelerometer 1

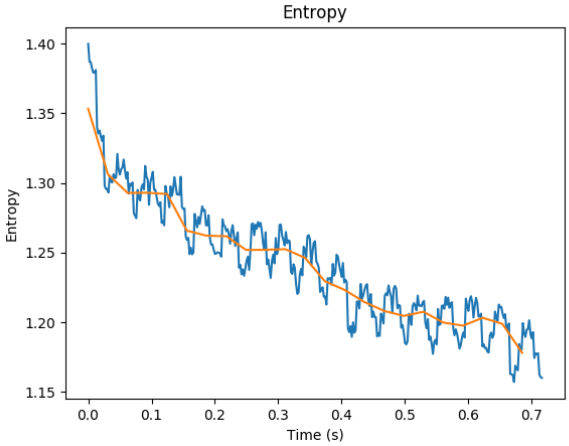

(b) Accelerometer 3

Figure 98: Wavelet Entropy Time series of vibration of the carbon fiber rod as sampled by the accelerometer No.1, 3 when exciting the rod at point 18 during the 2^{nd} test.

Wavelet Entropy Time Series of Point 19

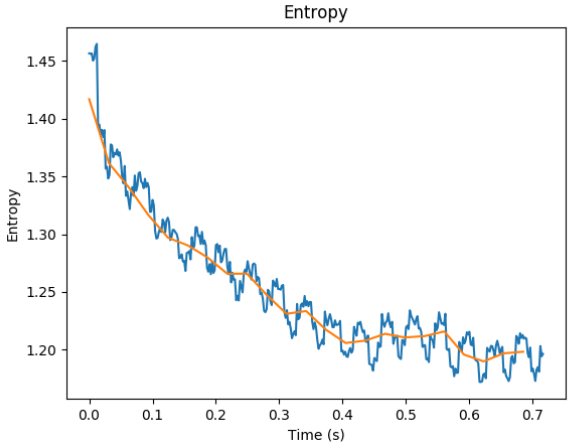

(a) Accelerometer 1

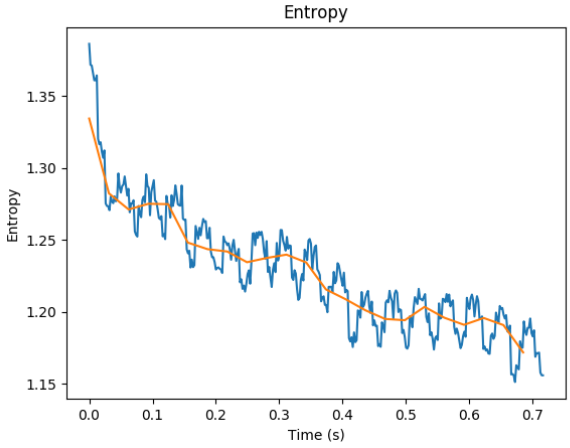

(b) Accelerometer 3

Figure 99: Wavelet Entropy Time series of vibration of the carbon fiber rod as sampled by the accelerometer No.1, 3 when exciting the rod at point 19 during the 1^{st} test.

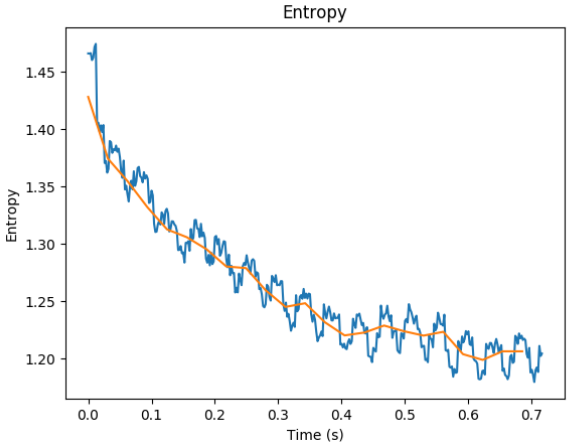

(a) Accelerometer 1

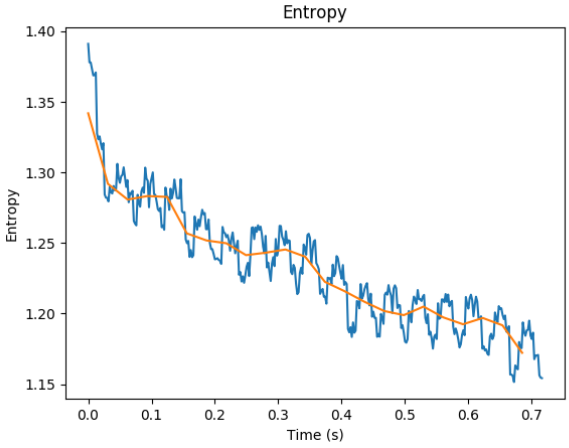

(b) Accelerometer 3

Figure 100: Wavelet Entropy Time series of vibration of the carbon fiber rod as sampled by the accelerometer No.1, 3 when exciting the rod at point 19 during the 2^{nd} test.

Wavelet Entropy Time Series of Point 20

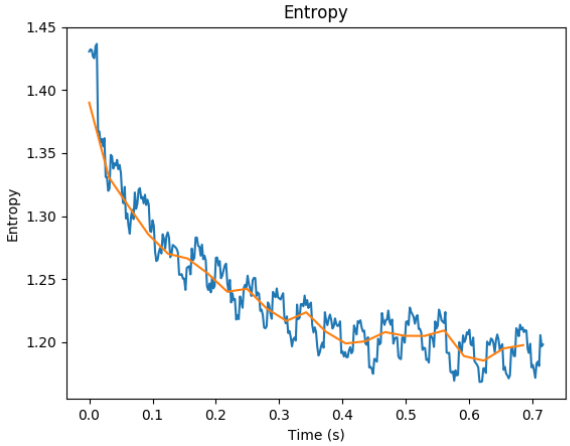

(a) Accelerometer 1

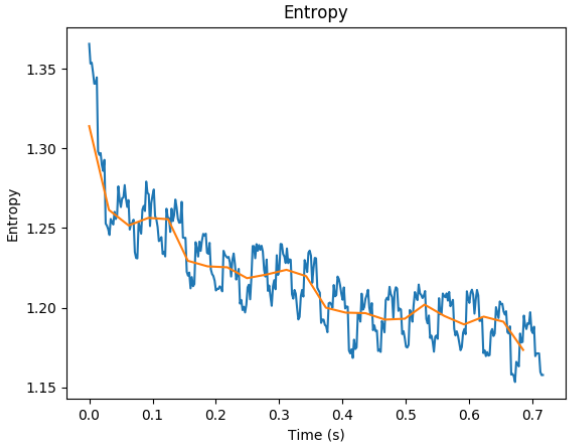

(b) Accelerometer 3

Figure 101: Wavelet Entropy Time series of vibration of the carbon fiber rod as sampled by the accelerometer No.1, 3 when exciting the rod at point 20 during the 1^{st} test.

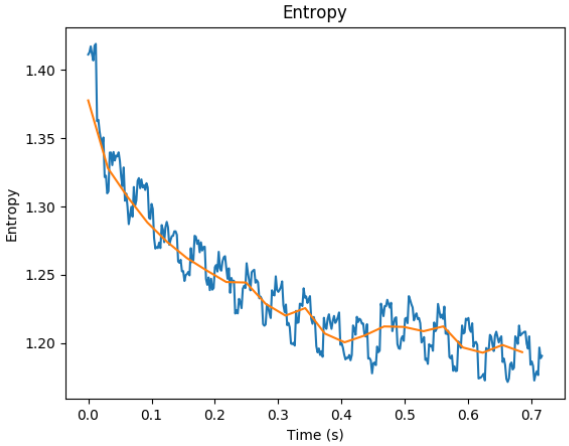

(a) Accelerometer 1

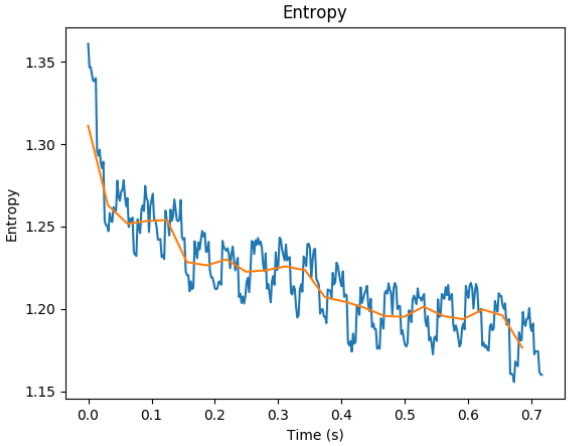

(b) Accelerometer 3

Figure 102: Wavelet Entropy Time series of vibration of the carbon fiber rod as sampled by the accelerometer No.1, 3 when exciting the rod at point 20 during the 2^{nd} test.

Wavelet Entropy Time Series of Point 21

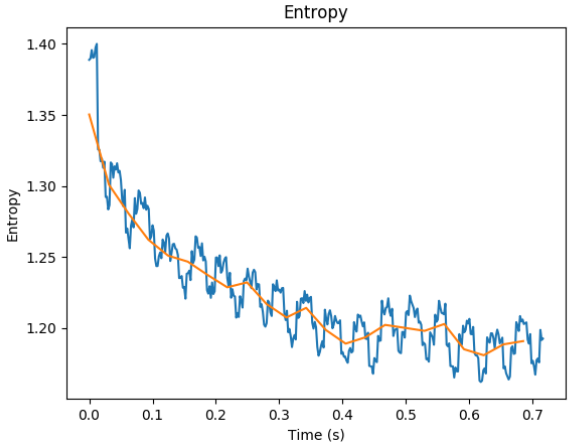

(a) Accelerometer 1

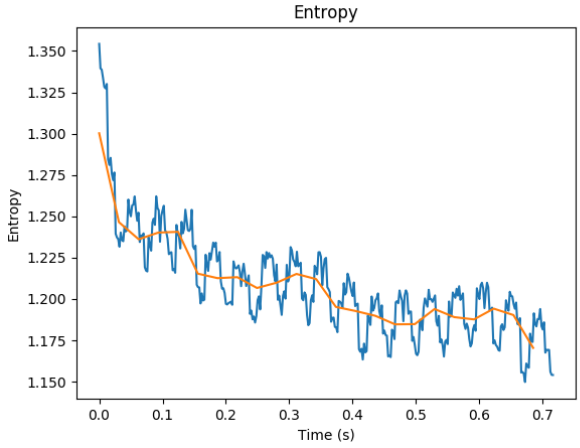

(b) Accelerometer 3

Figure 103: Wavelet Entropy Time series of vibration of the carbon fiber rod as sampled by the accelerometer No.1, 3 when exciting the rod at point 21 during the 1^{st} test.

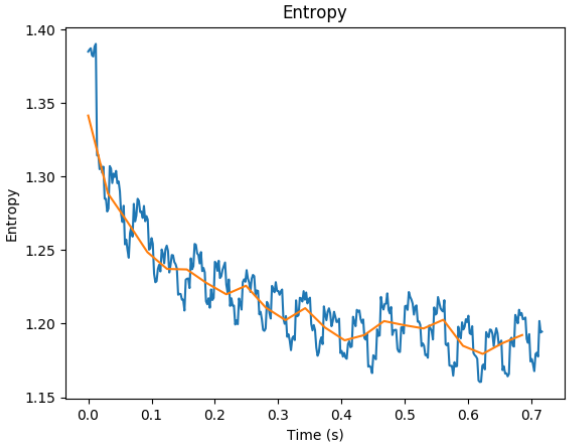

(a) Accelerometer 1

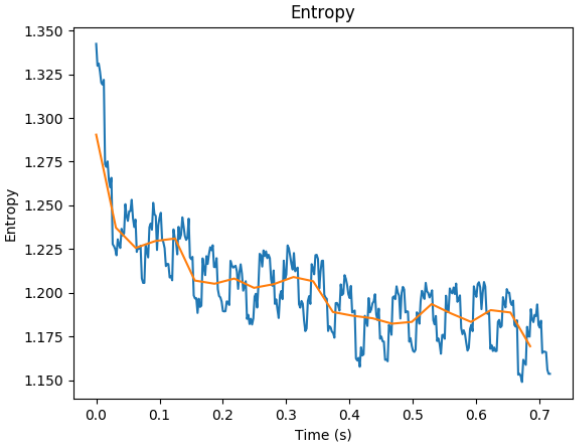

(b) Accelerometer 3

Figure 104: Wavelet Entropy Time series of vibration of the carbon fiber rod as sampled by the accelerometer No.1, 3 when exciting the rod at point 21 during the 2^{nd} test.

Wavelet Entropy Time Series of Point 22

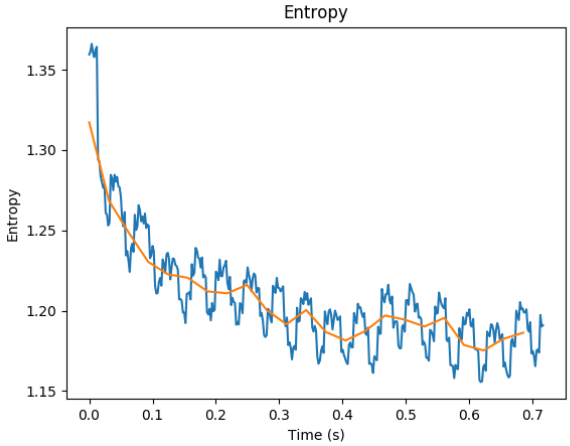

(a) Accelerometer 1

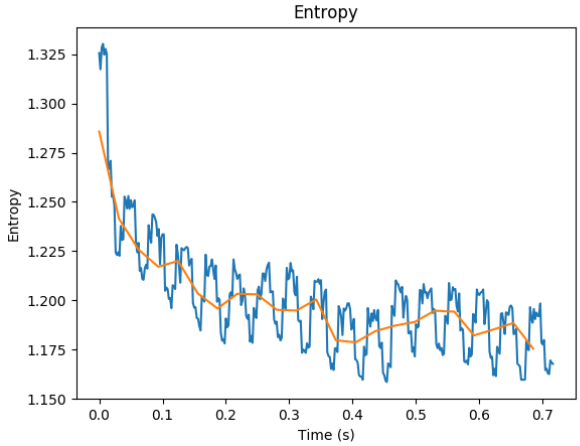

(b) Accelerometer 3

Figure 105: Wavelet Entropy Time series of vibration of the carbon fiber rod as sampled by the accelerometer No.1, 3 when exciting the rod at point 22 during the 1^{st} test.

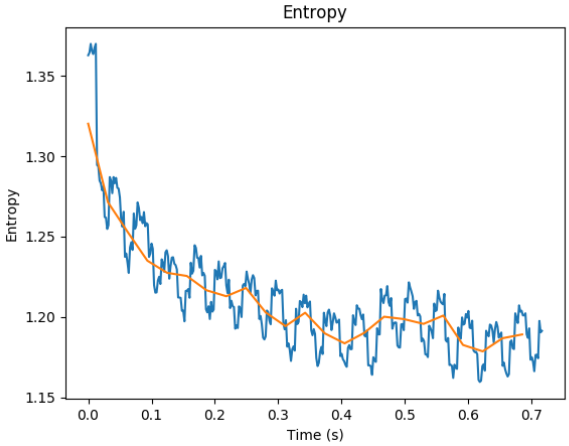

(a) Accelerometer 1

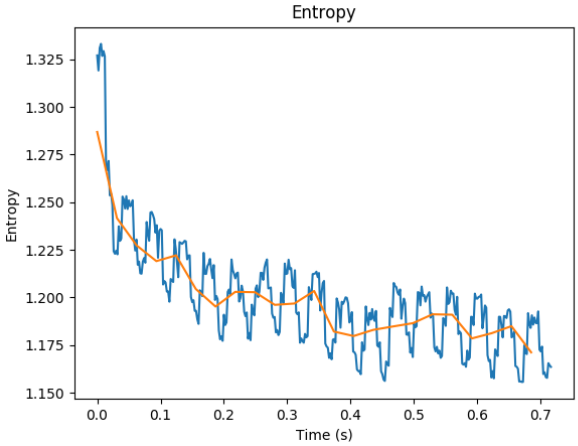

(b) Accelerometer 3

Figure 106: Wavelet Entropy Time series of vibration of the carbon fiber rod as sampled by the accelerometer No.1, 3 when exciting the rod at point 22 during the 2^{nd} test.

Wavelet Entropy Time Series of Point 23

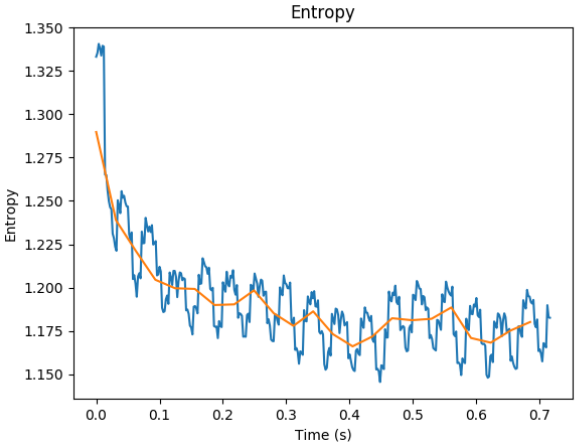

(a) Accelerometer 1

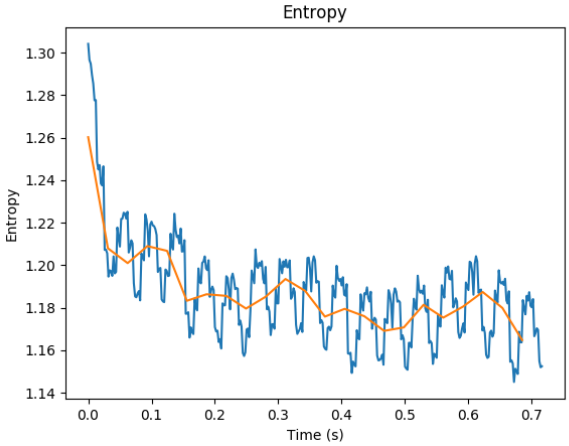

(b) Accelerometer 3

Figure 107: Wavelet Entropy Time series of vibration of the carbon fiber rod as sampled by the accelerometer No.1, 3 when exciting the rod at point 23 during the 1^{st} test.

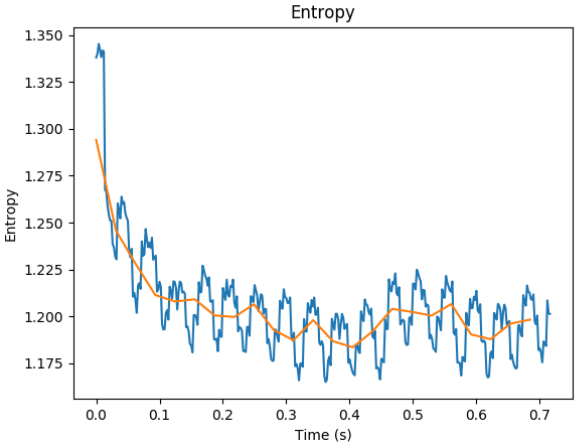

(a) Accelerometer 1

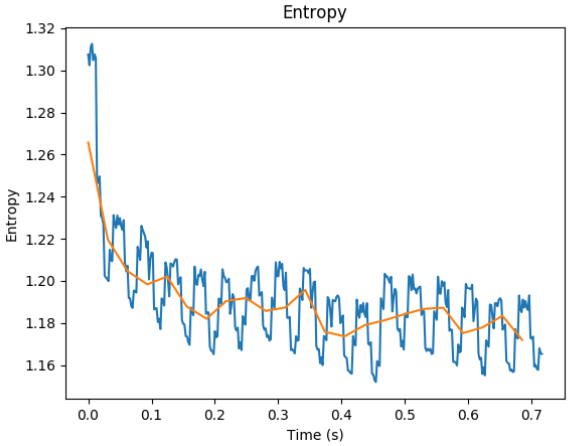

(b) Accelerometer 3

Figure 108: Wavelet Entropy Time series of vibration of the carbon fiber rod as sampled by the accelerometer No.1, 3 when exciting the rod at point 23 during the 2^{nd} test.

Wavelet Entropy Time Series of Point 24

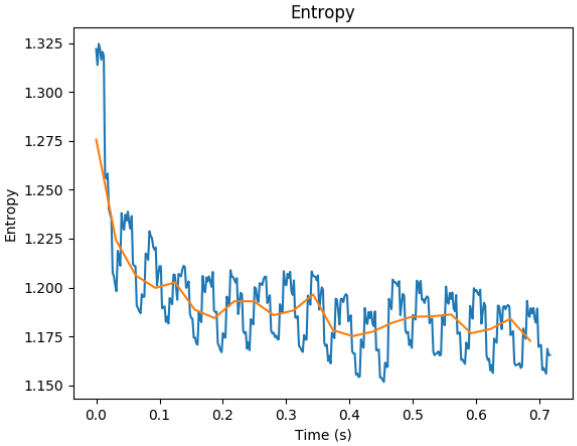

(a) Accelerometer 1

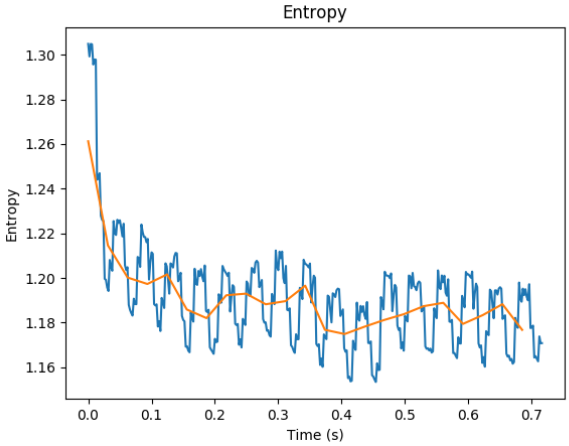

(b) Accelerometer 3

Figure 109: Wavelet Entropy Time series of vibration of the carbon fiber rod as sampled by the accelerometer No.1, 3 when exciting the rod at point 24 during the 1^{st} test.

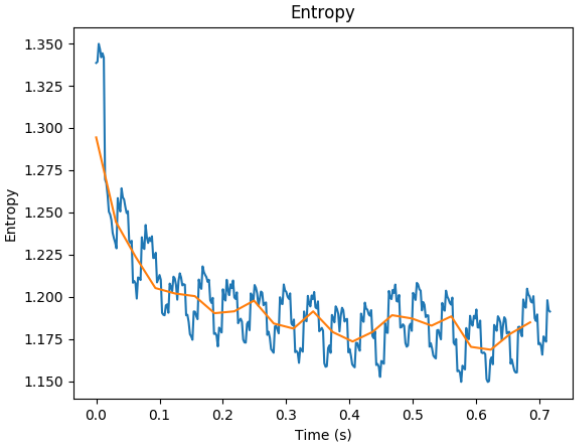

(a) Accelerometer 1

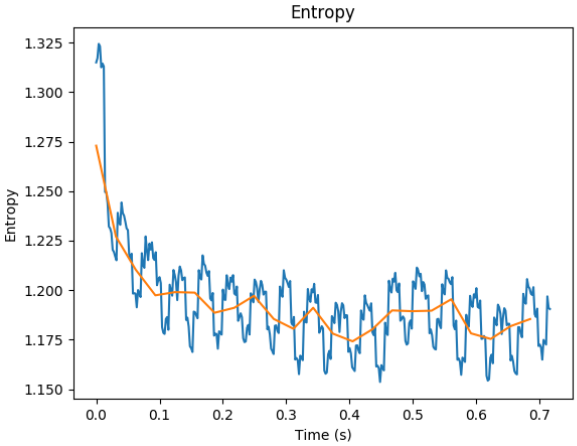

(b) Accelerometer 3

Figure 110: Wavelet Entropy Time series of vibration of the carbon fiber rod as sampled by the accelerometer No.1, 3 when exciting the rod at point 24 during the 2^{nd} test.

Wavelet Entropy Time Series of Point 25

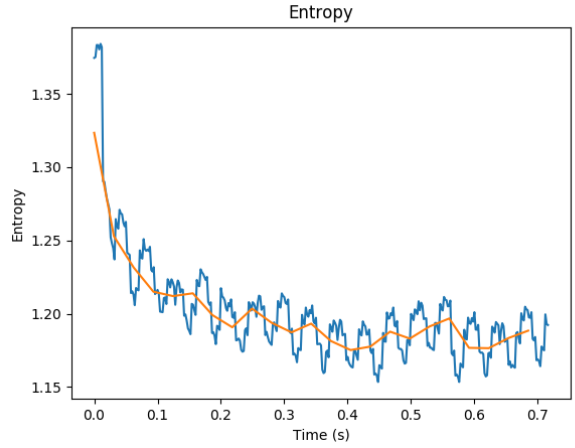

(a) Accelerometer 1

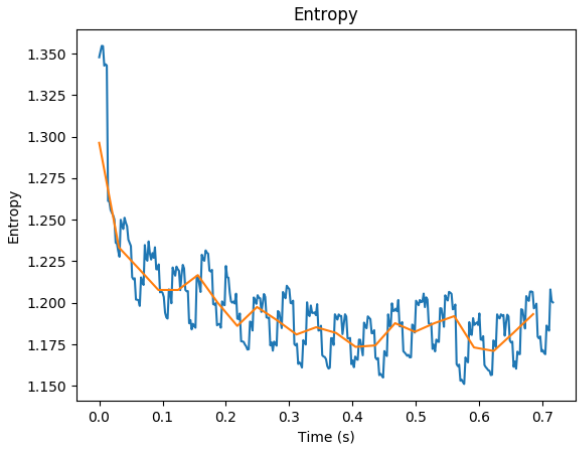

(b) Accelerometer 3

Figure 111: Wavelet Entropy Time series of vibration of the carbon fiber rod as sampled by the accelerometer No.1, 3 when exciting the rod at point 25 during the 1^{st} test.

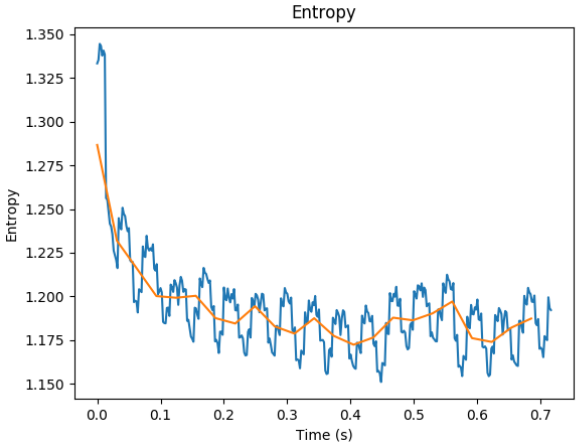

(a) Accelerometer 1

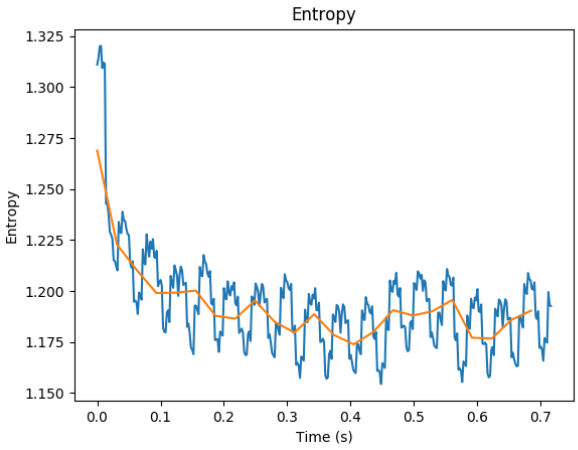

(b) Accelerometer 3

Figure 112: Wavelet Entropy Time series of vibration of the carbon fiber rod as sampled by the accelerometer No.1, 3 when exciting the rod at point 25 during the 2^{nd} test.

Wavelet Entropy Time Series of Point 26

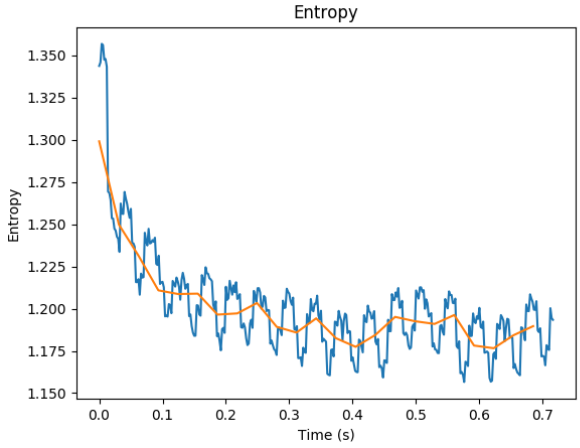

(a) Accelerometer 1

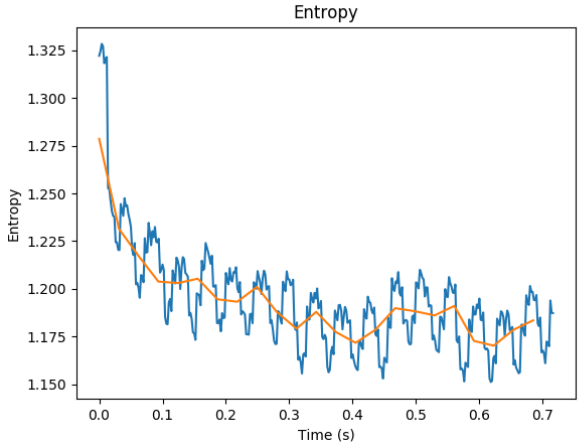

(b) Accelerometer 3

Figure 113: Wavelet Entropy Time series of vibration of the carbon fiber rod as sampled by the accelerometer No.1, 3 when exciting the rod at point 26 during the 1^{st} test.

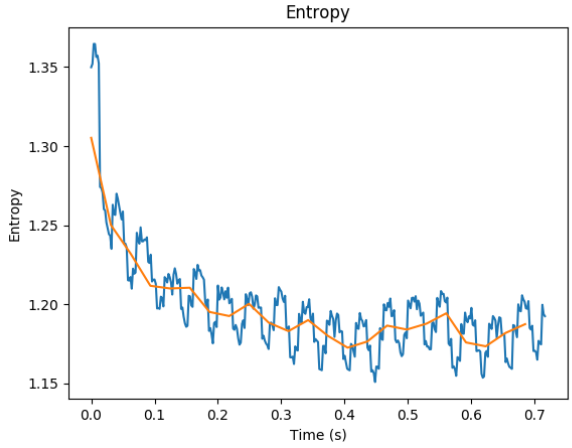

(a) Accelerometer 1

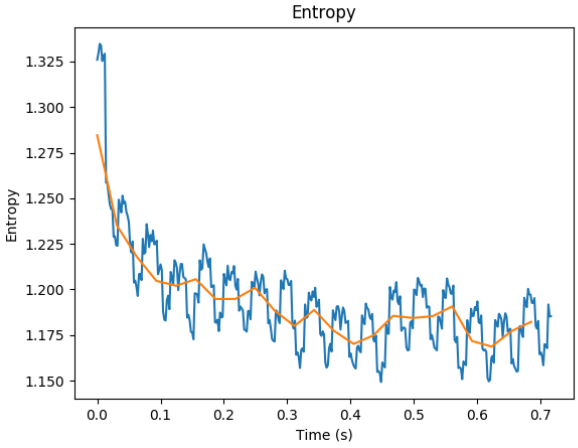

(b) Accelerometer 3

Figure 114: Wavelet Entropy Time series of vibration of the carbon fiber rod as sampled by the accelerometer No.1, 3 when exciting the rod at point 26 during the 2^{nd} test.

Wavelet Entropy Time Series of Point 27

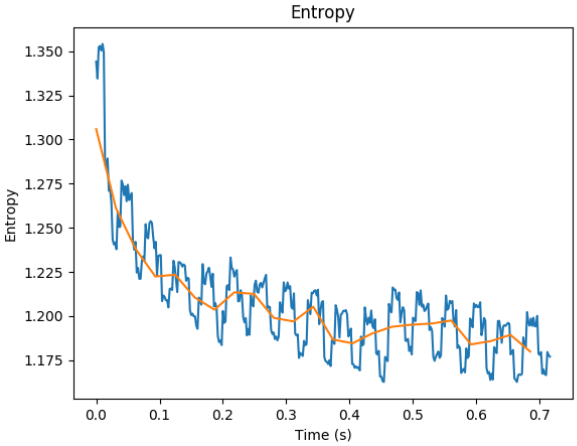

(a) Accelerometer 1

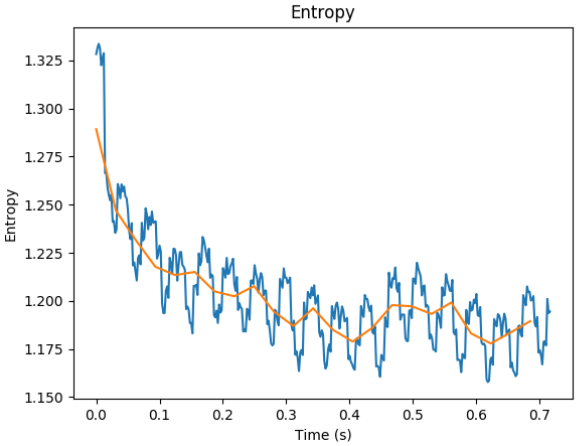

(b) Accelerometer 3

Figure 115: Wavelet Entropy Time series of vibration of the carbon fiber rod as sampled by the accelerometer No.1, 3 when exciting the rod at point 27 during the 1^{st} test.

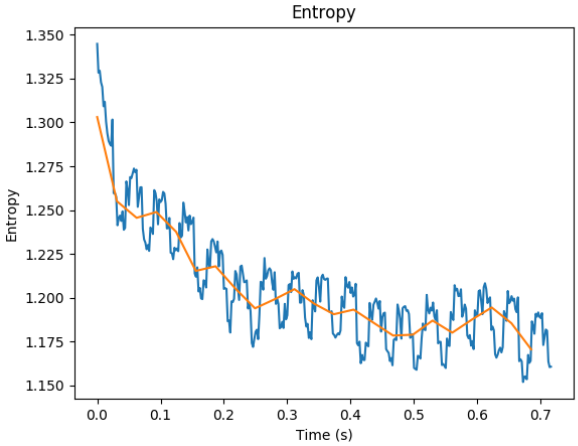

(a) Accelerometer 1

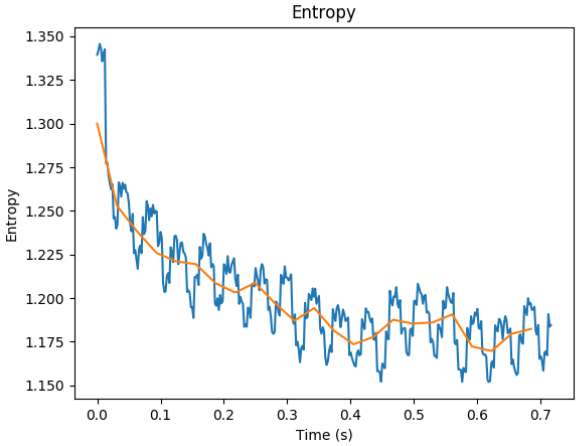

(b) Accelerometer 3

Figure 116: Wavelet Entropy Time series of vibration of the carbon fiber rod as sampled by the accelerometer No.1, 3 when exciting the rod at point 27 during the 2^{nd} test.

Wavelet Entropy Time Series of Point 28

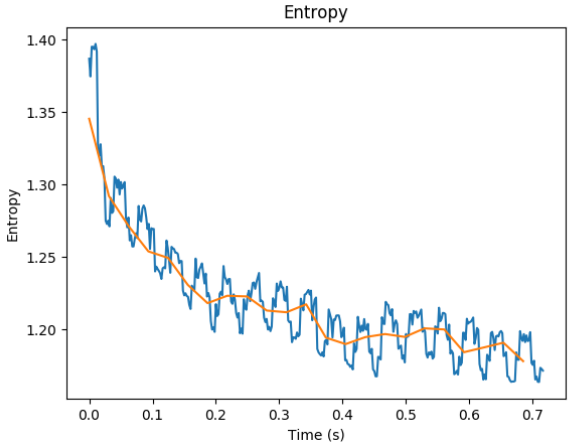

(a) Accelerometer 1

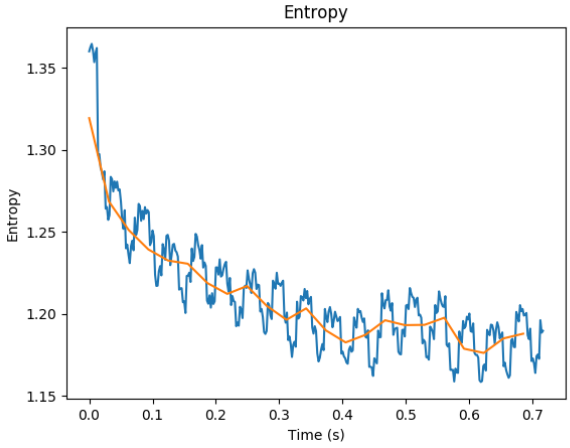

(b) Accelerometer 3

Figure 117: Wavelet Entropy Time series of vibration of the carbon fiber rod as sampled by the accelerometer No.1, 3 when exciting the rod at point 28 during the 1^{st} test.

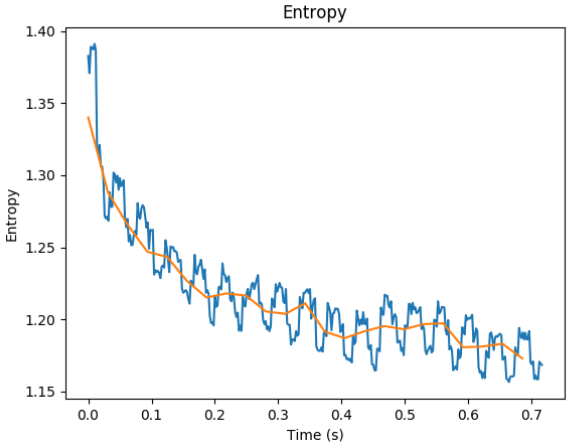

(a) Accelerometer 1

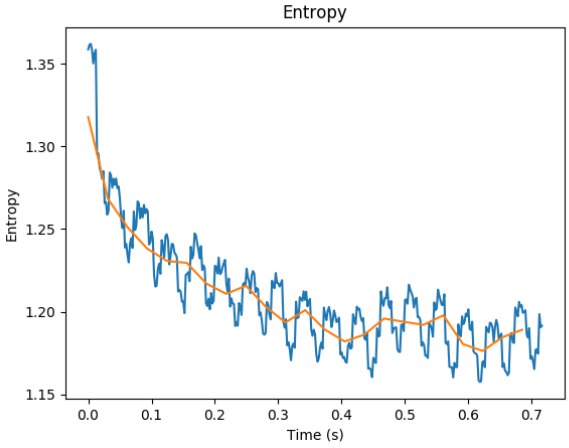

(b) Accelerometer 3

Figure 118: Wavelet Entropy Time series of vibration of the carbon fiber rod as sampled by the accelerometer No.1, 3 when exciting the rod at point 28 during the 2^{nd} test.

Wavelet Entropy Time Series of Point 29

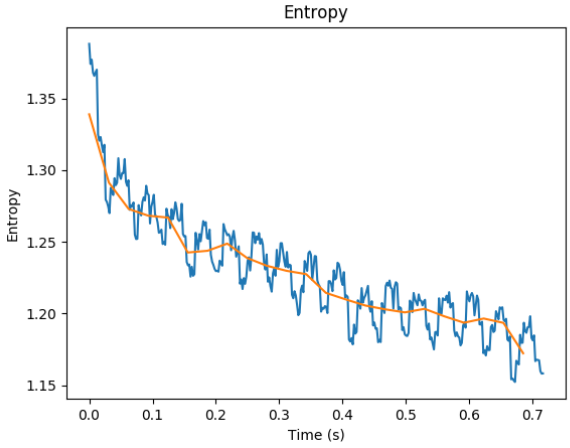

(a) Accelerometer 1

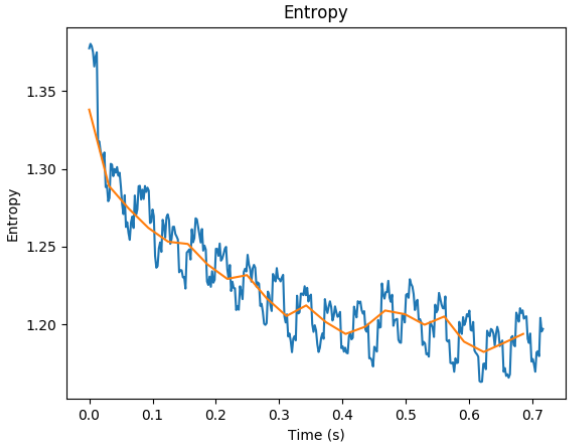

(b) Accelerometer 3

Figure 119: Wavelet Entropy Time series of vibration of the carbon fiber rod as sampled by the accelerometer No.1, 3 when exciting the rod at point 29 during the 1^{st} test.

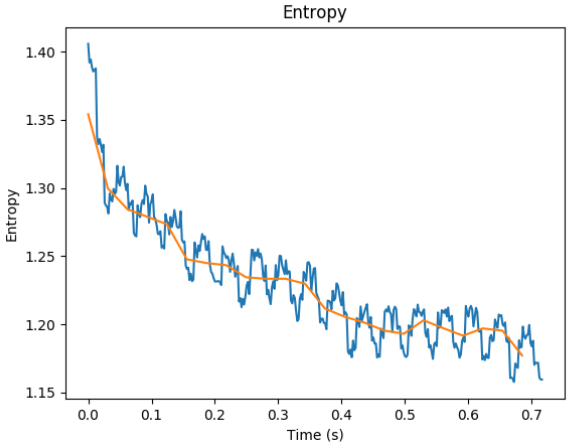

(a) Accelerometer 1

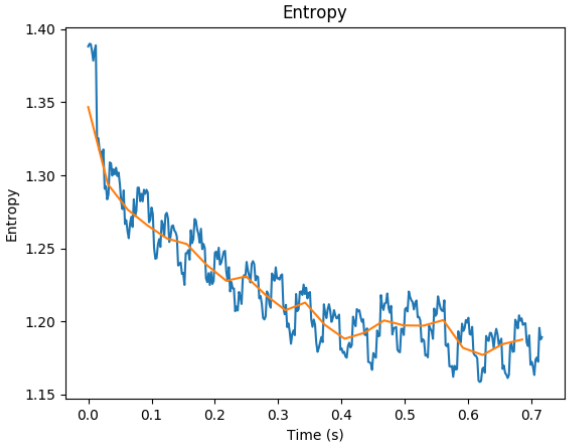

(b) Accelerometer 3

Figure 120: Wavelet Entropy Time series of vibration of the carbon fiber rod as sampled by the accelerometer No.1, 3 when exciting the rod at point 29 during the 2^{nd} test.

Wavelet Entropy Time Series of Point 30

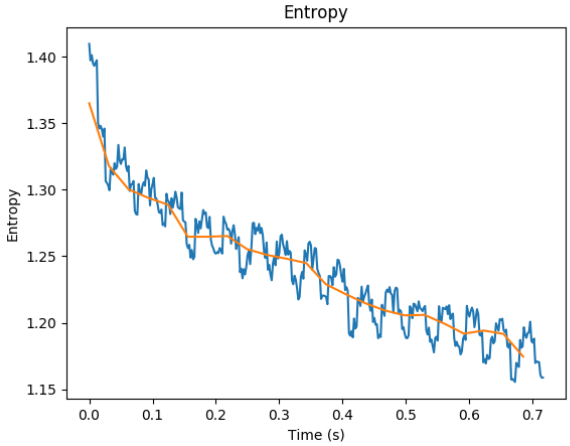

(a) Accelerometer 1

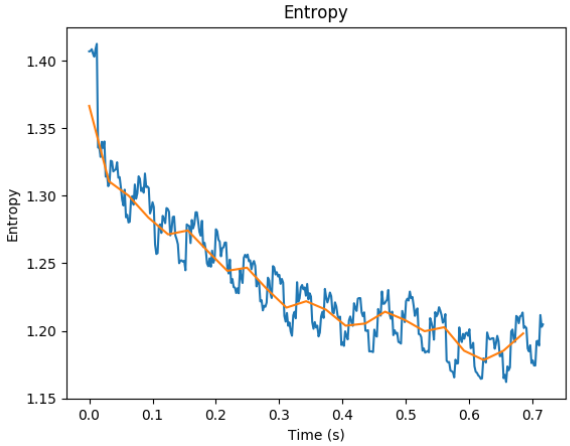

(b) Accelerometer 3

Figure 121: Wavelet Entropy Time series of vibration of the carbon fiber rod as sampled by the accelerometer No.1, 3 when exciting the rod at point 30 during the 1^{st} test.

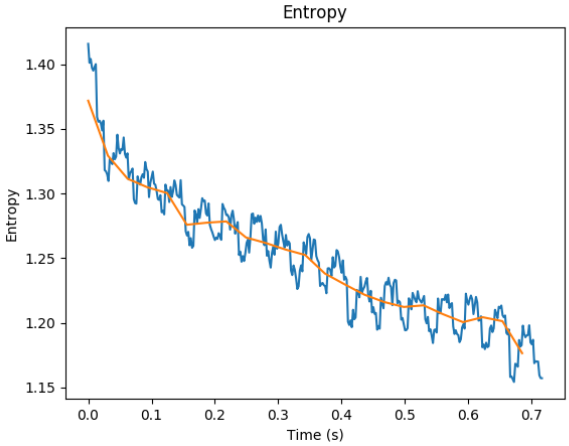

(a) Accelerometer 1

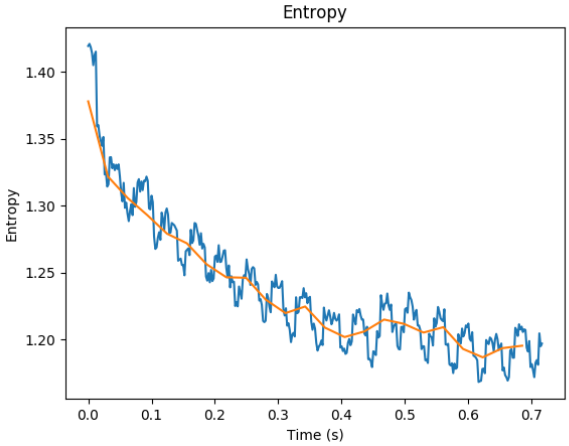

(b) Accelerometer 3

Figure 122: Wavelet Entropy Time series of vibration of the carbon fiber rod as sampled by the accelerometer No.1, 3 when exciting the rod at point 30 during the 2^{nd} test.

Wavelet Entropy Time Series of Point 31

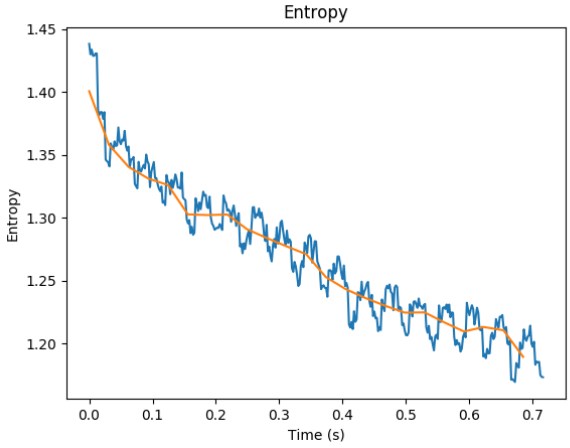

(a) Accelerometer 1

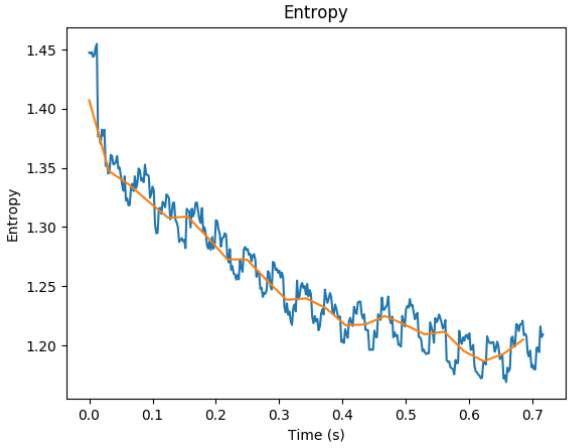

(b) Accelerometer 3

Figure 123: Wavelet Entropy Time series of vibration of the carbon fiber rod as sampled by the accelerometer No.1, 3 when exciting the rod at point 31 during the 1^{st} test.

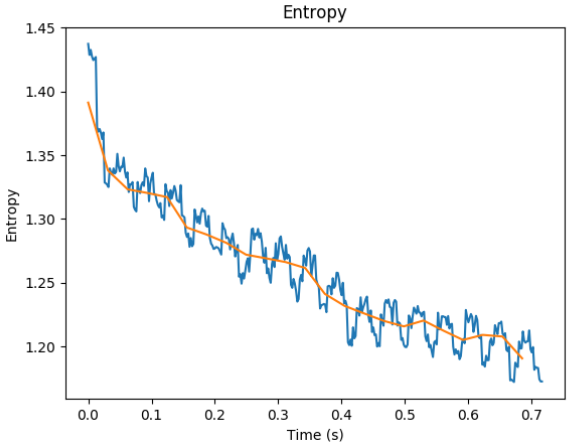

(a) Accelerometer 1

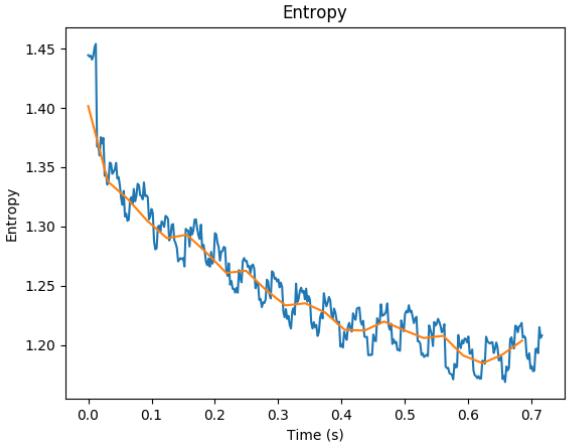

(b) Accelerometer 3

Figure 124: Wavelet Entropy Time series of vibration of the carbon fiber rod as sampled by the accelerometer No.1, 3 when exciting the rod at point 31 during the 2^{nd} test.

Wavelet Entropy Time Series of Point 32

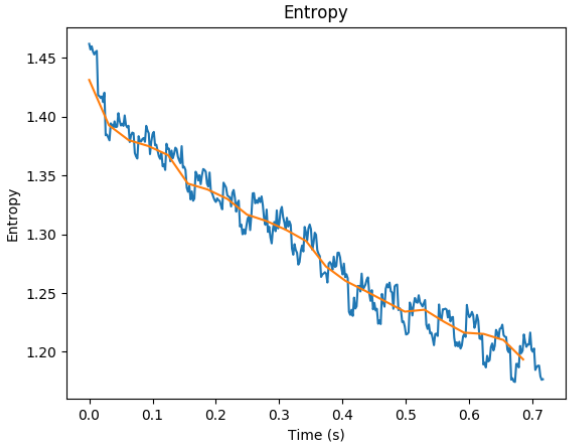

(a) Accelerometer 1

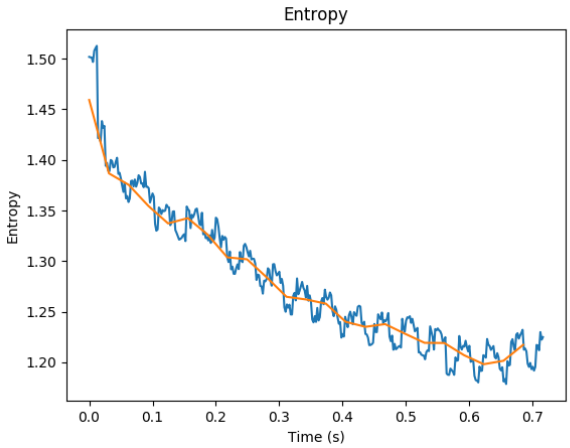

(b) Accelerometer 3

Figure 125: Wavelet Entropy Time series of vibration of the carbon fiber rod as sampled by the accelerometer No.1, 3 when exciting the rod at point 32 during the 1^{st} test.

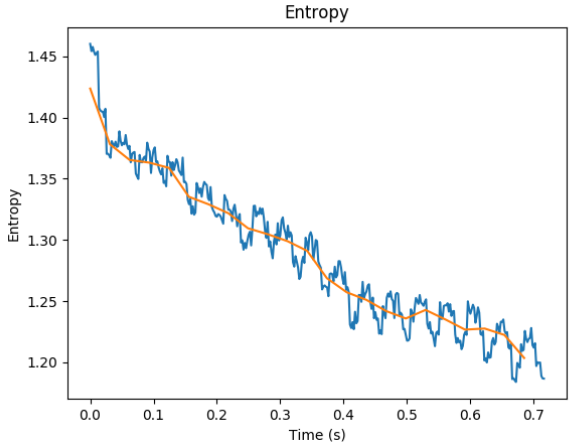

(a) Accelerometer 1

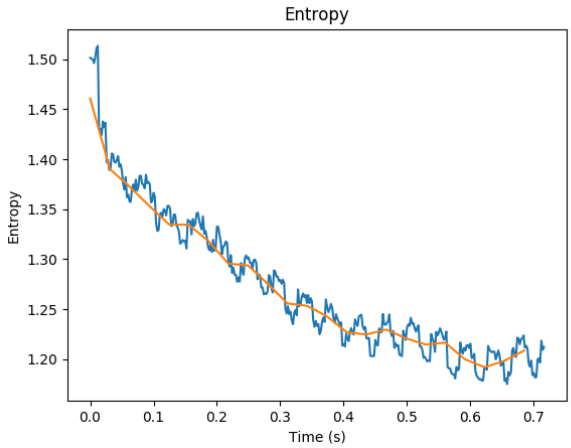

(b) Accelerometer 3

Figure 126: Wavelet Entropy Time series of vibration of the carbon fiber rod as sampled by the accelerometer No.1, 3 when exciting the rod at point 32 during the 2^{nd} test.

Wavelet Entropy Time Series of Point 33

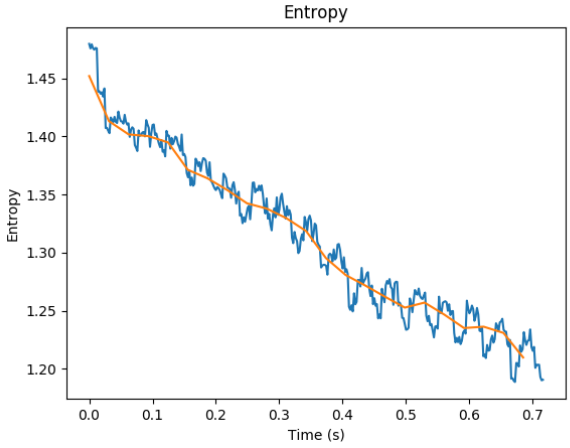

(a) Accelerometer 1

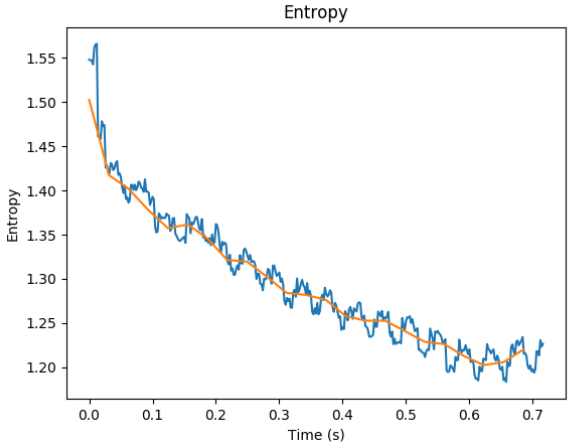

(b) Accelerometer 3

Figure 127: Wavelet Entropy Time series of vibration of the carbon fiber rod as sampled by the accelerometer No.1, 3 when exciting the rod at point 33 during the 1^{st} test.

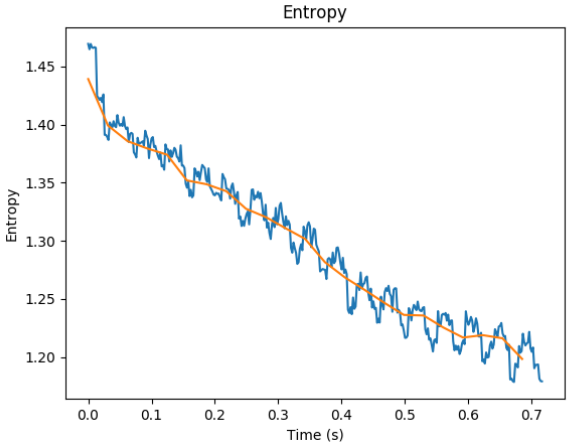

(a) Accelerometer 1

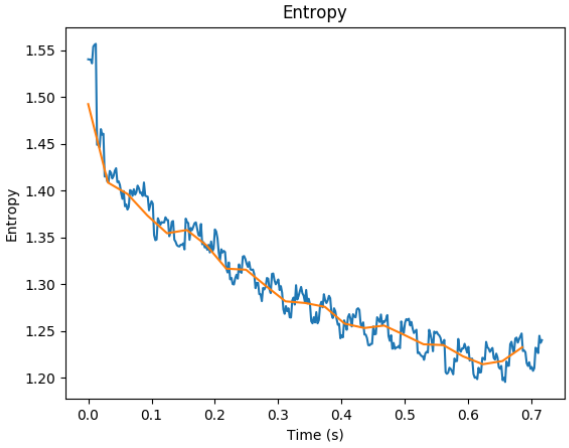

(b) Accelerometer 3

Figure 128: Wavelet Entropy Time series of vibration of the carbon fiber rod as sampled by the accelerometer No.1, 3 when exciting the rod at point 33 during the 2^{nd} test.

Wavelet Entropy Time Series of Point 34

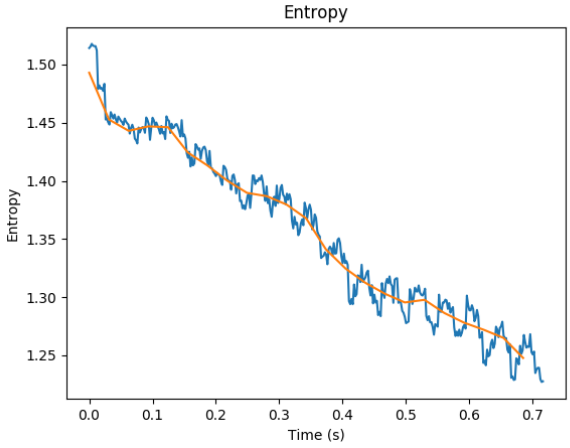

(a) Accelerometer 1

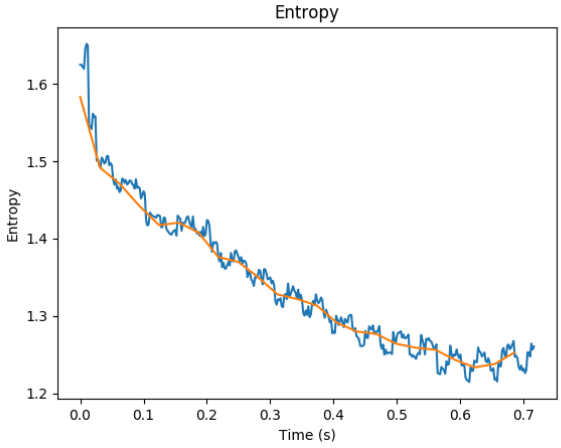

(b) Accelerometer 3

Figure 129: Wavelet Entropy Time series of vibration of the carbon fiber rod as sampled by the accelerometer No.1, 3 when exciting the rod at point 34 during the 1^{st} test.

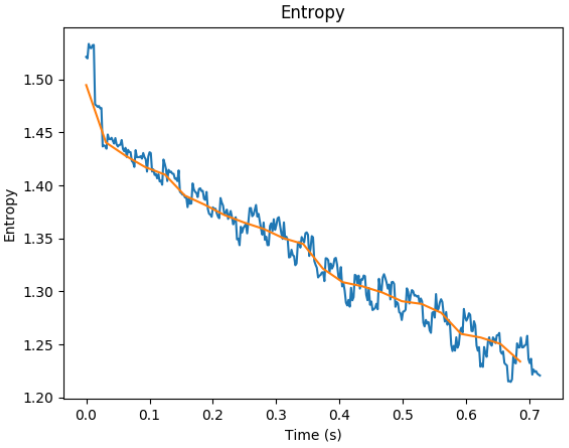

(a) Accelerometer 1

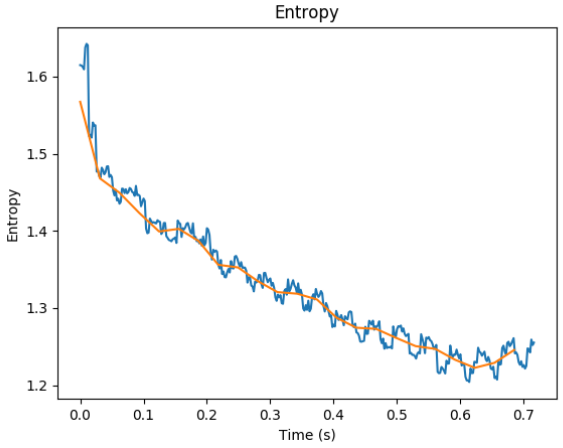

(b) Accelerometer 3

Figure 130: Wavelet Entropy Time series of vibration of the carbon fiber rod as sampled by the accelerometer No.1, 3 when exciting the rod at point 34 during the 2^{nd} test.

Wavelet Entropy Time Series of Point 35

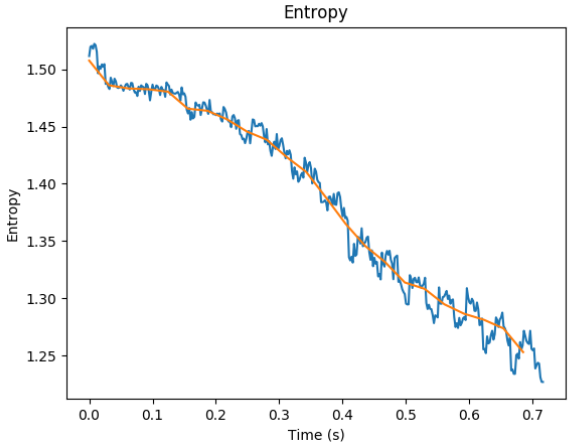

(a) Accelerometer 1

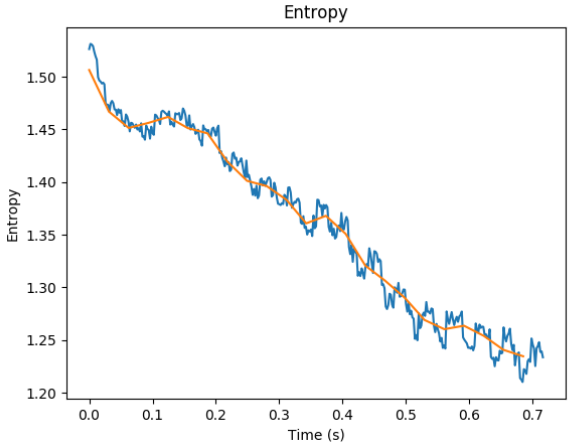

(b) Accelerometer 3

Figure 131: Wavelet Entropy Time series of vibration of the carbon fiber rod as sampled by the accelerometer No.1, 3 when exciting the rod at point 35 during the 1^{st} test.

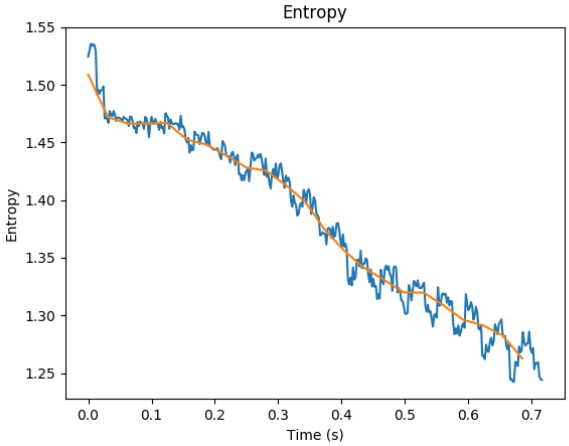

(a) Accelerometer 1

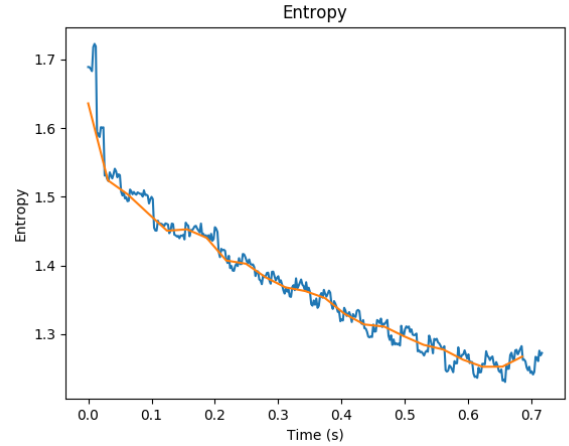

(b) Accelerometer 3

Figure 132: Wavelet Entropy Time series of vibration of the carbon fiber rod as sampled by the accelerometer No.1, 3 when exciting the rod at point 35 during the 2^{nd} test.

Wavelet Entropy Time Series of Point 36

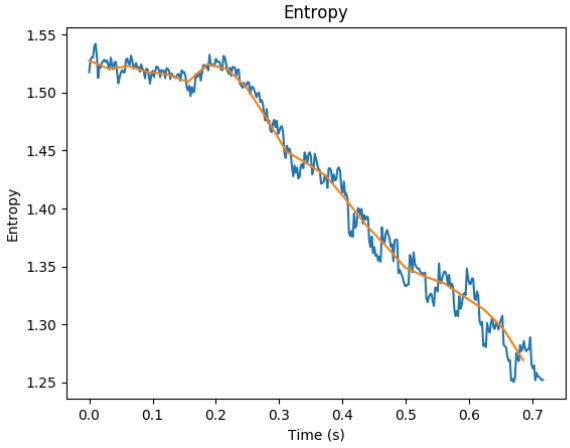

(a) Accelerometer 1

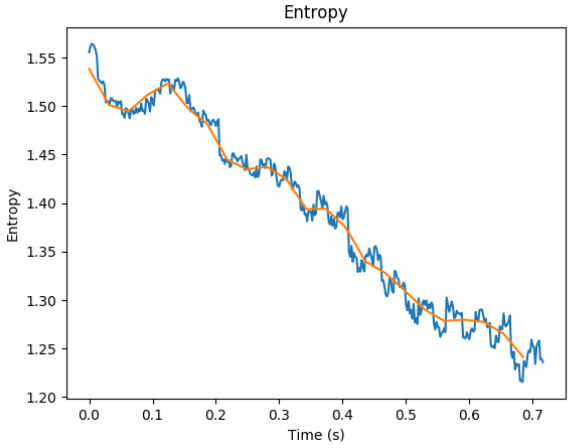

(b) Accelerometer 3

Figure 133: Wavelet Entropy Time series of vibration of the carbon fiber rod as sampled by the accelerometer No.1, 3 when exciting the rod at point 36 during the 1^{st} test.

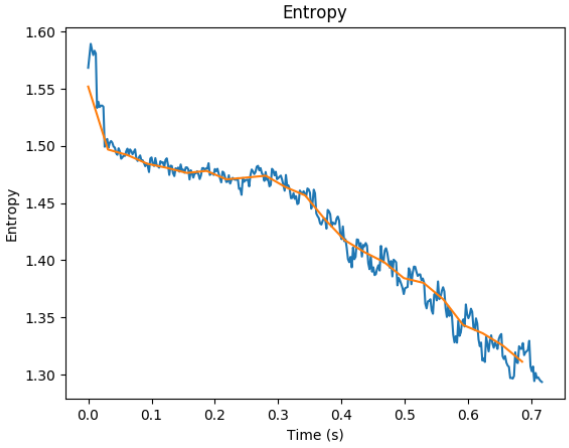

(a) Accelerometer 1

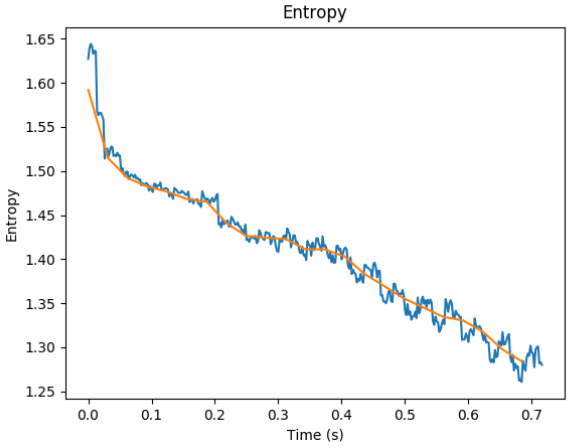

(b) Accelerometer 3

Figure 134: Wavelet Entropy Time series of vibration of the carbon fiber rod as sampled by the accelerometer No.1, 3 when exciting the rod at point 36 during the 2^{nd} test.

Wavelet Entropy Time Series of Point 37

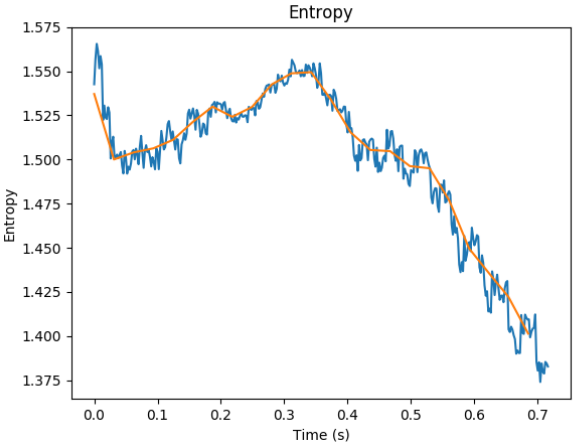

(a) Accelerometer 1

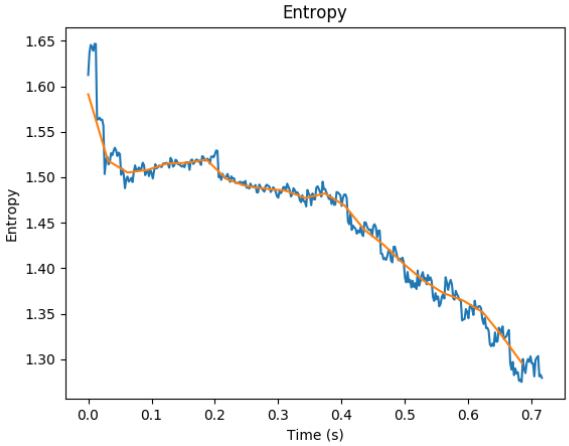

(b) Accelerometer 3

Figure 135: Wavelet Entropy Time series of vibration of the carbon fiber rod as sampled by the accelerometer No.1, 3 when exciting the rod at point 37 during the 1^{st} test.

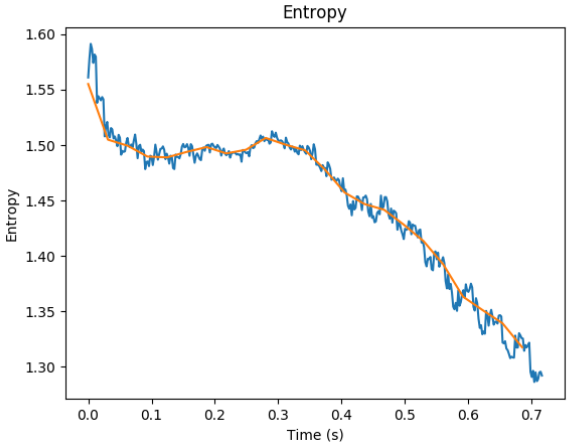

(a) Accelerometer 1

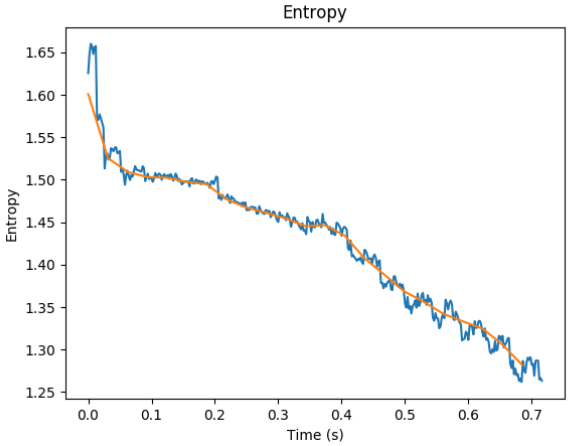

(b) Accelerometer 3

Figure 136: Wavelet Entropy Time series of vibration of the carbon fiber rod as sampled by the accelerometer No.1, 3 when exciting the rod at point 37 during the 2^{nd} test.

Wavelet Entropy Time Series of Point 38

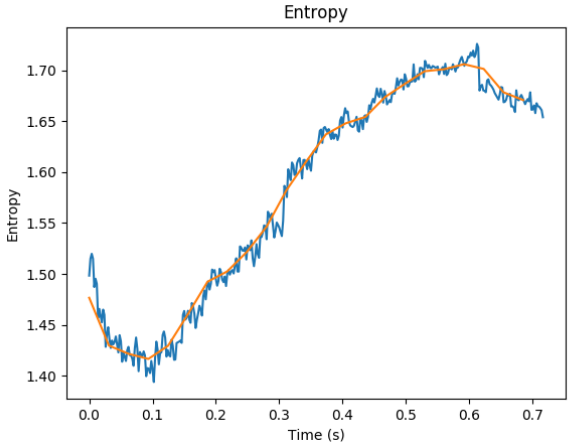

(a) Accelerometer 1

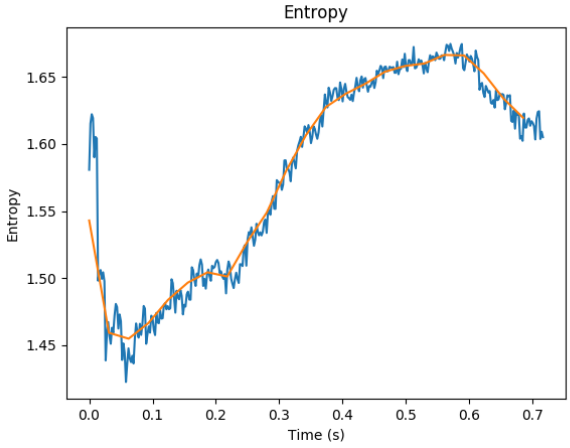

(b) Accelerometer 3

Figure 137: Wavelet Entropy Time series of vibration of the carbon fiber rod as sampled by the accelerometer No.1, 3 when exciting the rod at point 38 during the 1^{st} test.

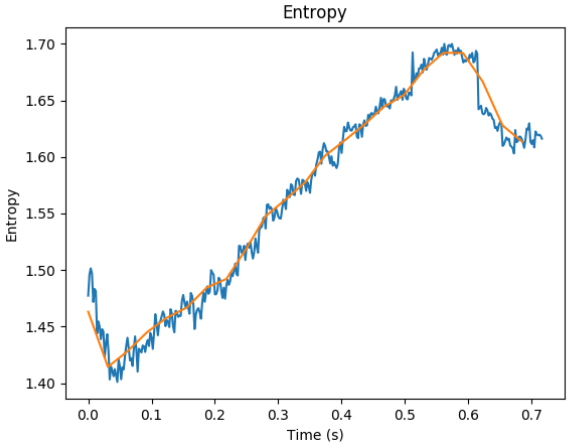

(a) Accelerometer 1

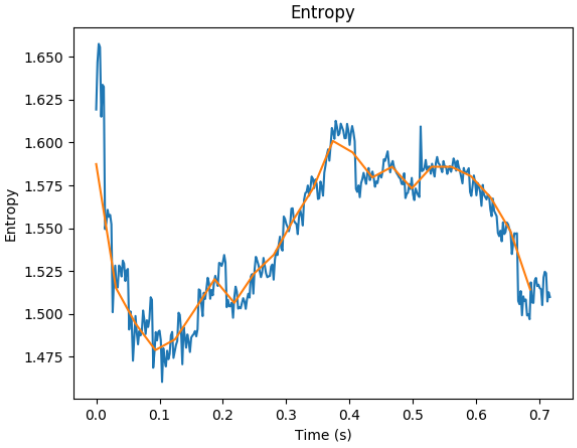

(b) Accelerometer 3

Figure 138: Wavelet Entropy Time series of vibration of the carbon fiber rod as sampled by the accelerometer No.1, 3 when exciting the rod at point 38 during the 2^{nd} test.

Wavelet Entropy Time Series of Point 39

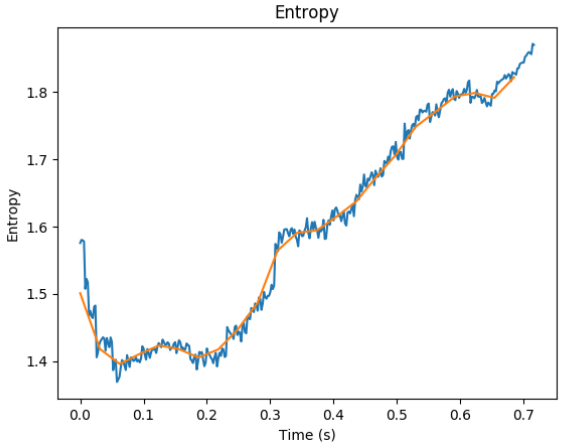

(a) Accelerometer 1

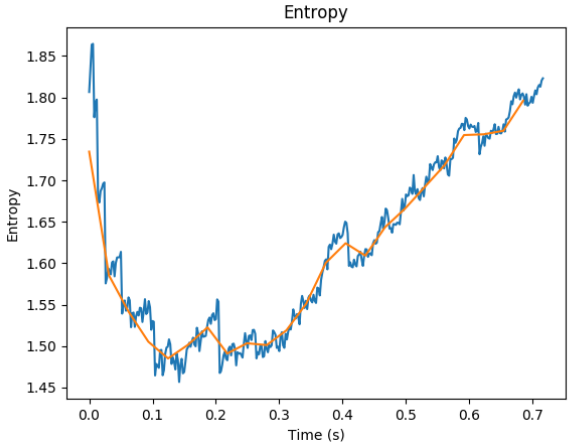

(b) Accelerometer 3

Figure 139: Wavelet Entropy Time series of vibration of the carbon fiber rod as sampled by the accelerometer No.1, 3 when exciting the rod at point 39 during the 1^{st} test.

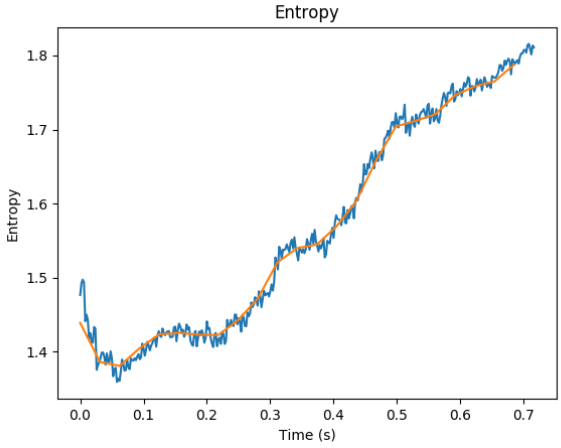

(a) Accelerometer 1

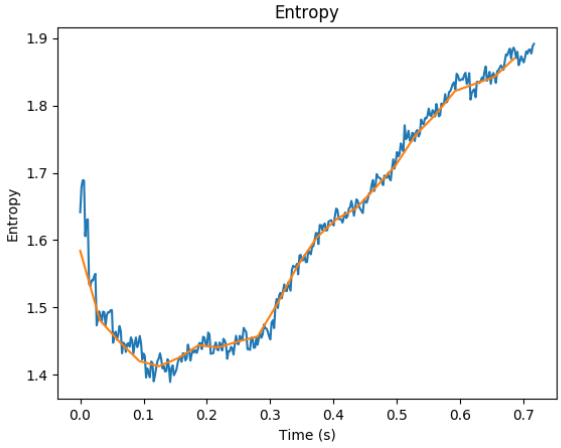

(b) Accelerometer 3

Figure 140: Wavelet Entropy Time series of vibration of the carbon fiber rod as sampled by the accelerometer No.1, 3 when exciting the rod at point 39 during the 2^{nd} test.

Wavelet Entropy Time Series of Point 40

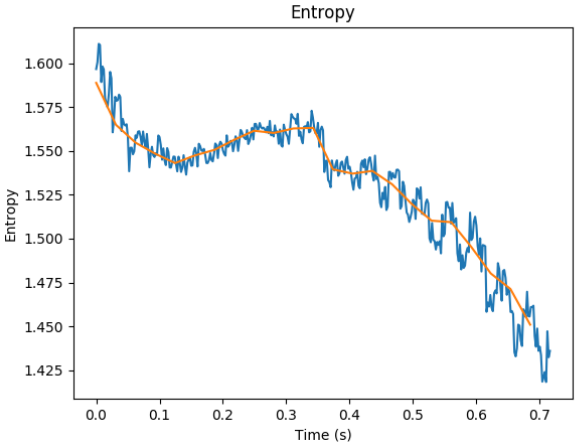

(a) Accelerometer 1

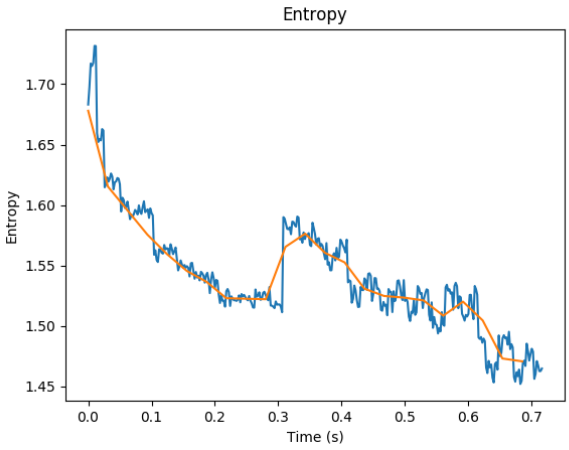

(b) Accelerometer 3

Figure 141: Wavelet Entropy Time series of vibration of the carbon fiber rod as sampled by the accelerometer No.1, 3 when exciting the rod at point 40 during the 1^{st} test.

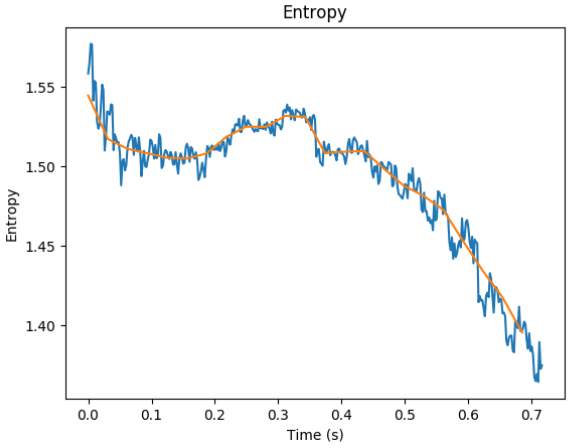

(a) Accelerometer 1

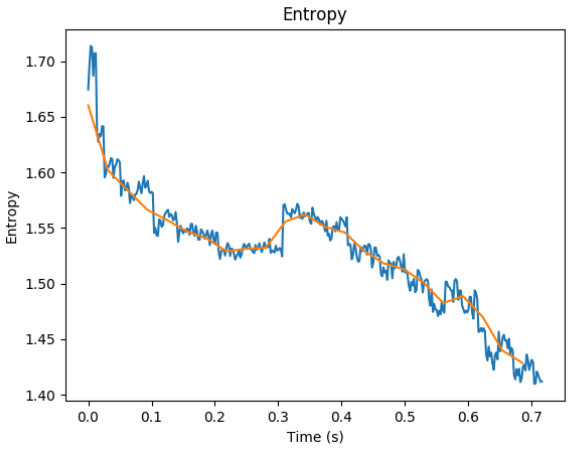

(b) Accelerometer 3

Figure 142: Wavelet Entropy Time series of vibration of the carbon fiber rod as sampled by the accelerometer No.1, 3 when exciting the rod at point 40 during the 2^{nd} test.

Wavelet Entropy Time Series of Point 41

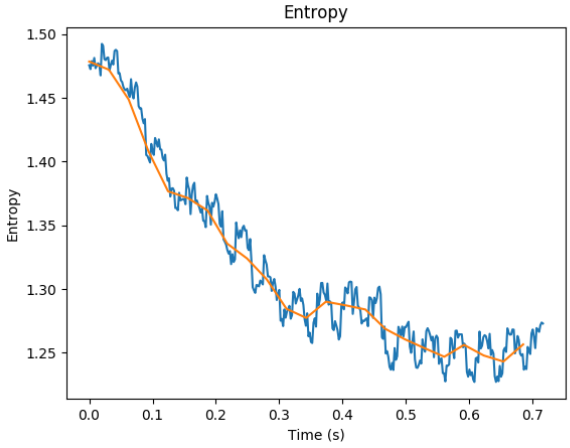

(a) Accelerometer 1

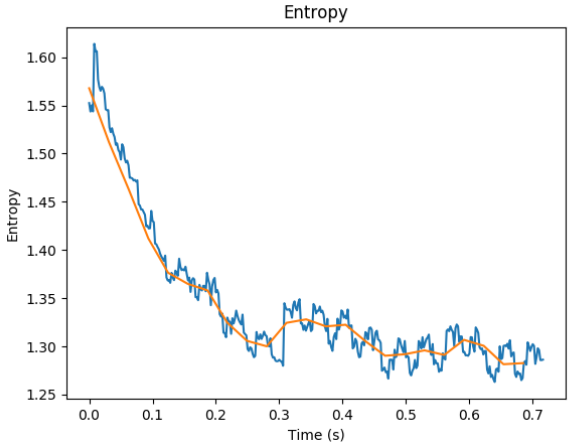

(b) Accelerometer 3

Figure 143: Wavelet Entropy Time series of vibration of the carbon fiber rod as sampled by the accelerometer No.1, 3 when exciting the rod at point 41 during the 1^{st} test.

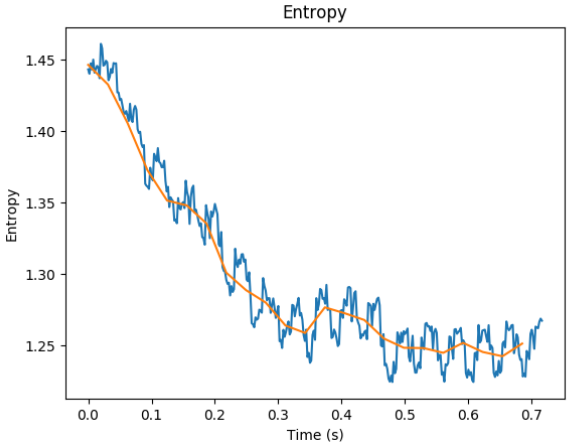

(a) Accelerometer 1

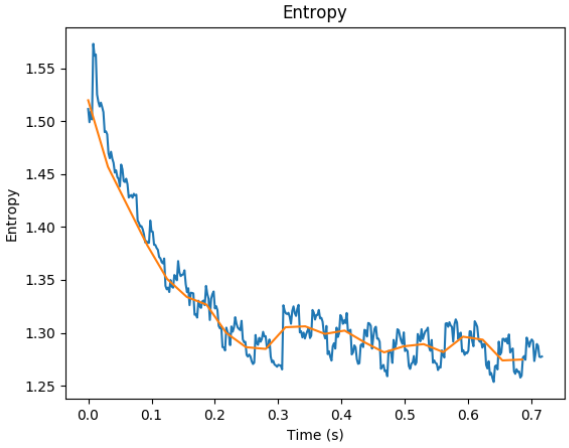

(b) Accelerometer 3

Figure 144: Wavelet Entropy Time series of vibration of the carbon fiber rod as sampled by the accelerometer No.1, 3 when exciting the rod at point 41 during the 2^{nd} test.

Wavelet Entropy Time Series of Point 42

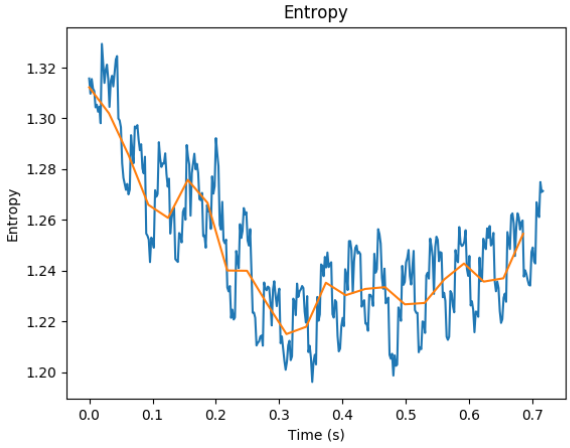

(a) Accelerometer 1

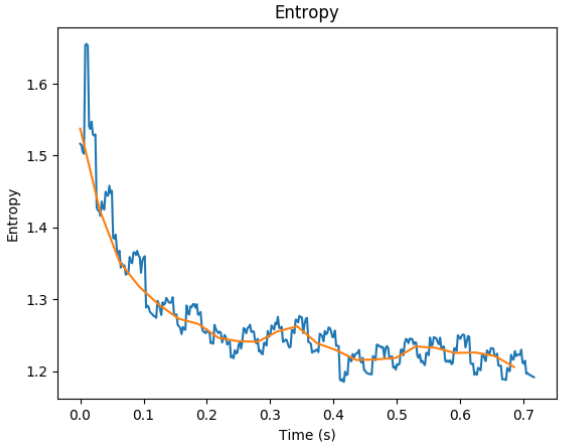

(b) Accelerometer 3

Figure 145: Wavelet Entropy Time series of vibration of the carbon fiber rod as sampled by the accelerometer No.1, 3 when exciting the rod at point 42 during the 1^{st} test.

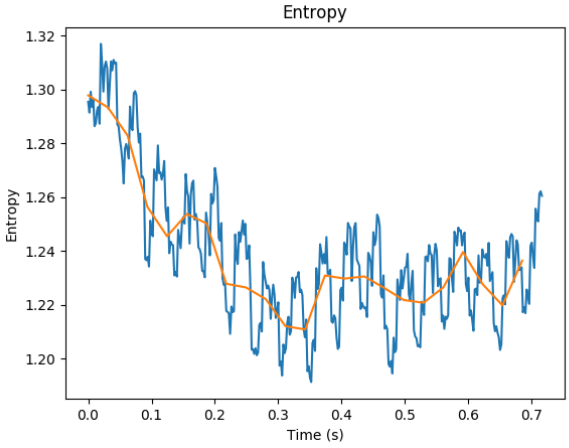

(a) Accelerometer 1

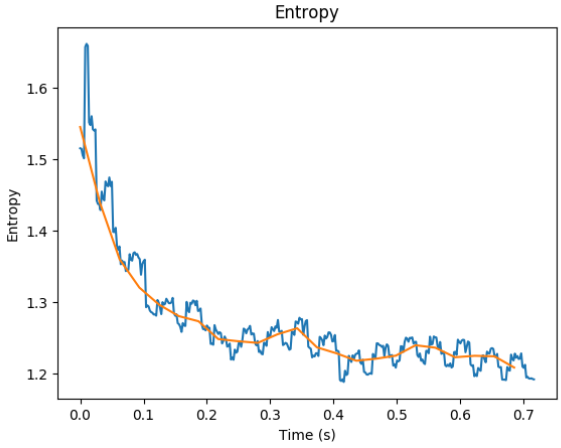

(b) Accelerometer 3

Figure 146: Wavelet Entropy Time series of vibration of the carbon fiber rod as sampled by the accelerometer No.1, 3 when exciting the rod at point 42 during the 2^{nd} test.

Wavelet Entropy Time Series of Point 43

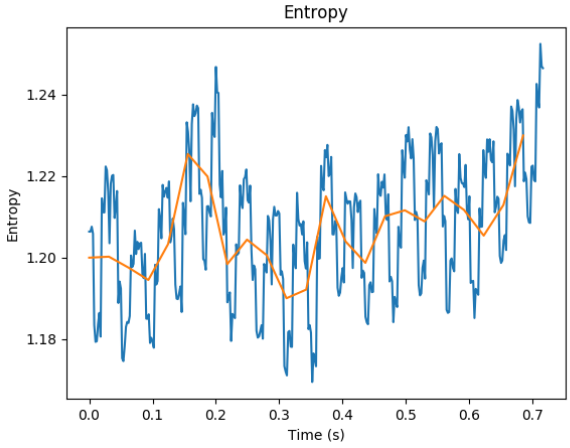

(a) Accelerometer 1

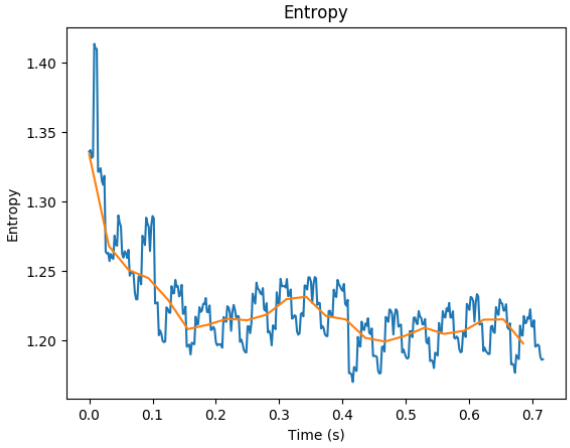

(b) Accelerometer 3

Figure 147: Wavelet Entropy Time series of vibration of the carbon fiber rod as sampled by the accelerometer No.1, 3 when exciting the rod at point 43 during the 1^{st} test.

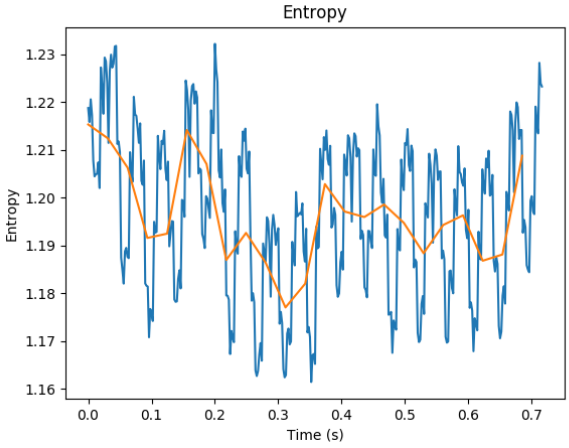

(a) Accelerometer 1

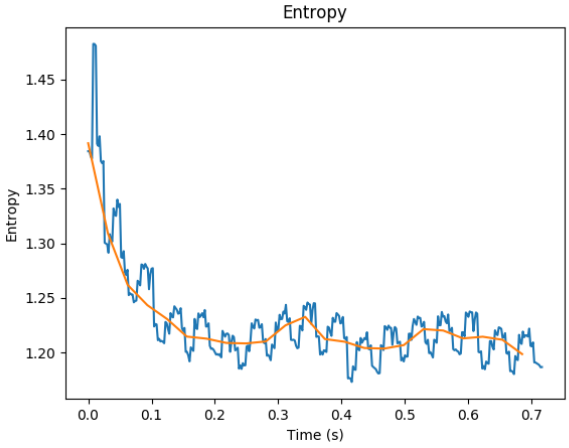

(b) Accelerometer 3

Figure 148: Wavelet Entropy Time series of vibration of the carbon fiber rod as sampled by the accelerometer No.1, 3 when exciting the rod at point 43 during the 2^{nd} test.

Wavelet Entropy Time Series of Point 44

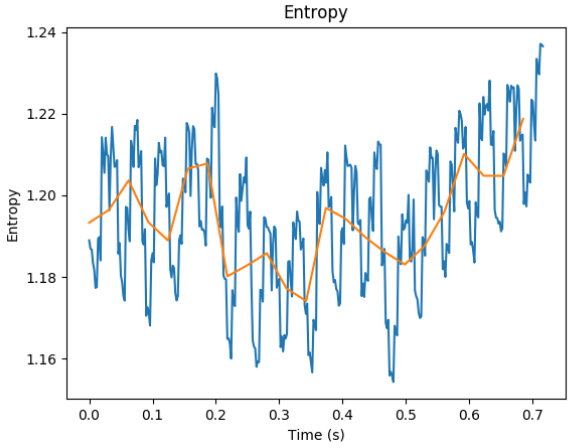

(a) Accelerometer 1

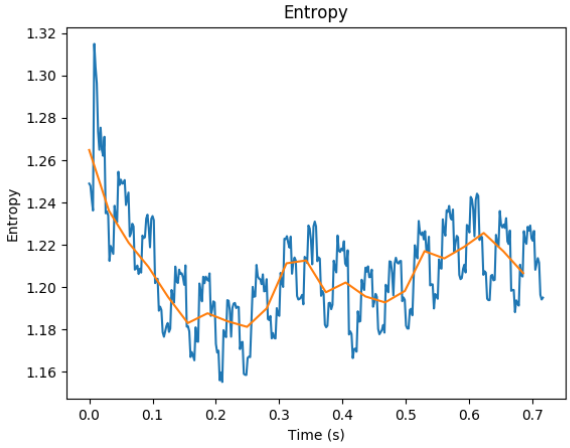

(b) Accelerometer 3

Figure 149: Wavelet Entropy Time series of vibration of the carbon fiber rod as sampled by the accelerometer No.1, 3 when exciting the rod at point 44 during the 1^{st} test.

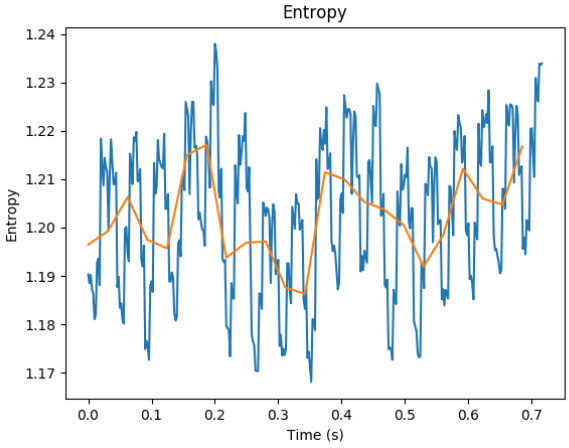

(a) Accelerometer 1

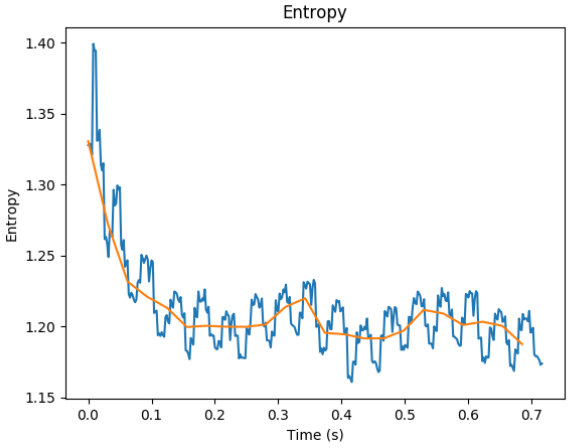

(b) Accelerometer 3

Figure 150: Wavelet Entropy Time series of vibration of the carbon fiber rod as sampled by the accelerometer No.1, 3 when exciting the rod at point 44 during the 2^{nd} test.

Wavelet Entropy Time Series of Point 45

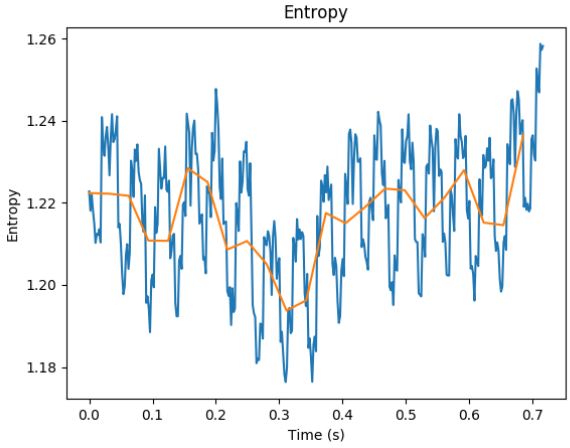

(a) Accelerometer 1

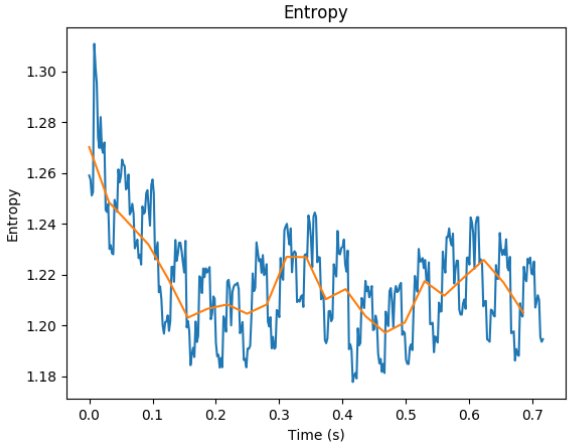

(b) Accelerometer 3

Figure 151: Wavelet Entropy Time series of vibration of the carbon fiber rod as sampled by the accelerometer No.1, 3 when exciting the rod at point 45 during the 1^{st} test.

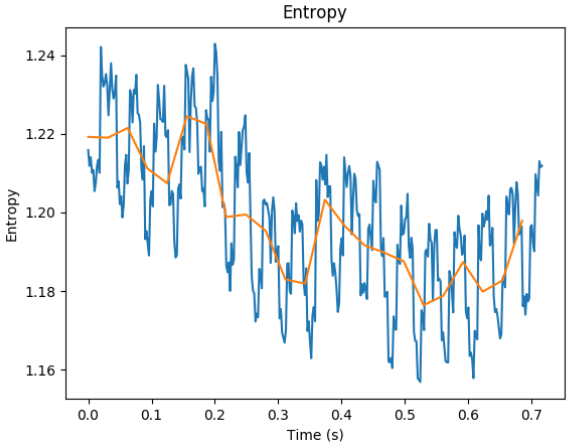

(a) Accelerometer 1

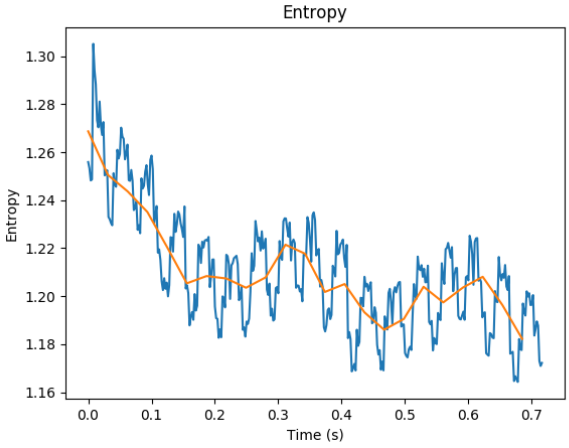

(b) Accelerometer 3

Figure 152: Wavelet Entropy Time series of vibration of the carbon fiber rod as sampled by the accelerometer No.1, 3 when exciting the rod at point 45 during the 2^{nd} test.

Wavelet Entropy Time Series of Point 46

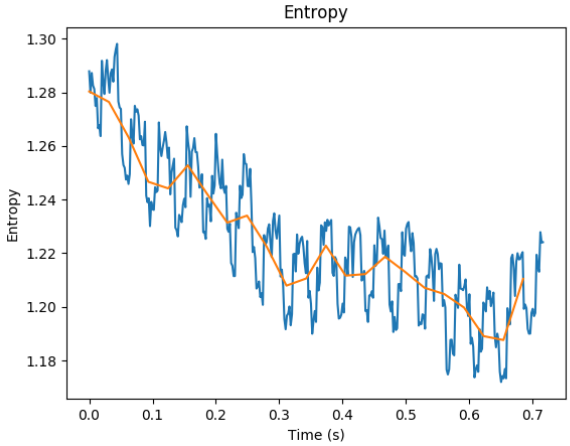

(a) Accelerometer 1

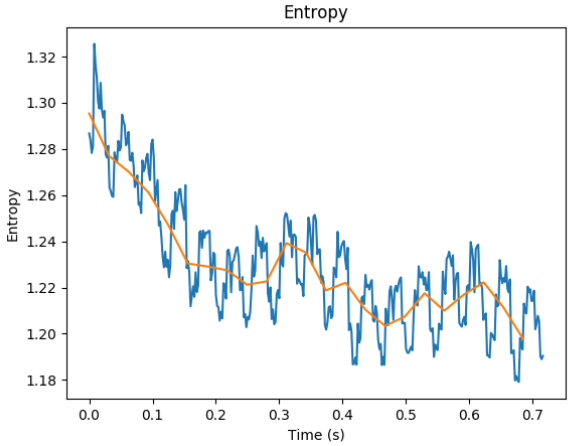

(b) Accelerometer 3

Figure 153: Wavelet Entropy Time series of vibration of the carbon fiber rod as sampled by the accelerometer No.1, 3 when exciting the rod at point 46 during the 1^{st} test.

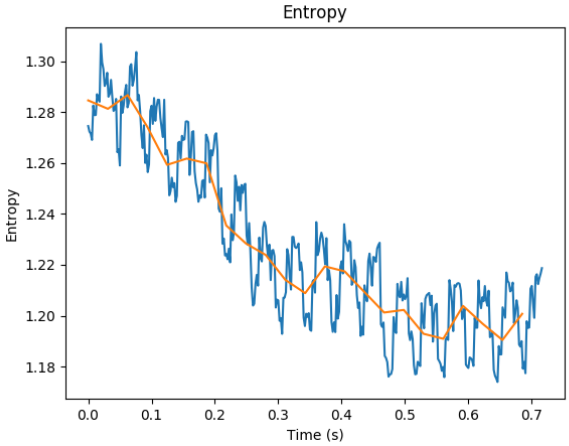

(a) Accelerometer 1

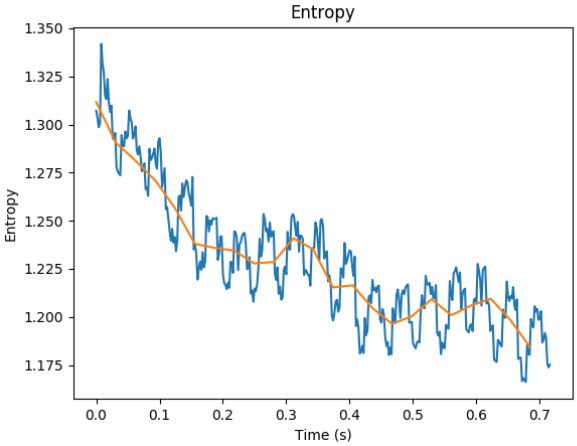

(b) Accelerometer 3

Figure 154: Wavelet Entropy Time series of vibration of the carbon fiber rod as sampled by the accelerometer No.1, 3 when exciting the rod at point 46 during the 2^{nd} test.

Wavelet Entropy Time Series of Point 47

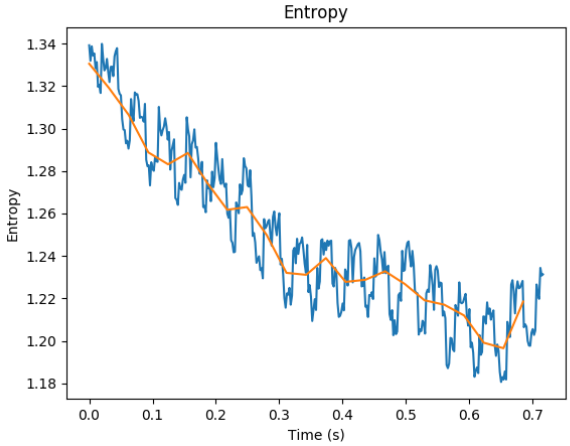

(a) Accelerometer 1

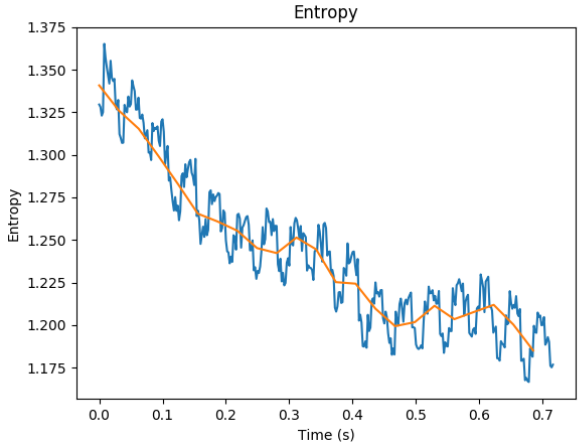

(b) Accelerometer 3

Figure 155: Wavelet Entropy Time series of vibration of the carbon fiber rod as sampled by the accelerometer No.1, 3 when exciting the rod at point 47 during the 1^{st} test.

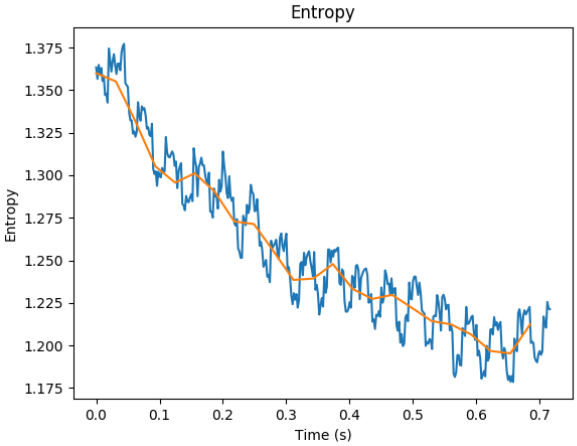

(a) Accelerometer 1

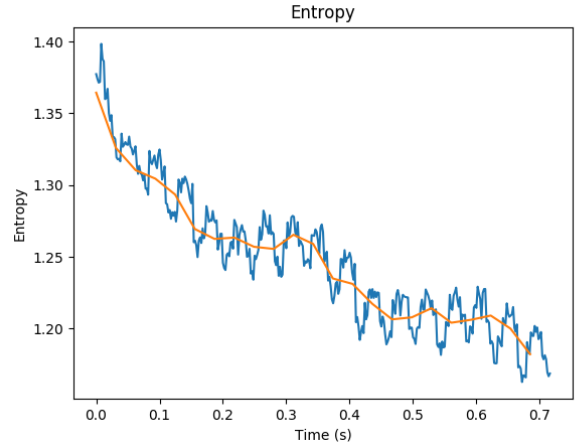

(b) Accelerometer 3

Figure 156: Wavelet Entropy Time series of vibration of the carbon fiber rod as sampled by the accelerometer No.1, 3 when exciting the rod at point 47 during the 2^{nd} test.

Wavelet Entropy Time Series of Point 48

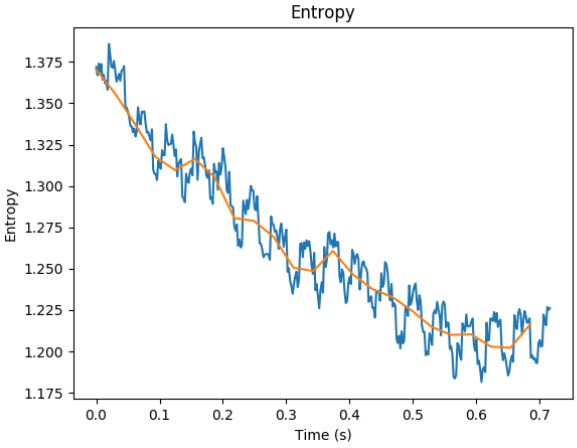

(a) Accelerometer 1

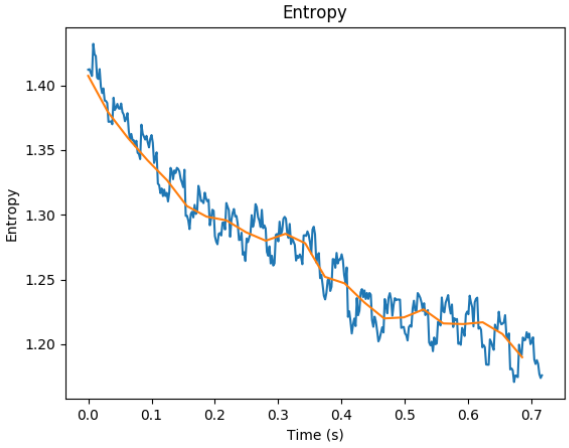

(b) Accelerometer 3

Figure 157: Wavelet Entropy Time series of vibration of the carbon fiber rod as sampled by the accelerometer No.1, 3 when exciting the rod at point 48 during the 1^{st} test.

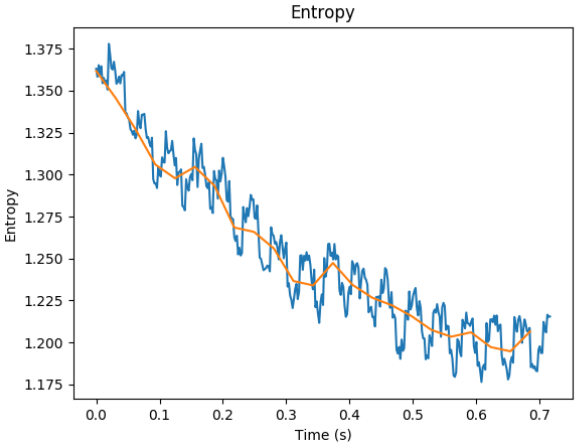

(a) Accelerometer 1

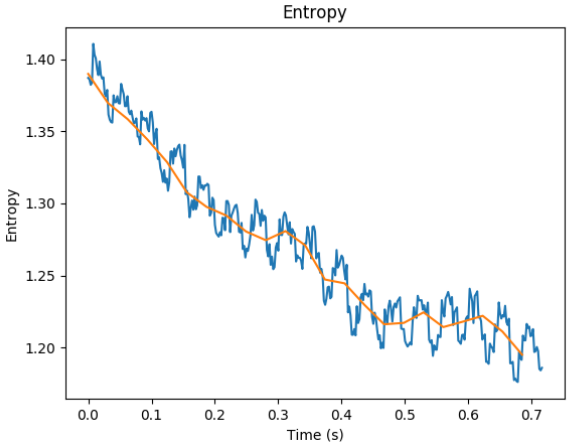

(b) Accelerometer 3

Figure 158: Wavelet Entropy Time series of vibration of the carbon fiber rod as sampled by the accelerometer No.1, 3 when exciting the rod at point 48 during the 2^{nd} test.

Wavelet Entropy Time Series of Point 49

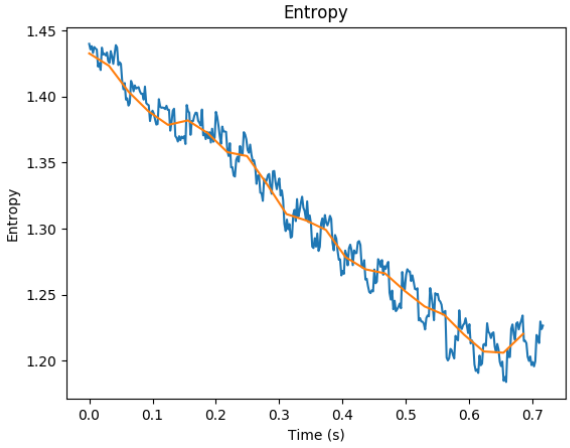

(a) Accelerometer 1

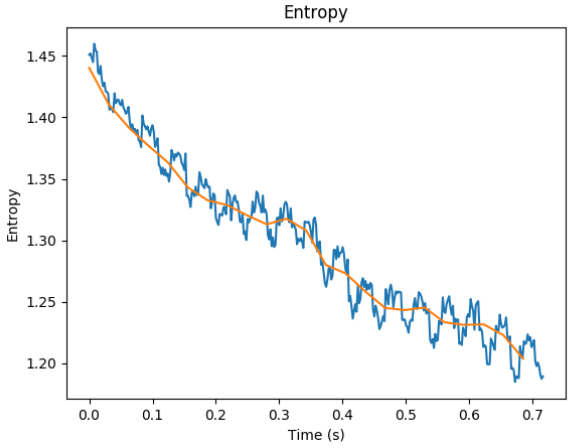

(b) Accelerometer 3

Figure 159: Wavelet Entropy Time series of vibration of the carbon fiber rod as sampled by the accelerometer No.1, 3 when exciting the rod at point 49 during the 1^{st} test.

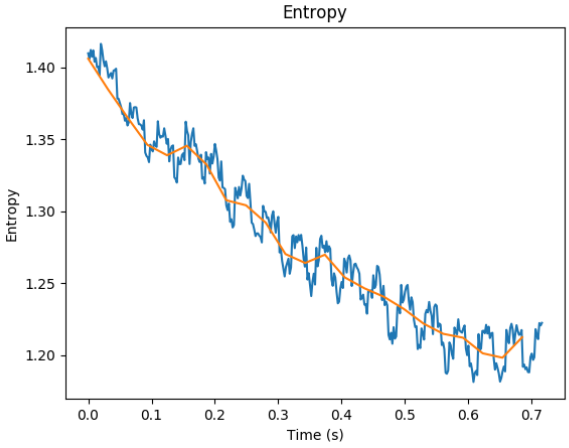

(a) Accelerometer 1

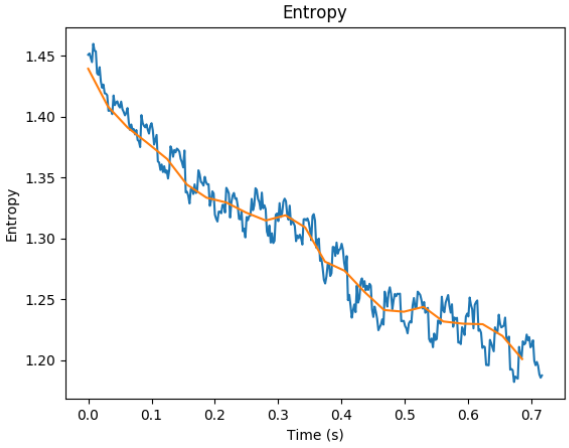

(b) Accelerometer 3

Figure 160: Wavelet Entropy Time series of vibration of the carbon fiber rod as sampled by the accelerometer No.1, 3 when exciting the rod at point 49 during the 2^{nd} test.

References

[Wan, 2018] (2018). Shannon entropy of binary wavelet packet subbands and its application in bearing fault extraction. *Entropy*, 20(4):260.

[Cook and Berthelot, 2001] Cook, D. and Berthelot, Y. (2001). Detection of small surface-breaking fatigue cracks in steel using scattering of rayleigh waves. *NDT & E International*, 34(7):483–492.

[Cropper, 1986] Cropper, W. H. (1986). Rudolf clausius and the road to entropy. *American journal of physics*, 54(12):1068–1074.

[Daubechies, 1992] Daubechies, I. (1992). *Ten lectures on wavelets*, volume 61. Siam.

[Dickson et al., 2017] Dickson, A. N., Barry, J. N., McDonnell, K. A., and Dowling, D. P. (2017). Fabrication of continuous carbon, glass and kevlar fibre reinforced polymer composites using additive manufacturing. *Additive Manufacturing*, 16:146–152.

[Ekici et al., 2008] Ekici, S., Yildirim, S., and Poyraz, M. (2008). Energy and entropy-based feature extraction for locating fault on transmission lines by using neural network and wavelet packet decomposition. *Expert Systems with Applications*, 34(4):2937–2944.

[Fresnel, 1819] Fresnel, A. (1819). Mémoire sur la diffraction de la lumière. *msld*, page 339.

[Friedel and Israel, 2010] Friedel, R. and Israel, P. B. (2010). *Edison's electric light: the art of invention*. JHU Press.

[Georgiou, 2019] Georgiou, I. T. (2019). Big data in experimental structural dynamics by synchronous ensembles of collocated acceleration signals (cas): The reciprocity principle failure and advanced diagnostics for composite material structures. *Structural Health Monitoring 2019*.

[Grimaldi and Bernia, 1966] Grimaldi, F. M. and Bernia, G. (1966). *Physico-mathesis de lumine coloribus et iride, 1665*. Dawsons of Pall Mall.

[Haldipur and Boone, 2014] Haldipur, P. and Boone, S. D. (2014). Development of phased array ultrasonic testing in lieu of radiography for testing complete joint penetration (cjp) welds. In *Nondestructive Characterization for Composite Materials, Aerospace Engineering, Civil Infrastructure, and Homeland Security 2014*, volume 9063, page 90632A. International Society for Optics and Photonics.

[Halmshaw, 1996] Halmshaw, R. (1996). *Introduction to the non-destructive testing of welded joints*. Woodhead Publishing.

[Harris et al., 2020] Harris, C. R., Millman, K. J., van der Walt, S. J., Gommers, R., Virtanen, P., Cournapeau, D., Wieser, E., Taylor, J., Berg, S., Smith, N. J., Kern, R., Picus, M., Hoyer, S., van Kerkwijk, M. H., Brett, M., Haldane, A., del R'ıo, J. F., Wiebe, M., Peterson, P., G'erard-Marchant, P., Sheppard, K., Reddy, T., Weckesser, W., Abbasi, H., Gohlke, C., and Oliphant, T. E. (2020). Array programming with NumPy. *Nature*, 585(7825):357–362.

[Haüy, 1784] Haüy, R. J. (1784). *Essai d'une théorie sur la structure des crystaux: appliquée à plusieurs genres de substances crystallisées*. Chez Gogué & Née de la Rochelle.

[Houtz, 1950] Houtz, R. (1950). " orlon" acrylic fiber: Chemistry and properties. *Textile Research Journal*, 20(11):786–801.

[Hunter, 2007a] Hunter, J. D. (2007a). Matplotlib: A 2d graphics environment. *Computing in Science & Engineering*, 9(3):90–95.

[Hunter, 2007b] Hunter, J. D. (2007b). Matplotlib: A 2d graphics environment. *Computing in science & engineering*, 9(3):90–95.

[Kullback and Leibler, 1951] Kullback, S. and Leibler, R. A. (1951). On information and sufficiency. *The annals of mathematical statistics*, 22(1):79–86.

[Kumar et al., 2010] Kumar, S., Srinivasan, P., Sharma, S. D., Subbaiah, K. V., and Mayya, Y. S. (2010). Evaluation of scatter contribution and distance error by iterative methods for strength determination of hdr 192ir brachytherapy source. *Medical Dosimetry*, 35(3):230–237.

[Kumar et al., 2012] Kumar, Y., Dewal, M. L., and Anand, R. S. (2012). Relative wavelet energy and wavelet entropy based epileptic brain signals classification. *Biomedical Engineering Letters*, 2(3):147–157.

[Lee et al., 2019a] Lee, G., Gommers, R., Waselewski, F., Wohlfahrt, K., and OLeary, A. (2019a). Pywavelets: A python package for wavelet analysis. *Journal of Open Source Software*, 4(36):1237.

[Lee et al., 2019b] Lee, G. R., Gommers, R., Waselewski, F., Wohlfahrt, K., and Oamp;8217;Leary, A. (2019b). Pywavelets: A python package for wavelet analysis. *Journal of Open Source Software*, 4(36):1237.

[Lin et al., 2010] Lin, J.-L., Liu, J. Y.-C., Li, C.-W., Tsai, L.-F., and Chung, H.-Y. (2010). Motor shaft misalignment detection using multiscale entropy with wavelet denoising. *Expert systems with applications*, 37(10):7200–7204.

[Lobkis and Rokhlin, 2010] Lobkis, O. and Rokhlin, S. (2010). Characterization of polycrystals with elongated duplex microstructure by inversion of ultrasonic backscattering data. *Applied Physics Letters*, 96(16):161905.

[Mallat, 1999] Mallat, S. (1999). *A wavelet tour of signal processing*. Elsevier.

[Mauceri et al., 1999] Mauceri, T., Biggs, P., Beatty, J., and Flynn, D. (1999). Scatter and attenuation measurements at distances greater than 10 cm from an source. *Medical Physics*, 26(1):97–99.

[Mow and Pao, 1971] Mow, C.-C. and Pao, Y.-H. (1971). The diffraction of elastic waves and dynamic stress concentrations. Technical report, RAND CORP SANTA MONICA CALIF.

[Newland, 2012] Newland, D. E. (2012). *An introduction to random vibrations, spectral & wavelet analysis*. Courier Corporation.

[Ni and Iwamoto, 2002] Ni, Q.-Q. and Iwamoto, M. (2002). Wavelet transform of acoustic emission signals in failure of model composites. *Engineering Fracture Mechanics*, 69(6):717–728.

[Oliphant, 2006] Oliphant, T. (2006). *Guide to NumPy*.

[pandas development team, 2020] pandas development team, T. (2020). pandas-dev/pandas: Pandas.

[Park, 1999] Park, W. B. (1999). The production of hollow carbon fibre from a special pan precursor.

[Planck, 1914] Planck, M. (1914). The theory of heat radiation, translated by m. *Masius, P. Blackistons Son & Co, Philadelphia, reprinted by Kessinger*.

[Prasad and Simha, 2002] Prasad, P. and Simha, K. (2002). Energy released during arc crack propagation. *International journal of fracture*, 116(1):3–8.

[PROBABILITY, 1984] PROBABILITY, A. P. (1984). Random variables, and stochastic processes.

[Rayleigh, 1872] Rayleigh, J. W. S. (1872). *Investigation of the disturbance produced by a spherical obstacle on the waves of sound*. CF Hodgson & Sons.

[Rayleigh, 1888] Rayleigh, L. (1888). Wave theory of light (in encyclopedia britannica). *New York*.

[Ren and Sun, 2008] Ren, W.-X. and Sun, Z.-S. (2008). Structural damage identification by using wavelet entropy. *Engineering Structures*, 30(10):2840–2849.

[Rosso et al., 2001] Rosso, O. A., Blanco, S., Yordanova, J., Kolev, V., Figliola, A., Schürmann, M., and Başar, E. (2001). Wavelet entropy: a new tool for analysis of short duration brain electrical signals. *Journal of neuroscience methods*, 105(1):65–75.

[Shannon, 1948] Shannon, C. E. (1948). A mathematical theory of communication. *Bell system technical journal*, 27(3):379–423.

[Sharp and Matschinsky, 2015] Sharp, K. and Matschinsky, F. (2015). Translation of ludwig boltzmanns paper on the relationship between the second fundamental theorem of the mechanical theory of heat and probability calculations regarding the conditions for thermal equilibrium sitzungberichte der kaiserlichen akademie der wissenschaften. mathematisch-naturwissen classe. abt. ii, lxxvi 1877, pp 373-435 (wien. ber. 1877, 76: 373-435). reprinted in

wiss. abhandlungen, vol. ii, reprint 42, p. 164-223, barth, leipzig, 1909. *Entropy*, 17(4):1971–2009.

[Shim and Volkmer, 1996] Shim, H.-T. and Volkmer, H. (1996). On the gibbs phenomenon for wavelet expansions. *Journal of approximation theory*, 84(1):74–95.

[Soares et al., 2002] Soares, S. D., Donato, G. V. P., do Fundão-Quadra, I., and de Janeiro-RJ-Brazil, R. (2002). Acoustic emission- developments in petrobras r & d center in the last twenty years. *Journal of Nondestructive Testing(Germany)*, 7(9):1–8.

[Sorokin, 2002] Sorokin, S. (2002). Analysis of vibrations and energy flows in sandwich plates bearing concentrated masses and spring-like inclusions in heavy fluid-loading conditions. *Journal of Sound and Vibration*, 253(2):485–505.

[Strang, 1989] Strang, G. (1989). Wavelets and dilation equations: A brief introduction. *SIAM review*, 31(4):614–627.

[Strang, 1994] Strang, G. (1994). Wavelets. *American Scientist*, 82(3):250–255.

[Strang and Nguyen, 1996] Strang, G. and Nguyen, T. (1996). *Wavelets and filter banks*. SIAM.

[Swann,] Swann. Swann jw, brit. pat. 4933, 1880.

[Tant et al., 2015] Tant, K. M., Mulholland, A. J., Langer, M., and Gachagan, A. (2015). A fractional fourier transform analysis of the scattering of ultrasonic waves. *Proceedings of the Royal Society A: Mathematical, Physical and Engineering Sciences*, 471(2175):20140958.

[Tourin et al., 2000] Tourin, A., Fink, M., and Derode, A. (2000). Multiple scattering of sound. *Waves in random media*, 10(4):R31–R60.

[Van Rossum, 2020] Van Rossum, G. (2020). *The Python Library Reference, release 3.8.2*. Python Software Foundation.

[Van Rossum and Drake, 2009] Van Rossum, G. and Drake, F. L. (2009). *Python 3 Reference Manual*. CreateSpace, Scotts Valley, CA.

[Virtanen et al., 2020] Virtanen, P., Gommers, R., Oliphant, T. E., Haberland, M., Reddy, T., Cournapeau, D., Burovski, E., Peterson, P., Weckesser, W., Bright, J., van der Walt,

S. J., Brett, M., Wilson, J., Millman, K. J., Mayorov, N., Nelson, A. R. J., Jones, E., Kern, R., Larson, E., Carey, C. J., Polat, İ., Feng, Y., Moore, E. W., VanderPlas, J., Laxalde, D., Perktold, J., Cimrman, R., Henriksen, I., Quintero, E. A., Harris, C. R., Archibald, A. M., Ribeiro, A. H., Pedregosa, F., van Mulbregt, P., and SciPy 1.0 Contributors (2020). SciPy 1.0: Fundamental Algorithms for Scientific Computing in Python. *Nature Methods*, 17:261–272.

[von Laue, 1912] von Laue, M. (1912). *Eine quantitative prüfung der theorie für die interferenzerscheinungen bei röntgenstrahlen*. Verlag der Kgl. Bayer. Akad. der Wiss.

[Wang et al., 2014] Wang, Y., Li, W., Zhou, J., Li, X., and Pu, Y. (2014). Identification of the normal and abnormal heart sounds using wavelet-time entropy features based on oms-wpd. *Future Generation Computer Systems*, 37:488–495.

[Wes McKinney, 2010] Wes McKinney (2010). Data Structures for Statistical Computing in Python. In Stéfan van der Walt and Jarrod Millman, editors, *Proceedings of the 9th Python in Science Conference*, pages 56 – 61.

[Wu and Siegel, 1999] Wu, H. and Siegel, M. (1999). Correlation of accelerometer and microphone data in the" coin tap test". In *IMTC/99. Proceedings of the 16th IEEE Instrumentation and Measurement Technology Conference (Cat. No. 99CH36309)*, volume 2, pages 814–819. IEEE.

[Zheng-You et al., 2006] Zheng-You, H., Xiaoqing, C., and Guoming, L. (2006). Wavelet entropy measure definition and its application for transmission line fault detection and identification;(part i: Definition and methodology). In *2006 International Conference on Power System Technology*, pages 1–6. IEEE.